A Measurement of the Polarization of J/ψ Mesons Produced in High-Energy $p\bar{p}$ Collisions

by

Robert J. Cropp

A thesis submitted in conformity with the requirements
for the degree of Doctor of Philosophy
Graduate Department of Physics
University of Toronto

Copyright © 2000 by Robert J. Cropp

Abstract

A Measurement of the Polarization of J/ψ Mesons Produced in High-Energy $p\bar{p}$ Collisions

Robert J. Cropp

Doctor of Philosophy

Graduate Department of Physics

University of Toronto

2000

This dissertation presents an analysis of the polarization of J/ψ mesons produced in $p\bar{p}$ collisions at a centre-of-mass energy of 1.8 TeV. The collisions were produced by the Fermilab Tevatron collider, the world's highest energy particle accelerator. The data were recorded by the Collider Detector at Fermilab during Run 1 of the Tevatron in 1992-1995.

The J/ψ meson consists of a charm quark and its antiquark, and is the best-known type of quarkonium, the bound state of a heavy quark-antiquark pair. The measurement of the production polarization of J/ψ mesons and other quarkonia provides a test of quarkonium production models. The study of quarkonium production is important for understanding the strong nuclear force between quarks. The strong force is one of the four known fundamental forces, being responsible for binding quarks into hadrons and holding atomic nuclei together.

The polarization of centrally produced J/ψ mesons has been measured over the transverse momentum range $4 - 20$ GeV/c , using an analysis of the angular distribution of their decays to $\mu^+\mu^-$. Decay length measurements made by CDF's silicon vertex detector allowed the promptly produced J/ψ mesons to be separated from those produced in B-hadron decays. The prompt and B-decay polarization parameters, α_P and α_B, have both been measured. The measured value of α_P is positive at intermediate P_T, but is consistent with zero above 12 GeV/c , in apparent disagreement with predictions of the NRQCD factorization formalism.

Acknowledgements

Many people have helped and supported me during my time as a graduate student, and I am glad to have a place to acknowledge them here. First and foremost is my supervisor, Professor William Trischuk, who has taught me much of what I know about high-energy physics. William's guidance and support have made this analysis and my Ph.D. possible.

I would also like to acknowledge all the rest of the Toronto CDF group, for it has been a pleasure to work here. Particular thanks go to Andreas and Wendy (that's Dr. Warburton and Dr. Taylor, now) for their help and guidance when I was starting out here. Professor Pekka Sinervo has always given me valuable advice, and has shown me that there is such a thing as a free lunch. Andrew Robinson has been a great office-mate and the source of many good conversations on topics inside and outside of physics.

I thank all of my colleagues in the CDF B-physics group with whom I have worked over the past three years. I also thank everyone in the silicon testing group at Fermilab, where I enjoyed doing my service work. Beyond these specific groups, all of the people who make up the CDF collaboration deserve to be acknowledged for their hard work in creating and running the experiment that made this analysis possible.

I acknowledge with gratitude the financial support I have received from the Natural Sciences and Engineering Research Council of Canada, the University of Toronto Physics Department, the Walter C. Sumner Foundation and the Alberta Heritage Scholarship Fund.

My final thanks go to my parents for their love and support.

Contents

1 Introduction **1**

1.1 A History of the Quark 2

1.2 Quantum Chromodynamics and Hadron Production 6

1.3 Charmonium Production 11

1.4 Predictions for ψ Polarization 18

1.5 Dissertation Overview 21

2 Accelerator and Detector **23**

2.1 The Fermilab Tevatron 24

2.2 The CDF Detector 27

2.2.1 Solenoid magnet 28

2.2.2 Central tracking chamber 30

2.2.3 Silicon vertex detector 32

2.2.4 Vertex time projection chamber 36

2.2.5 Calorimeters 38

2.2.6 Muon detectors 41

2.2.7 Beam-beam counters 46

2.2.8 Data acquisition and trigger system 46

3 Data Sample and Event Selection **49**

3.1 Run 1 of the Tevatron 49

3.2 Dimuon Triggers 50

3.2.1 Level 1 . . . 50
3.2.2 Level 2 . . . 52
3.2.3 Level 3 . . . 55
3.3 Data Storage . . . 55
3.4 Event Requirements . . . 56

4 J/ψ Polarization Analysis **63**
4.1 The ct Fit . . . 67
4.1.1 Background fit . . . 67
4.1.2 Signal fit . . . 68
4.1.3 ct fit results . . . 69
4.2 Acceptance Modeling . . . 74
4.3 Polarization Fit . . . 78
4.3.1 Inclusive polarization fit . . . 78
4.3.2 Data analysis polarization fit . . . 82
4.3.3 Monte Carlo experiments . . . 85
4.4 Systematic Uncertainties . . . 90
4.4.1 Prompt and B-fractions . . . 90
4.4.2 Monte Carlo P_T spectrum . . . 90
4.4.3 Trigger efficiency . . . 93
4.5 Polarization Fit Results . . . 95

5 Conclusion **99**
5.1 Discussion . . . 99
5.1.1 Prompt polarization . . . 99
5.1.2 B-decay polarization . . . 101
5.2 Future Prospects . . . 103

A The J/ψ Angular Decay Distribution **105**
A.1 Derivation . . . 105

A.2 Effect of the $\cos 2\phi^*$ term 108
A.2.1 Measuring ρ_{1-1} 109
A.2.2 Shift in α 110
A.2.3 Results 110

B SVXII/ISL Service Work **113**
B.1 The CDFII Upgrade 113
B.2 SVXII/ISL Production and Testing 115
B.3 The Burn-In System 117

C The CDF Run I Collaboration **121**

Bibliography **126**

List of Tables

1.1 The charmonium states and the known bottomonium states: only states below the open-flavour threshold are listed. 9

1.2 Values of some NRQCD matrix elements, fitted from CDF cross section data and the ψ leptonic widths, from [45]. 15

2.1 Selected characteristics of the various calorimeters. 40

3.1 Muon P_T requirements depend on the CFT bin used in the Level 2 trigger. 57

3.2 Dimuon mass signal and sideband windows for each $P_T^{J/\psi}$ bin. 61

4.1 The ct background fit results, from the mass sidebands. 72

4.2 The ct signal window fit results. 73

4.3 Fractions of prompt and B in short- and long-lived ct regions. 73

4.4 Fitted parameters for the $P_T^{J/\psi}$ spectra used in acceptance Monte Carlo. . . 75

4.5 Results of the inclusive polarization fit applied to data. 82

4.6 The eight Monte Carlo samples used in the data analysis polarization fit. . 83

4.7 The effect of B-fraction variation on fitted values of α. 91

4.8 ct requirements used to define high-purity prompt and B-decay samples in SVX data, for the P_T comparison. 91

4.9 Results of comparison between Monte Carlo and data P_T spectra within each P_T bin. 92

4.10 Shifts in α with shallower/steeper trigger simulation efficiency curves. . . . 95

4.11 Results of the data analysis polarization fit. 96

A.1 Estimated values of q and R, fitted values of F and derived $\Delta\alpha$ for prompt production. 111

List of Figures

1.1 The three generations of quarks and leptons as weak isodoublets. 6

1.2 The bound charmonium states. 10

1.3 Examples of ψ production in the Colour Singlet Model. 13

1.4 Differential ψ production cross sections in $p\bar{p}$ collisions, multiplied by the branching ratio to $\mu^+\mu^-$. 17

1.5 Schematic diagram of gluon fragmentation to a $c\bar{c}$ $[\underline{8},^3S_1]$ pair, followed by binding (the blob) into a ψ meson. 18

1.6 An NRQCD factorization prediction for the polarization parameter α of directly produced ψ mesons, as a function of ψ transverse momentum. 20

2.1 An overview of the Fermilab accelerator complex. 25

2.2 An isometric view of the CDF detector in Run 1, showing its axial and forward/backward symmetry. 27

2.3 One quadrant of the CDF detector in Run 1. 29

2.4 A CTC endplate, showing the wire feedthrough slots for the cells in the nine superlayers. 31

2.5 A typical $J/\psi \to \mu^+\mu^-$ candidate event reconstructed in the CTC, seen in the plane transverse to the beamline. 33

2.6 An SVX barrel. Two such barrels constitute the SVX detector; the readout ends are located furthest from the interaction point. 37

2.7 An SVX layer 2 ladder with 4 SVX IC chips. 38

2.8 Side view of two opposite octants of the VTX, showing the two primary vertices in the event of Figure 2.5. 39

2.9 One wedge of the central calorimeter, showing the ten towers in η. 42
2.10 Central muon coverage in pseudorapidity and azimuth. 44
2.11 Location of the central muon chambers. 45
2.12 A central muon module, consisting of four layers of four cells. 45
2.13 A CMU cell, showing the aluminum sheets and I-beams, G-10 spacers and the steel sense wire. 46
3.1 Transverse momentum measurement in the Level 1 muon trigger. 51
3.2 Level 1 and 2 muon trigger efficiencies in the CMU as functions of P_T. . . . 52
3.3 A high P_T track passing through an axial superlayer of the CTC. 53
3.4 Transverse decay length measurement in an inclusive $B \to J/\psi$ decay. . . . 59
3.5 The J/ψ peak in the dimuon mass distribution, in eight $P_T^{J/\psi}$ bins. 62
4.1 The J/ψ decay shown in its rest frame. 64
4.2 Reconstructed $\chi_c \to J/\psi\ \gamma$ decays in the J/ψ data sample. 66
4.3 Fitted prompt and B-decay ct distributions for the full P_T range, shown over a limited ct range. 70
4.4 The ct fit for the full P_T range. 71
4.5 Parameterization of J/ψ transverse momentum spectra. 75
4.6 Distributions of $\cos\theta^*$ in simulated unpolarized Run 1B sample. 77
4.7 Comparison of $P_T^{J/\psi}$ distributions in data and Monte Carlo samples. . . . 79
4.8 Comparison of $y^{J/\psi}$ distributions in data and Monte Carlo samples. . . . 80
4.9 The polarization fit in the $8 - 10$ GeV/c bin. 86
4.10 The polarization fit in the $12 - 15$ GeV/c bin. 87
4.11 Pull distributions in each P_T bin, from inclusive fits in Monte Carlo experiments with $\alpha = 0$. 88
4.12 Prompt pull distributions from data analysis fits in Monte Carlo experiments with $\alpha_P = 0.5$ and $\alpha_B = 0$. 89
4.13 The trigger efficiency systematic uncertainty as a function of P_T. 94
4.14 Polarization fit results. 97
A.1 Relative acceptance versus ϕ^*, over the P_T range $4 - 20$ GeV/c 108

B.1 An end-view of an SVXII barrel, showing the five layers of silicon ladders mounted on the bulkhead. 114
B.2 A isometric view of the layout of SVXII and ISL. 115
B.3 Schematic of a small-angle stereo sensor. 118

Chapter 1

Introduction

As far as we know, all matter in the universe is made out of a few types of fundamental particles, each with several properties but no measurable size. The science of particle physics is the study of these elementary constituents of matter and the interactions between them.

The idea that matter consists of discrete microscopic parts, rather than being continuous, has been around for a long time. However, definitive empirical evidence has only accumulated within the past two hundred years. Dalton proposed the atomic hypothesis soon after the beginning of the nineteenth century [1]. Since then the understanding of atoms and their behaviour has grown and become essential to most areas of physics and chemistry. Its importance has been succinctly described by the particle theorist Richard Feynman:

> If, in some cataclysm, all of scientific knowledge were to be destroyed, and only one sentence passed on to the next generation of creatures, what statement would contain the most information in the fewest words? I believe it is the *atomic hypothesis* ... that *all things are made of atoms — little particles that move around in perpetual motion, attracting each other when they are a little distance apart, but repelling upon being squeezed into one another.* [2]

Modern science has often used the successful strategy of breaking a complex system into its component parts in order to understand it. Particle physics can be considered the extreme case of this method. The atom was originally conceived of as the ultimate

particle, indivisible and unchanging, but over time experimentation revealed its internal structure. By the time quantum mechanics was developed, atoms were known to consist of a small, heavy, positively charged nucleus surrounded by a structured cloud of negatively charged electrons. This concept is fundamental to much of chemistry and condensed-matter physics. Subsequently, it was established that the atomic nucleus itself is an aggregation containing two types of particle, the proton and the neutron. And the proton and neutron are themselves composite particles, being composed of constituents known as quarks.

At present, quarks and leptons seem to be the ultimate particles of matter (the electron is one of the leptons). They appear pointlike down to the limits of experimental resolution, on the order of 10^{-18} metres. The length scales at which quarks and leptons can be studied are intimately linked to the energies at which they interact. As a particle's energy increases, its quantum wavelength decreases, and it can "resolve" other particles at shorter distances. This is in exact analogy to the superior resolution obtained with the shorter wavelengths of an electron microscope when compared to an optical microscope. Since its birth, experimental particle physics has been engaged in an ongoing effort to achieve higher and higher energies in the laboratory, so that smaller distances may be probed. For this reason, experimental particle physics has also come to be known as high energy physics.

This dissertation presents an analysis of the production of a particular bound state of a charm quark and its antiquark, called the J/ψ, in a high energy physics experiment. Processes such as this yield insight into the nature of interactions between quarks. The remainder of this chapter provides the background and motivation for the analysis. Subsequent chapters describe the experimental apparatus used, the data collected, the analysis procedure and the interpretation of the results.

1.1 A History of the Quark

There is not room here for a comprehensive review of the history of particle physics, or even for many details. This section therefore gives a brief overview, with an emphasis on bound states and fundamental particles. A suitable year to date the start of particle physics is

1895, with Röntgen's discovery of x-rays [3]. The next two years saw Becquerel's discovery of natural radioactivity in uranium [4], and Thompson's measurement of the charge-to-mass ratio of the electron [5]. The first two discoveries provided evidence that atoms possess internal structure. The third definitively established the electron as a particle.

The nature of the atom was clarified by Rutherford's series of experiments on the scattering of α and β particles on a wide variety of elements [6]. These experiments demonstrated that most of an atom's mass is concentrated within a dense, charged nucleus which occupies a very small fraction of the atom's volume. Rutherford later found that the nucleus contained positively charged particles [7], which became known as protons. The discovery of the neutron in 1932 [8] completed the picture of the atomic structure: a small nucleus consisting of a number of protons and neutrons, surrounded by a cloud of electrons.

Naturally, the experimental study of the consituents of the atom was intimately connected to the development of quantum mechanics and subsequently quantum field theory. The Compton effect, the scattering of x-rays from atomic electrons, demonstrated that light can behave like a particle [9]. Meanwhile the diffraction of electrons demonstrated that matter particles can behave like waves [10]. The need soon arose for a satisfactory theoretical description of systems in which both special relativity and quantum mechanics are relevant. Quantum field theory combined the two, and predicted the existence of antiparticles, of which the first to be discovered was the positron, in 1932 [11]. Quantum field theory describes the forces between fundamental particles of matter (which are fermions, having half-integer spin) as being mediated by specific bosons (which have integer spin). A highly successful quantum field theory of the electromagnetic (EM) interaction called Quantum Electrodynamics (QED) evolved during the 1920's to the 1940's. QED describes the electromagnetic force between charged fermions as the exchange of photons, which are quanta of EM radiation. By that time two other forces between subatomic particles had been recognized. The strong force acts between nucleons (protons and neutrons) and is responsible for nuclear binding. The weak force is responsible for certain types of particle decays, such as nuclear β-decay.

During the 1940's, 50's and 60's a wide variety of unstable particles was discovered,

at first in cosmic ray experiments and later on in accelerator experiments. For each new particle, physicists attempted to identify as many of its properties as possible, including its mass, spin, charge, lifetime and modes of production and decay. An important distinction arose between particles which feel the strong force (hadrons), and those which do not (leptons). The electron is a lepton, as is its heavier counterpart the muon, and the neutrinos. The hadrons can be subdivided into two categories based on their spin. The baryons are fermions, whereas the mesons are bosons. The nucleons are the most familiar examples of baryons. The first meson to be observed was the pion [12], which was identified as the force carrier between nucleons in Yukawa's theory of the strong nuclear interaction [13].

Another characteristic of hadrons which distinguished them from leptons was isospin. Isospin is a symmetry between certain types of hadrons based on the mathematical group $SU(2)$, and was first suggested by Heisenberg [14]. Hadrons can be grouped into "isospin multiplets" of one, two, three or more particles. Each member of the multiplet has an almost identical mass, and exhibits similar behaviour in strong interactions. Some examples of isospin multiplets are the nucleon doublet (p, n) and the pion triplet (π^+, π^0, π^-).

The proliferation of new hadrons made a more detailed classification scheme highly desirable. In 1961 Gell-Mann and Ne'eman independently showed that hadrons could be naturally classified into "supermultiplets" — groups of baryons or mesons with the same spin and parity and similar masses [15, 16]. Each supermultiplet contained several isospin multiplets. The arrangement of hadrons within each supermultiplet displayed patterns of charge, isospin and strangeness, based on the symmetry group $SU(3)$. This formed the beginning of the quark model, in which hadrons are pictured as bound states of fundamental spin $\frac{1}{2}$ particles known as quarks [17, 18]. Mesons are quark-antiquark bound states, and baryons are states of three quarks. At the time, all of the known hadrons could be classified using three quarks, named "up", "down" and "strange". The up and down quarks had nearly identical masses and formed an isospin doublet, which accounted for the occurence of isospin multiplets among hadrons. The quantum numbers of a hadron could be understood from the quantum numbers of the quarks and their angular momentum wavefunction. The quarks were also required to possess new quantum property called colour. However, quarks

only seemed to combine to form colourless states, and no free quarks were ever observed.

A series of deep-inelastic electron-proton scattering experiments at SLAC in the late 1960's and early 1970's provided evidence for the physical existence of quarks [19]. The scaling of the proton structure functions indicated that the electrons were scattering off pointlike, charged objects within the proton [20, 21]. Around this time, a quantum field theory of the strong interaction was also developing [22, 23]. It is now called Quantum Chromodynamics (QCD), and incorporates quarks as its fundamental fermions. In QCD, quarks interact via the exchange of spin 1 gauge bosons called gluons, which couple to the colour of the quarks.

The announcement of the discovery of the fourth quark, "charm", in November 1974 had such an impact on the field of particle physics that it is often called the November Revolution. The heavy J/ψ meson was discovered independently by two experiments [24, 25]. The quark model succesfully explained the J/ψ meson as a $^3S_1$ bound state of a charm quark and its antiquark. The subsequent observations of other $c\bar{c}$ states, as well as bound states of charm quarks with lighter quarks, provided strong evidence for the reality of quarks. Furthermore, the charm quark fit naturally into the emerging scheme of fermion generations. The fifth quark, "bottom", was discovered a few years later in a similiar manner, in the form of the $b\bar{b}$ state $\Upsilon(1S)$ [26]. Once again, a variety of bound states involving the new quark were subsequently discovered.

Direct evidence for gluons first appeared in the observation of hadron production in $e^+\ e^-$ annihilation [27]. A notable success of the quark model had been the prediction of hadron production rates at $e^+\ e^-$ colliders, as a quark-antiquark pair can be produced from a virtual photon. The quark and antiquark typically manifest themselves as two collimated "jets" of hadrons, emerging back-to-back from the collision point. However, in some events three jets were observed, and the third jet was consistent with a gluon, having been radiated from the quark or the antiquark.

The modern theory of fundamental particles and forces is known as the Standard Model. It encompasses quantum field theories of the strong, weak and electromagnetic forces, and organizes the fundamental fermions into three generations each of quarks and leptons. They

T_3	Quarks			Leptons		
$+1/2$	$\begin{pmatrix} u \\ d' \end{pmatrix}_L$	$\begin{pmatrix} c \\ s' \end{pmatrix}_L$	$\begin{pmatrix} t \\ b' \end{pmatrix}_L$	$\begin{pmatrix} \nu_e \\ e \end{pmatrix}_L$	$\begin{pmatrix} \nu_\mu \\ \mu \end{pmatrix}_L$	$\begin{pmatrix} \nu_\tau \\ \tau \end{pmatrix}_L$
$-1/2$						

Figure 1.1: The three generations of quarks and leptons as weak isodoublets. T_3 is weak isospin and the L subscripts denote the left-handed helicity state. The primed d', s' and b' denote weak interaction eigenstates, related to the mass eigenstates d, s and b by the CKM matrix.

are listed in Figure 1.1 in the standard format of left-handed weak isodoublets. (This format is due to the symmetry of the weak force, whose gauge bosons couple to fermions with helicity $-\frac{1}{2}$. Helicity is the projection of a particle's spin onto its momentum.) The discovery of the top quark in 1995 [28] completed the third generation of quarks. The list of fundamental fermions appears complete, and QCD is firmly established.

1.2 Quantum Chromodynamics and Hadron Production

Like the precisely tested QED and Electroweak theories, QCD is a local gauge field theory. It is based on the colour $SU(3)$ symmetry. Quarks are colour triplets, having three components of colour, denoted red, green and blue. Antiquarks meanwhile possess three types of analogous anticolour. In terms of group theory, quarks and antiquarks transform respectively under the three-dimensional **3** and $\bar{\mathbf{3}}$ representations of the gauge group $SU(3)$. The gauge bosons of the theory are the gluons, which couple to colour. Gluons themselves are colour octets, transforming under the eight-dimensional representation **8** of $SU(3)$. Since they carry colour, gluons can interact among themselves as the weak vector bosons do. However, like the photon, they are massless.

The six flavours of quarks have a wide range of masses, varying from well under 1 GeV/c^2 for the up, down and strange quarks to about 175 GeV/c^2 for the top quark. Up, down and strange are called light quarks, while charm, bottom and top are called heavy

quarks, for reasons which will become evident below. The strong force acts on quarks independently of their flavour, although their different masses result in different behaviours. Quarks appear pointlike at the scale of $\sim 10^{-18}$ m, the current limit of experimental resolution [29].

Quarks and gluons have never been observed as free particles. This fact is included in QCD as the "colour confinement" hypothesis, which states that naturally occuring states are all colourless. Therefore $q\bar{q}$ and qqq states are allowed because the individual quark colours may combine to form a colour singlet state, whereas qq states, for example, are not[1]. Colour may seem more like a mathematical convenience than a genuine property (it was originally introduced to save the Pauli exclusion principle in certain baryons), but its existence is confirmed by a wide variety of experimental evidence [31]. The strong force between hadrons, such as nucleons in a nucleus, is somewhat different from the strong force between quarks, because hadrons are colourless. It is understood as being carried by colourless mesons, such as the pion, and may be thought of as a "residual" strong force.

In weakly bound systems (hydrogen, for example) the components may be separated if sufficient energy is added, for example in the form of a collision. However, in QCD bound systems, it is generally understood that the binding force is too strong for this to occur, regardless of the amount of energy added. If a hadron is struck hard, the constituent quarks do not simply come free. Rather, additional $q\bar{q}$ pairs are generated from the colour field, and recombine to form more hadrons. This process of generating $q\bar{q}$ pairs in energetic strong interactions is central to models of hadron production.

The strength of the quark-gluon and gluon-gluon couplings are parameterized by the strong coupling constant α_s, analogous to the electromagnetic coupling constant α. The value of α_s depends on the energy scale of the process being studied, a characteristic known as "running". At low energies, $E \lesssim 1$ GeV, the coupling is so strong that perturbation theory breaks down[2]. At higher energies α_s decreases, becoming small enough for perturbation theory to be applied reliably. For example, $\alpha_s(M_Z) \simeq 0.12$. This decrease in α_s

[1] Colourless bound states of gluons may exist, although no candidates have yet been confirmed [30].
[2] One might say that $\alpha_s \to 1$, but it cannot actually be measured in the nonperturbative regime.

implies that in the limit of very high energies quarks behave as free particles, a property known as asympototic freedom. In general, perturbative QCD succesfully describes strong interactions in high energy collisions produced at modern particle colliders.

However, the understanding of strong dynamics at low energies remains a major challenge for particle physics. With perturbation theory unavailable, a variety of theoretical models must be applied to different situations. For example, the original quark model is very useful in classifying hadrons and understanding their quantum numbers. However, it does not include any dynamics and therefore is not able to predict quantities such as masses or scattering cross sections. Meanwhile, several models exist to deal with the process of hadronization, the evolution of a single energetic quark or gluon into a jet of hadrons. These models can be tested in the study of jet production at collider experiments.

The heavy charm and bottom quarks are valuable to the study of QCD because their masses, on the order of 1.5 GeV/c^2 and 4.5 GeV/c^2 respectively, are large enough for perturbation theory to be at least somewhat applicable[3]. The best-understood hadrons are the "quarkonia" states, $c\bar{c}$ and $b\bar{b}$. These are to some extent nonrelativistic systems, and so are analogous to electromagnetically bound systems like hydrogen or positronium. Quarkonia may thus be modeled as a quark and an antiquark moving in a central potential, leaving the form of the potential to be fitted to data [32]. Table 1.1 lists the masses and other properties of the bound quarkonium states, and Figure 1.2 shows the energy levels of charmonium. In this context, "bound" refers to states with mass below the open-flavour threshold: $2m_D$ for charmonia and $2m_B$ for bottomonia. In general, states above this threshold decay rapidly to $D\overline{D}$ (or $B\overline{B}$) and are not so amenable to study as the bound states.

The value of α_s has been measured in $\Upsilon(1S)$ decays to be $\alpha_s(M_{\Upsilon(1S)}) = 0.16 \pm 0.01$ [33]. At the J/ψ mass, it is estimated that $\alpha_s(M_{J/\psi}) \simeq 0.25$ [34]. These values can be used to estimate the quark velocities in the potential model, yielding $v_c^2 \simeq 0.3$ for charmonia and $v_b^2 \simeq 0.1$ for bottomonia[4]. The nonrelativistic approximation is evidently not very accurate for charmonia, but is useful nonetheless.

[3] This is true of the top quark as well, however bound top states are not available for study: top quarks decay too quickly to form bound states.

[4] Velocities are quoted in natural units where the speed of light is defined to be $c \equiv 1$.

Table 1.1: The charmonium states and the known bottomonium states: only states below the open-flavour threshold are listed. The column ($n\,^{2S+1}L_J$) lists the standard spectrosopic notation of principal quantum number and angular momenta. The column J^{PC} lists the values of spin, parity and charge-parity.

Name	Quark content	$n\,^{2S+1}L_J$	Mass (GeV/c^2)	J^{PC}
η_c	$c\bar{c}$	$1\,^1S_0$	2.980	0^{-+}
J/ψ	$c\bar{c}$	$1\,^3S_1$	3.097	1^{--}
χ_{c0} , χ_{c1} , χ_{c2}	$c\bar{c}$	$1\,^3P_{0,1,2}$	3.417, 3.510, 3.556	0^{++}, 1^{++}, 2^{++}
h_c	$c\bar{c}$	$1\,^1P_1$	3.523	1^{+-}
$\eta_c(2S)$	$c\bar{c}$	$2\,^1S_0$	3.594	0^{-+}
$\psi(2S)$	$c\bar{c}$	$2\,^3S_1$	3.686	1^{--}
$\Upsilon(1S)$	$b\bar{b}$	$1\,^3S_1$	9.460	1^{--}
χ_{b0} , χ_{b1} , $\chi_{b2}(1P)$	$b\bar{b}$	$1\,^3P_{0,1,2}$	9.860, 9.982, 9.913	0^{++}, 1^{++}, 2^{++}
$\Upsilon(2S)$	$b\bar{b}$	$2\,^3S_1$	10.023	1^{--}
χ_{b0} , χ_{b1} , $\chi_{b2}(2P)$	$b\bar{b}$	$2\,^3P_{0,1,2}$	10.232, 10.255, 10.269	0^{++}, 1^{++}, 2^{++}
$\Upsilon(3S)$	$b\bar{b}$	$3\,^3S_1$	10.355	1^{--}

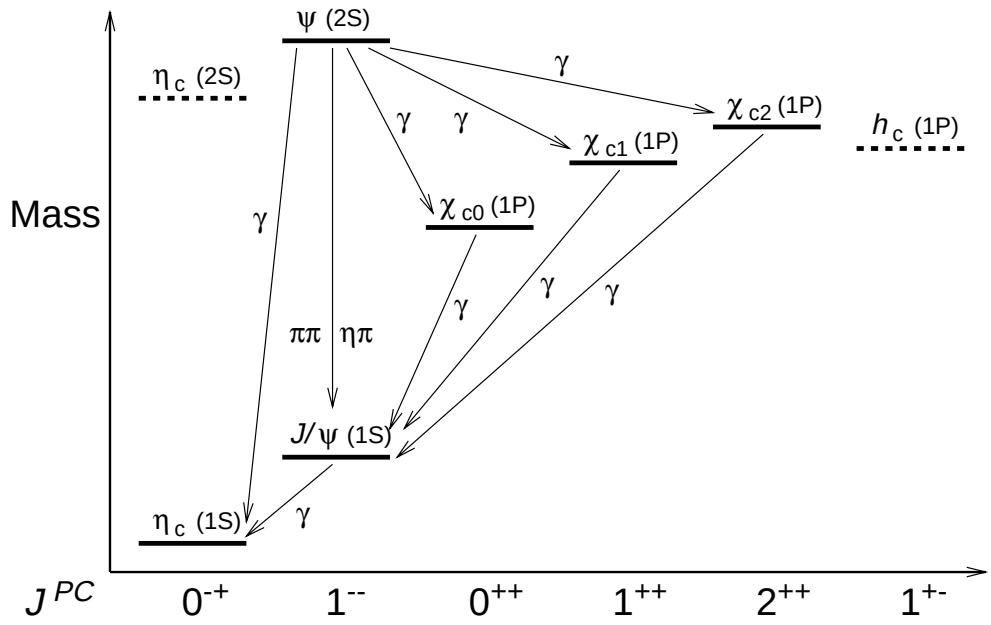


Figure 1.2: The bound charmonium states. The $\eta_c(2S)$ and $h_c(1P)$ mesons have only been tentatively identified. Arrows denote some common transitions between states.

The production of heavy quarks in high-energy particle collisions is an active field of research. Perturbative QCD can be used to make predictions of inclusive heavy flavour production, i.e. charm, bottom and top production [35]. Provided the colliding beam particles have sufficient energy, heavy quarks may be produced in a variety of collisions, for example at e^+e^-, ep and $p\bar{p}$ colliders. The highest energies are currently attained in $p\bar{p}$ collisions, where heavy quark pairs are produced by $q\bar{q}$ and gg interactions between the components of the proton and antiproton. At high energies, due to asymptotic freedom the incoming hadrons behave approximately as beams of independent quarks and gluons. The momentum distributions of the quarks and gluons within a hadron are characterized by a set of measured parton distribution functions, which depend on the energy scale of the production process. The inclusive heavy quark production cross section thus depends on the parton distribution functions and the amplitudes for $q\bar{q}$ and gg collisions to produce heavy quarks.

The production cross sections for a particular hadron, such as the J/ψ meson studied in this dissertation, in various collider environments may also be predicted and measured. The

study of quarkonium production in high-energy collisions is useful because it involves QCD processes at different energy scales. First, the heavy quark-antiquark pair is produced in an energetic collision, then the pair binds together into a quarkonium state. If the energy scales of these two steps differ sufficiently, the cross section for the production of a quarkonium meson H may factor into two parts: 1) the cross section for inclusive production of the heavy quark pair $Q\overline{Q}$, which can be calculated perturbatively, and 2) the probability for the $Q\overline{Q}$ pair to evolve into the bound state H, which must be modeled. The technique of separating a production process into two stages is formally known as factorization [35] and is central to QCD calculations of high-energy collisions. The validity of the factorization of the quarkonium production cross section depends on the energy scales and interactions involved in the two steps, and must ultimately be tested experimentally.

1.3 Charmonium Production

There are three widely known approaches to describing the evolution of a heavy quark-antiquark pair into a bound state. These approaches, listed below, deal with the probability for a $Q\overline{Q}$ pair produced in a particular colour and angular momentum state to form a particular quarkonium meson. If factorization is valid, these probabilities are independent of the $Q\overline{Q}$ production process. For example, charmonium production is studied in several experimental environments including Z^0 decays, B-hadron decays, ep collisions, $p\bar{p}$ collisions and fixed target hadron experiments. While the perturbative $c\bar{c}$ production cross section is different for each process, the subsequent binding process is the same, provided factorization holds.

The Colour Evaporation Model (CEM) [36] is a relatively simple model, in which there is no correlation of colour and angular momentum quantum numbers between the initial $Q\overline{Q}$ state and the final quarkonium state. It is assumed that soft gluon emission during the binding process alters the quantum numbers to arrive at the appropriate final state. Thus any $c\bar{c}$ pair with invariant mass between $2m_c$ and the open flavour threshold $2m_D$ will form a charmonium state. There is a fixed probability to form each quarkonium state,

so the CEM predicts that the ratio of quarkonia cross sections (for example $\sigma_{J/\psi} : \sigma_{\psi(2S)}$ or $\sigma_{\chi_{c1}} : \sigma_{\chi_{c2}}$) is the same for any production process. However, the actual values are not predicted and must be measured experimentally.

The Colour Singlet Model (CSM)[5] takes the opposite approach, assuming that each quarkonium state can only be produced by a $Q\overline{Q}$ pair in the same colour and angular momentum state as that quarkonium. Therefore a J/ψ meson, for example, can only be derived from a $c\bar{c}$ pair created in a $^3S_1$ colour-singlet state. The attractive feature of the CSM is that it makes definite quantitative predictions for production cross sections, because the binding probability is related to the quarkonium wavefunction from the potential model introduced previously. In the potential model, the amplitude for the quark and antiquark to overlap, $R(0)$, is related to the quarkonium decay width[6]. For example, $R_\psi(0)$ (where ψ stands for J/ψ or $\psi(2S)$ as appropriate) can be measured in leptonic ψ decays:

$$\Gamma(\psi \to e^+e^-) \simeq \frac{4\alpha_s^2}{9m_c^2}|R_\psi(0)|^2 \tag{1.1}$$

The derived value of $|R_\psi(0)|^2$ then appears in the CSM formula for inclusive ψ production:

$$d\sigma(\psi + X) = d\hat{\sigma}(c\bar{c}\ [\underline{1},^3S_1] + X)\ \cdot\ |R_\psi(0)|^2 \tag{1.2}$$

Here $d\hat{\sigma}(c\bar{c}\ [\underline{1},^3S_1] + X)$ is the inclusive cross section for producing the $c\bar{c}$ in the correct $[\underline{1},^3S_1]$ state[7], which is calculated perturbatively.

One of the important predictions of the Colour Singlet Model concerns the differential production cross sections versus transverse momentum in high-energy hadronic collisions. The transverse momentum of a produced particle is defined as $P_T \equiv P\sin\theta$, where θ is the polar angle with respect to the beam direction. It is a natural quantity to measure at a collider, because high-P_T particles are well separated from the remnants of the colliding beams. Various perturbative processes contribute to the total cross section, two of which are shown in Figure 1.3. The leading order process in α_s is expected to dominate at lower P_T. It is an example of a "fusion" process, in which the quarkonium is produced in the collision

[5] Some references for the CSM can be found in [37], which reviews all the production models discussed here.

[6] For P-wave quarkonia the first derivative of R at the origin is used, and so on for higher-L states.

[7] The $\underline{1}$ denotes the colour singlet state. A colour octet state would be written $\underline{8}$.

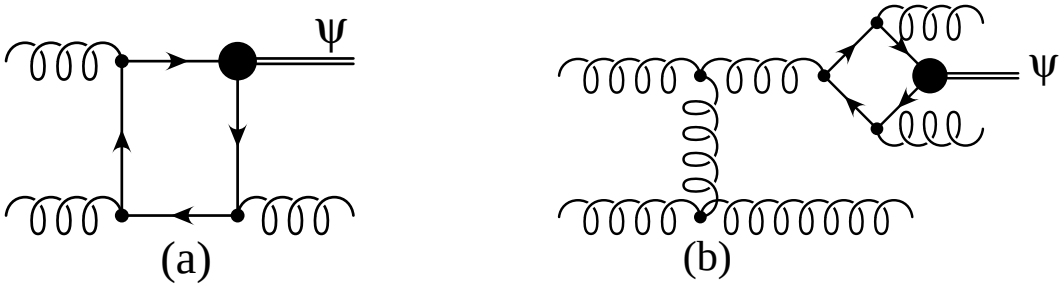


Figure 1.3: Examples of ψ production in the Colour Singlet Model. The leading order diagram is shown in (a) and occurs at order α_s^3; it is a two-gluon fusion process. The large "blob" vertex represents the nonperturbative binding process; the $c\bar{c}$ pair entering the blob must be in a $[\underline{1},^3S_1]$ state. A gluon fragmentation diagram is shown in (b). In both cases an outgoing gluon balances the transverse momentum of the ψ meson.

of two incoming partons. At higher P_T, on the other hand, "fragmentation" processes are expected to dominate due to their shallower P_T dependence [38]. Fragmentation refers to the production of a quarkonium meson in the jet produced by a single high P_T particle. As will be discussed below, the measured cross sections disagree with CSM predictions, being significantly higher.

The third and most sophisticated theoretical approach to quarkonium production is known as the NRQCD factorization formalism[8] [39]. Nonrelativistic QCD (NRQCD) [40] is an effective field theory [41] which treats quarkonium as an approximately nonrelativistic system. NRQCD makes systematic corrections to this approximation using an expansion series in v, the velocity of the heavy quark in the quarkonium rest frame. When applied to production, this implies that $Q\overline{Q}$ pairs produced with one set of quantum numbers can evolve into a quarkonium state with different quantum numbers, by emitting low energy gluons. The probabilities of such transitions are suppressed by specific powers of v. This is in contrast to the CSM, in which such transitions have zero probability.

The NRQCD factorized cross section for inclusive production of a quarkonium state H

[8]Sometimes the phrase "Colour Octet Model" (COM) is encountered when colour-octet mechanisms are considered. However, the COM lacks the formal organization of energy scales that NRQCD provides.

has the form:

$$d\sigma(H+X) = \sum_n d\hat{\sigma}(Q\overline{Q}[n]+X)\cdot\langle\mathcal{O}_n^H\rangle \tag{1.3}$$

Here $d\hat{\sigma}$ is the inclusive cross section for producing a $Q\overline{Q}$ pair in the colour and angular momentum state n, with "small" relative velocity[9]. The number $\langle\mathcal{O}_n^H\rangle$ is known as the "matrix element" for the transition of a $Q\overline{Q}$ pair in state $[n]$ to the quarkonium H along with light hadrons whose energies in the rest frame of H are of order $m_Q v_Q^2$ [37]. The matrix elements are dimensionful quantities, so powers of m_Q are understood in the denominator of Equation 1.3 to cancel the dimensions properly. NRQCD cannot predict the exact values of the matrix elements, but it can estimate their order of magnitude: it predicts that each matrix element is proportional to a specific power of v.

The matrix elements are formally defined in NRQCD, although a full discussion of this is well beyond the scope of this thesis. They have the form [39]

$$\langle\mathcal{O}_n^H\rangle \;=\; \langle 0|\;\chi^\dagger\;\mathcal{K}_n\;\psi\;(a_H^\dagger a_H)\;\psi^\dagger\;\mathcal{K}_n'\;\chi\;|0\rangle \tag{1.4}$$

where ψ and χ are Pauli spinor operators which destroy heavy quarks and create heavy antiquarks respectively. The operator a_H creates the quarkonium[10] along with light hadrons. The factor $\mathcal{K}_n$ contains colour and spin matrices and covariant derivatives, depending on the quantum numbers in n. Equation 1.4 is therefore describing a projection of a $Q\overline{Q}$ pair onto a quarkonium state. Although there is an unlimited number of matrix elements with various values of n, in practice only those at lowest order in v are considered. This can be illustrated by the expansion in powers of v of the Fock state of the J/ψ meson:

$$\begin{aligned}|J/\psi\rangle \;=\;& O(1)\;|c\bar{c}[\underline{1},^3S_1]\rangle \;+\; O(v)\;|c\bar{c}[\underline{8},^3P_J]g\rangle \;+\; O(v^2)\;|c\bar{c}[\underline{8},^1S_0]g\rangle \\ &+\; O(v^2)\;|c\bar{c}[(\underline{1},\underline{8}),^3S_1]gg\rangle \;+\; O(v^2)\;|c\bar{c}[(\underline{1},\underline{8}),^3D_J]gg\rangle \;+\;\cdots\end{aligned} \tag{1.5}$$

The velocity scaling of a particular matrix elements depends on the scaling of the related term in this expansion. Only those matrix elements at small powers of v are included in calculations.

[9] In calculating $d\hat{\sigma}$, the relative velocity of the quark and antiquark is restricted to sufficiently small values, of order v or less, that they will not move apart and hadronize separately.

[10] Note that a_H as written here implies a sum over helicity states, which must instead be separated when considering polarization.

Table 1.2: Values of some NRQCD matrix elements, fitted from CDF cross section data and the ψ leptonic widths, from [45]. The expected scaling orders in quark mass and velocity from NRQCD rules are also listed. The relative weightings of the matrix elements $\langle \mathcal{O}_8^{\psi}(^1S_0)\rangle$ and $\langle \mathcal{O}_8^{\psi}(^3P_0)\rangle$ are chosen to be $r_{J/\psi} = 3.47$ and $r_{\psi(2S)} = 2.56$ on phenomenological grounds.

Matrix element	J/ψ value (GeV^3)	$\psi(2S)$ value (GeV^3)	Scaling order
$\langle \mathcal{O}_1^{\psi}(^3S_1)\rangle$	$(7.6 \pm 0.5) \times 10^{-1}$	$(4.4 \pm 0.4) \times 10^{-1}$	$m_c^3 v_c^3$
$\langle \mathcal{O}_8^{\psi}(^3S_1)\rangle$	$(3.9 \pm 0.6) \times 10^{-3}$	$(6.2 \pm 1.0) \times 10^{-3}$	$m_c^3 v_c^7$
$\frac{1}{3}\langle \mathcal{O}_8^{\psi}(^1S_0)\rangle + \frac{r}{3m_c^2}\langle \mathcal{O}_8^{\psi}(^3P_0)\rangle$	$(2.2 \pm 0.2) \times 10^{-2}$	$(0.6 \pm 0.2) \times 10^{-2}$	$m_c^3 v_c^7$

The leading order (in v) matrix element for ψ production is $\langle \mathcal{O}_1^{\psi}(^3S_1)\rangle$, which corresponds to the CSM case: the $c\bar{c}$ pair is produced in a $[\underline{1},^3S_1]$ state. In NRQCD this matrix element is of order v_c^3, and its value can be measured from the J/ψ leptonic decay width, in analogy with Equation 1.1. The next matrix elements involve colour octet initial states and occur at order v_c^7; they are $\langle \mathcal{O}_8^{J/\psi}(^3P_J)\rangle$, $\langle \mathcal{O}_8^{J/\psi}(^1S_0)\rangle$ and $\langle \mathcal{O}_8^{J/\psi}(^3S_1)\rangle$. Their values have been fitted from production cross sections in $p\bar{p}$ collisions, as have analogous matrix elements for other quarkonia [42, 43, 44, 45]. The short-distance cross section $d\hat{\sigma}$ associated with each matrix element has a certain P_T dependence, so the matrix elements can be fitted to the observed P_T spectrum. The matrix elements $\langle \mathcal{O}_8^{J/\psi}(^1S_0)\rangle$ and $\langle \mathcal{O}_8^{J/\psi}(^3P_J)\rangle$ cannot be separately determined because their cross sections have the same P_T dependence, so their weighted sum is fitted. NRQCD spin symmetry relations, in this case

$$\langle \mathcal{O}_8^{\psi}(^3P_J)\rangle = (2J+1) \cdot \langle \mathcal{O}_8^{\psi}(^3P_0)\rangle \tag{1.6}$$

are used to reduce the number of free parameters in the fits [46]. Table 1.2 lists one set of recently derived values for the above matrix elements.

If the above formalism is valid, then any J/ψ production process should yield the same fitted values for the matrix elements[11]. This universality may however be limited in certain regions of phase space [47] and by the details of the soft gluon emission process [48]. The attempt to understand quarkonium production in all types of experimental environments

[11] NRQCD can also be applied to quarkonium decays, with different but related matrix elements [39].

in the NRQCD framework is an ongoing one.

In high-energy $p\bar{p}$ collisions, there are three distinct types of charmonium production. The first is the type discussed above, in which the meson is produced in the collision of the proton and antiproton. This is called direct production. The second is in the decay of heavier charmonia, for example the production of a J/ψ meson in the decay of a χ_c or $\psi(2S)$ meson, and is known as feeddown. The third, B-decay, is in the weak decay of b-flavoured hadrons: B^+, B^0, B_S^0, Λ_b and their antiparticles. This third type is distinguished from the first two by the relatively long lifetime of B-hadrons, about 1.5 ps. The decay vertex of a B-hadron is usually far enough from the primary $p\bar{p}$ interaction point to be identified as a displaced secondary vertex[12]. The first two types of charmonium production occur at the primary interaction point and are collectively known as prompt production.

The production cross sections of several quarkonia in high-energy $p\bar{p}$ collisions have been measured within the past five years by the Collider Detector at Fermilab (CDF) collaboration at the Fermilab Tevatron [49, 50, 51]. The measured differential cross sections $d\sigma/dP_T$ for direct J/ψ and $\psi(2S)$ production are of particular significance. The direct cross section has been experimentally separated from those of feeddown and B-decay[13]. The measured cross sections are shown in Figure 1.4. The direct cross sections disagree with CSM predictions, being on the order of fifty times larger for both the J/ψ and $\psi(2S)$. This has effectively ended consideration of the CSM as a plausible model.

The NRQCD factorization formalism meanwhile uses the measured cross sections to fit for the relevant matrix elements $\langle \mathcal{O}_8^{\psi}(^3P_J)\rangle$, $\langle \mathcal{O}_8^{\psi}(^1S_0)\rangle$ and $\langle \mathcal{O}_8^{\psi}(^3S_1)\rangle$. The fit to the data is acceptable in shape and obtains values reasonably consistent with the expected powers of v. At high P_T ($P_T \gg m_c$) the dominant process in NRQCD is the fragmentation of a single gluon to a $c\bar{c}$ pair in a $[\underline{8},^3S_1]$ state [52]. This process is illustrated in Figure 1.5. In comparison to the colour singlet fragmentation process in Figure 1.3(b), this occurs at a higher order of v_c (v_c^7 versus v_c^3) but at a lower order of α_s (α_s^3 versus α_s^5). Thus it is indeed

[12] A sequential decay such as $B \to \chi_c \to J/\psi$ is classified as B-decay, not feeddown, because it occurs at a displaced vertex.

[13] Since the $\psi(2S)$ is the heaviest bound $c\bar{c}$ state, it has no feeddown: all prompt $\psi(2S)$ production is direct.

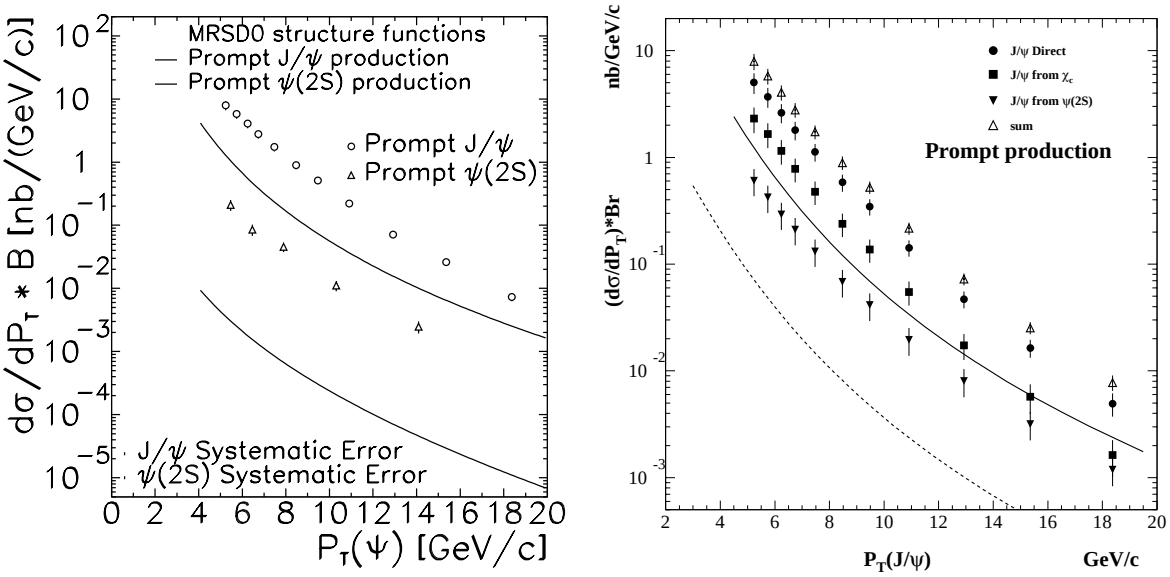


Figure 1.4: Differential ψ production cross sections in $p\bar{p}$ collisions, multiplied by the branching ratio to $\mu^+\mu^-$. CDF measurements (points) are compared with CSM predictions (lines). Left plot: prompt J/ψ and $\psi(2S)$ production (the J/ψ prediction is the higher of the two curves). Right plot: separated sources of prompt J/ψ production (lower line is direct CSM prediction, upper line is J/ψ from χ_c prediction, with colour octet mechanisms included). From [50] and [51].

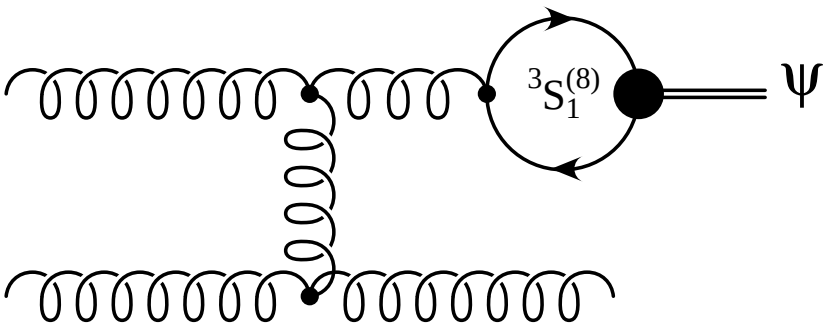


Figure 1.5: Schematic diagram of gluon fragmentation to a $c\bar{c}$ $[\underline{8},^3S_1]$ pair, followed by binding (the blob) into a ψ meson. Light hadrons with low energies may also be emitted during the binding but are not shown. The fragmenting gluon could also be produced by other perturbative QCD processes.

plausible that the colour octet process could explain the observed direct cross sections.

1.4 Predictions for ψ Polarization

This explanation of the CDF measurements has lead to a striking prediction concerning ψ polarization in $p\bar{p}$ collisions, which may be tested experimentally. As ψ mesons are spin 1 particles, they may possess transverse polarization (helicity ± 1), longitudinal polarization (helicity 0), or some combination of the two. The NRQCD factorization formalism predicts that at high P_T, directly produced ψ mesons are mostly transversely polarized. References [43, 53, 54, 55, 56, 57] document the introduction and refinement of this prediction. It derives from the expected dominance of the gluon fragmentation mechanism to $c\bar{c}$ $[\underline{8},^3S_1]$. For $P_T \gg m_\psi$, the fragmenting gluon is almost on shell, and is therefore transversely polarized, up to corrections of order m_ψ^2/E^2 [53]. The $c\bar{c}$ pair inherits this polarization, and NRQCD predicts that the binding process will preserve the polarization as the ψ meson forms.

In contrast, the Colour Evaporation Model assumes that those processes of soft gluon emission in which a quark spin flips are unsuppressed. Thus any spin alignment of the $c\bar{c}$ pair

is lost in the binding process, and the ψ mesons are predicted to be produced unpolarized in all experiments [36].

The polarization of ψ mesons determines their angular decay distributions. In the case of leptonic decays, e^+e^- and $\mu^+\mu^-$, the decay angle of interest lies between the positive lepton momentum in the ψ rest frame and the ψ momentum in the hadronic ($p\bar{p}$) centre-of-mass frame. This angle, referred to as θ^*, has the distribution

$$\frac{d\Gamma}{d\cos\theta^*} \propto \frac{3}{2(\alpha+3)}(1+\alpha\cos^2\theta^*) \tag{1.7}$$

where the variable α is known as the polarization parameter. Fully transverse polarization is characterized by $\alpha = +1$ and fully longitudinal polarization by $\alpha = -1$. Values in between correspond to mixtures, with $\alpha = 0$ denoting no polarization (and an isotropic $\cos\theta^*$ distribution). Quantitative predictions for the dependence of α on P_T have been made for direct ψ production [43, 56, 57]. One typical prediction is shown in Figure 1.6. All predictions display an increase in α at high P_T. However, several effects are taken into account which reduce α below +1. Firstly, gluon fragmentation to the $^3S_1$ colour octet state is not the only type of production; other matrix elements contribute, especially in the lower P_T range where fragmentation does not dominate. Some of these channels, such as those with the $^1S_0$ intermediate state, do not yield polarized charmonia. Secondly, the fragmenting gluons are off-shell and are thus not completely transverse. Thirdly, there are contributions to the fragmentation process at higher orders in α_s which may alter the spin configuration of the $c\bar{c}$ pair [55]. Lastly, the binding process may not perfectly preserve the $c\bar{c}$ spin alignment; in NRQCD there are spin-symmetry breaking mechanisms which are suppressed by the order of v^4 relative to the leading-order processes [55].

Predictions for $\alpha(P_T)$ are generally very similar or identical for direct J/ψ and direct $\psi(2S)$ production. Slight differences may arise from the different J/ψ and $\psi(2S)$ matrix elements used in the prediction, which are usually fitted from data on $d\sigma/dP_T$. The general prediction of increasing transverse polarization also applies to Υ production at $P_T \gg m_\Upsilon$, but very few Υ mesons are produced at such high transverse momentum. The NRQCD factorization formalism has also been applied to χ_c [57] and χ_b [58] polarization, but these

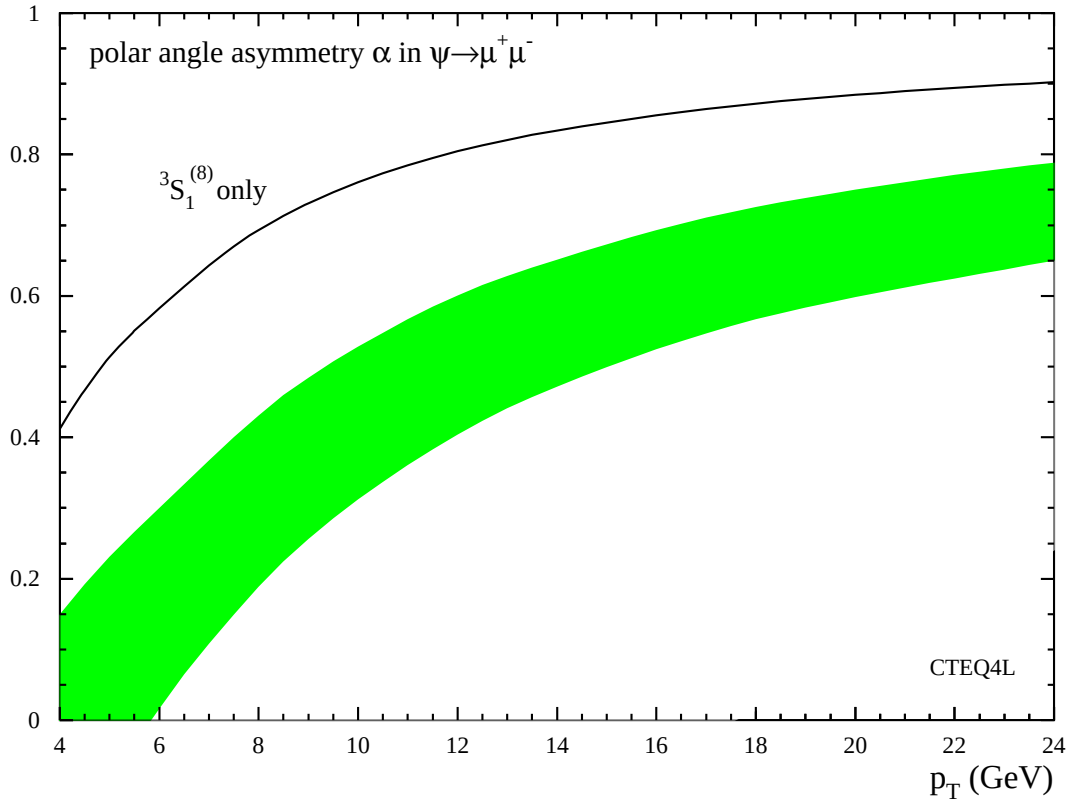


Figure 1.6: An NRQCD factorization prediction for the polarization parameter α of directly produced ψ mesons, as a function of ψ transverse momentum. The line denotes the $\langle \mathcal{O}_8^{\psi}(^3S_1)\rangle$ mechanism alone; the shaded band includes other mechanisms as well as theoretical uncertainties from the matrix element values. From [43].

quantities are rather more difficult to measure.

1.5 Dissertation Overview

This dissertation describes the measurement of the polarization of J/ψ mesons produced in $p\bar{p}$ collisions at a centre-of-mass energy of 1.8 TeV. (This measurement has been submitted for publication [59].) The collisions were produced by the Tevatron proton-antiproton collider, located at Fermi National Accelerator Laboratory in Batavia, Illinois, U.S.A. The collision data was collected by the Collider Detector at Fermilab (CDF), which is one of the two detectors operating at the Tevatron.

Chapter 2 describes CDF and the Tevatron in detail. Chapter 3 describes the data sample used to perform this analysis. It is worth noting that other $^3S_1$ quarkonia, such as the $\psi(2S)$ and $\Upsilon(1S)$ mesons can also be (and have been) analyzed for polarization. The $\psi(2S)$ has the advantage of an absence of feeddown, while the $\Upsilon(1S)$ has no contamination from B-decay. However, the advantage of the J/ψ analysis is the large number of $J/\psi \to \mu^+\mu^-$ decays recorded by CDF. The number of events in the J/ψ data sample numbers in the hundreds of thousands, which is necessary for good statistical precision.

In Chapter 4 the details of the polarization analysis are described. The angular distribution of the muons in the J/ψ decays is used to measure the polarization. Furthermore, the polarization of promptly produced J/ψ mesons is separated from the polarization of those produced in B-hadron decays, using measured J/ψ decay lengths.

Chapter 5 compares the measurement with theoretical predictions, attempts to draw some conclusions, and considers the possibilities for similar measurements in the future. The three appendices contain a discussion of the J/ψ decay angle distribution, a brief description of my contribution to the CDF Run 2 upgrade, and the CDF author list.

Chapter 2

Accelerator and Detector

A particle accelerator and a detector together form the basis of a high energy physics experiment. The types of particles accelerated, and the energy which they attain, determine what areas of particle physics can be studied. During the 1970's, both CERN[1] and Fermilab[2] began to develop high energy proton-antiproton colliders. These machines are synchrotrons [60] in which counter-rotating p and $\bar{p}$ beams are accelerated in the same set of magnets and collide head-on [61, 62]. In these collisions, due to their composite nature, the proton and antiproton behave much like collections of quarks and gluons with a broad spectrum of energies. A wide variety of hard interactions are thus possible, but only a fraction of the total $p\bar{p}$ centre-of-mass energy is available for each interaction. Protons are nevertheless the particle of choice for the highest-energy accelerators, since they lose far less energy to synchrotron radiation than do electrons.

At the same time, work began on a Collider Detector Facility (the original name of CDF) to record the collisions produced by the new Fermilab machine. CDF was designed to observe the variety of event signatures produced by hard parton-parton collisions, such as jets, high P_T muons and electrons, and the missing transverse energy characteristic of neutrinos. This chapter describes CDF and the Tevatron as they were configured during 1992-95, when the data for this analysis was recorded.

[1] CERN is the European laboratory for nuclear and particle physics research, and is located in Geneva, Switzerland.

[2] The Fermi National Accelerator Laboratory, located in Batavia IL, U.S.A.

2.1 The Fermilab Tevatron

The Tevatron is a superconducting synchrotron and is at present the highest energy particle collider in the world. It operates with proton and antiproton beams of 900 GeV each, for a total centre-of-mass energy of $\sqrt{s} = 1.8$ TeV. The first $p\bar{p}$ collisions were produced in 1985, and the first data run took place in 1987. During Run 1 in 1992-96 the Tevatron operated at luminosities in the range $(2 - 27) \times 10^{30}$ cm^{-2}s^{-1} [63].

A series of lower energy accelerators is responsible for providing proton and antiproton beams for injection into the Tevatron [64]. Figure 2.1 shows the layout of the accelerators at Fermilab. The acceleration process begins in the Pre-Accelerator, where protons are obtained from hydrogen gas and converted into H^- ions in an ion source. A Cockcroft-Walton [65] power supply generates a 750 kV potential difference, which accelerates the ions into a linear accelerator (Linac). At the core of the Linac is a 175 metre long series of copper drift tubes. A radiofrequency potential difference is applied to alternating tubes, such that the ions are accelerated each time they traverse a gap between tubes. At the end of the Linac, the ion beam has a kinetic energy of 400 MeV[3]. At this point, before reaching the next machine, the ions pass through a carbon foil which strips both the electrons from the proton.

The next accelerator in the process is an alternating gradient synchrotron [66] called the Booster. It has a radius of 75 metres and raises the proton energy to 8 GeV. The Booster is "rapid cycling", completing its acceleration cycle at a rate of 15 Hz, and loads twelve proton bunches at a time into the Main Ring. The Main Ring, a synchrotron 1 km in radius, was the original major accelerator at Fermilab. It contains over 1000 dipole, quadrupole and correcting magnets. Six straight sections contain the beam injection and transfer lines, experimental areas and radio frequency (RF) accelerating cavities. The Main Ring accelerates protons to 150 GeV and then transfers them into the Tevatron.

Antiproton production [67] is accomplished by extracting 120 GeV protons from the Main Ring and directing them onto a nickel target[4]. Antiprotons produced in the resulting

[3] Prior to an upgrade in 1993 the Linac energy was 200 MeV.
[4] Copper and rhenium targets have also been used.

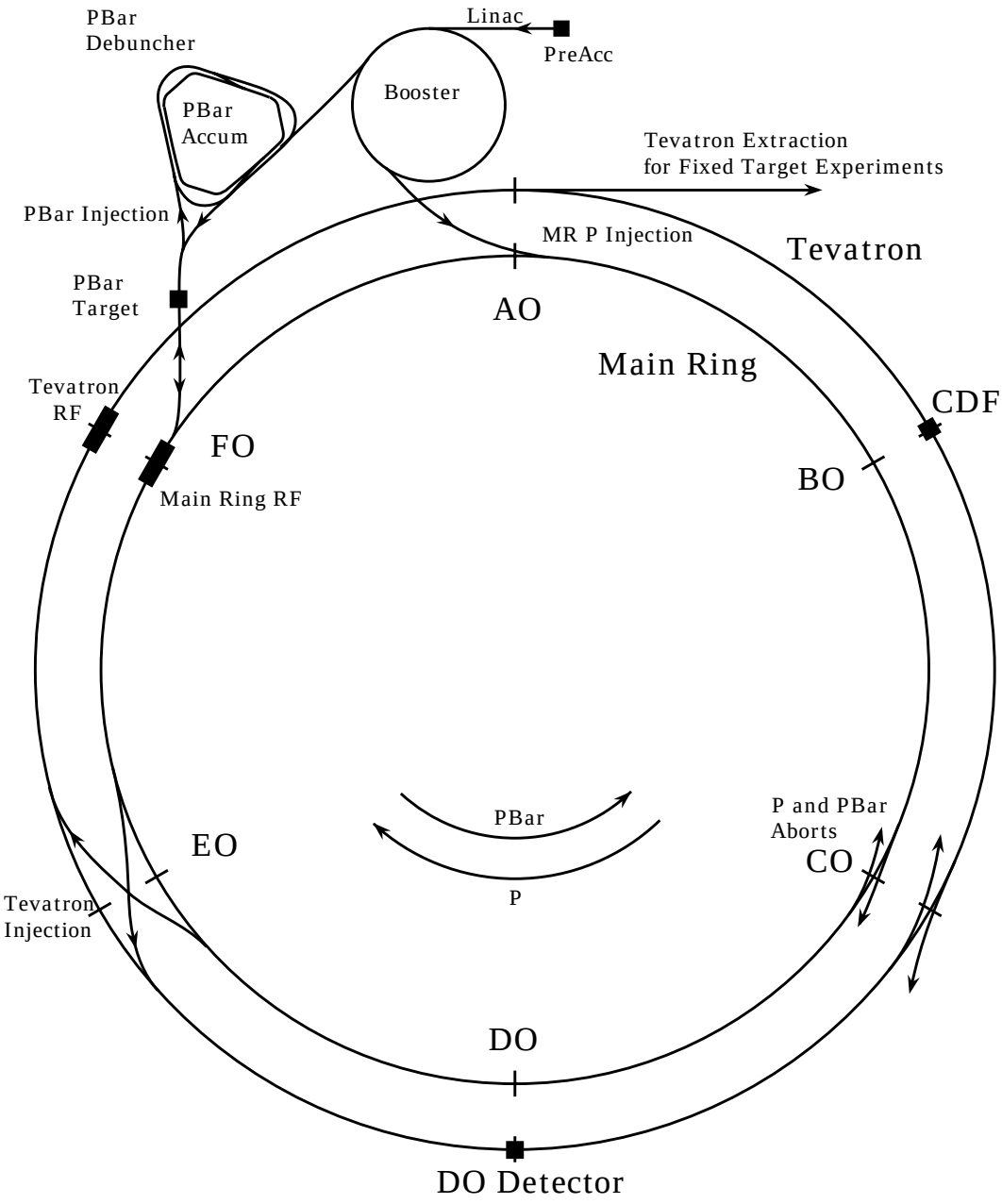


Figure 2.1: An overview of the Fermilab accelerator complex. The Main Ring and Tevatron occupy the same tunnel; they are not drawn to scale here.

proton-nucleus collisions are focused using a cylindrical lithium lens carrying a pulsed 0.4 MA axial current. They enter the Debuncher [68], a storage ring similar in size to the Booster. The Debuncher changes the bunches of antiprotons into a smooth beam, in effect exchanging the spread in antiproton energies for a spread in time. It then reduces the beam emittance using the process of stochastic cooling [69], making the antiproton beam suitable for efficient extraction and acceleration. The antiprotons are transferred to the Accumulator Ring [70], concentric with the Debuncher, where successive injections are stacked together and cooled further. The kinetic energy in both rings is 8 GeV. The Accumulator typically stores antiprotons at a rate of about 7×10^{10} per hour [71]. The antiproton production rate is a significant limiting factor on the luminosity of the Tevatron.

The Tevatron [72] is located in the same tunnel as the Main Ring, directly underneath it. The layout of the magnet lattice is similar to the Main Ring, but the magnet coils are made from superconducting NbTi [73] cooled to 4.6 K using liquid helium. The dipole magnets achieve a bending field of 4.4 Tesla. The Tevatron possesses eight RF cavities which operate at 53 MHz, the same frequency as the Main Ring cavities. Four of the eight cavities add 1/3 MeV each to the proton energy per pass, and the other four do the same for the antiprotons. The Tevatron can operate either in fixed-target mode, providing proton beams up to 800 GeV, or as a proton-antiproton collider. For the latter, the Tevatron is first filled with six proton bunches circulating clockwise. When sufficient numbers of antiprotons have built up in the Accumulator, they are transferred to the Main Ring, accelerated to 150 GeV and injected into the Tevatron in six bunches circulating counterclockwise. A bunch typically contains 2.5×10^{11} protons or 7.5×10^{10} antiprotons [71]. Both beams are then accelerated up to 900 GeV. At the B0 and D0 sections of the ring, where the CDF and D0 detectors are located, the beams are focused down to small diameter by low-β quadrupole magnets. The bunches cross at these collision points once every 3.5 μs. The beams circulate and the detectors take data for several hours, until the luminosity drops off and new antiproton bunches are ready, whereupon the process starts over.

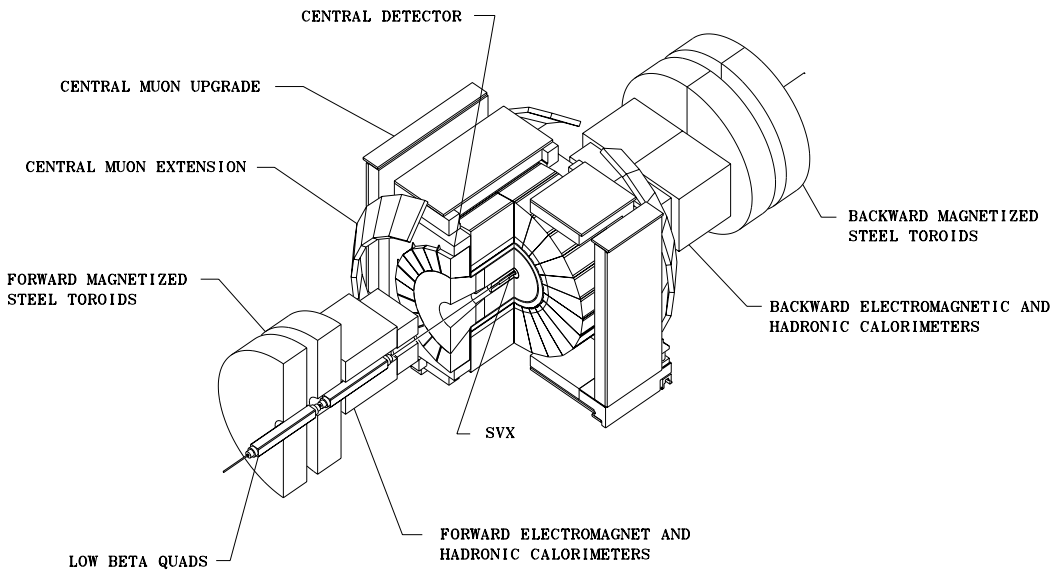


Figure 2.2: An isometric view of the CDF detector in Run 1, showing its axial and forward/backward symmetry. The detector stands about 10 metres high and 26 metres long. The cutaway view shows the interior of the detector.

2.2 The CDF Detector

The Collider Detector at Fermilab (CDF) is the product of many years of work by several hundred people. It represents in many ways a typical modern detector design [74]. The purpose of the detector is to surround the $p\bar{p}$ interaction point and measure the four-momenta and identity of individual particles and jets. However, because of the geometry of the colliding beams, it is not possible to provide complete (4π steradian) solid angular coverage around the interaction point. Rather, the emphasis is on central coverage, extending as far forward in pseudorapidity as is practical. In collider detector terms, "central" refers to the direction orthogonal to the beamline, whereas "forward" implies small angles with respect to the beamline. Therefore the central region is around $\theta \simeq 90^\circ$, where θ is the polar angle with respect to the proton beam direction. For physical reasons, pseudorapidity is more commonly used than polar angle: it is defined as $\eta \equiv -\ln(\tan\theta/2)$.

CDF is arranged in a cylindrical geometry, therefore it is both axially and forward-backward symmetric (see Figure 2.2). Construction began in the early 1980's, and it was first operated in 1985 and again in 1987-89. Reference [75] gives an overview of the detector

at that time. CDF consists of a series of particle detection systems arranged concentrically around the beamline. Figure 2.3 shows the layout of these systems in detail. The Central Tracking Chamber (CTC) is a drift chamber used for charged particle tracking in three dimensions, and is located inside a solenoidal magnet which provides a 1.4 T magnetic field. Interior to the CTC is a time projection chamber used to identify $p\bar{p}$ collision vertices. Outside the solenoid is a set of calorimeters, covering the central, intermediate and forward regions of pseudorapidity. Finally, drift chambers for muon identification are located outside the calorimeters, in the central and forward regions. The entire apparatus weighs about 5000 tons. It is situated in an assembly hall for maintenance, and moved into path of the Tevatron in the collision hall for taking data. A three level trigger system selects events for readout by a data acquisition system, and data is stored on magnetic tape.

For Run 1 of the Tevatron in 1992, the detector received several upgrades. These included a silicon microvertex detector, a new vertex time projection chamber and extensions to the muon system. This brought the total number of readout channels in CDF to about 150,000. The sections below describe the detector in its Run 1 configuration. The systems used in this analysis — the CTC, the silicon vertex detector and the central muon chambers — are covered in the most detail. (As a point of interest, it is worth mentioning that CDF is currently undergoing further upgrades for Run 2 in 2001.)

2.2.1 Solenoid magnet

CDF is at heart a magnetic spectrometer, so naturally the first part to describe is the magnet. It is a superconducting solenoid 4.80 m in length and 2.97 m in inner diameter [77], oriented along the beamline. All of the tracking systems are located interior to the solenoid. The axial magnetic field causes the trajectories of charged particles to curve, which allows a measurement of their momentum transverse to the beamline. The superconducting coil is designed to provide a 1.5 Tesla field at 5000 Amperes, but during Run 1 it was operated at 1.41 Tesla.

The coil consists of niobium titanium wires embedded in copper, surrounded by a stabilizing jacket of high purity aluminum. It is wrapped into a single layer of 1164 turns.

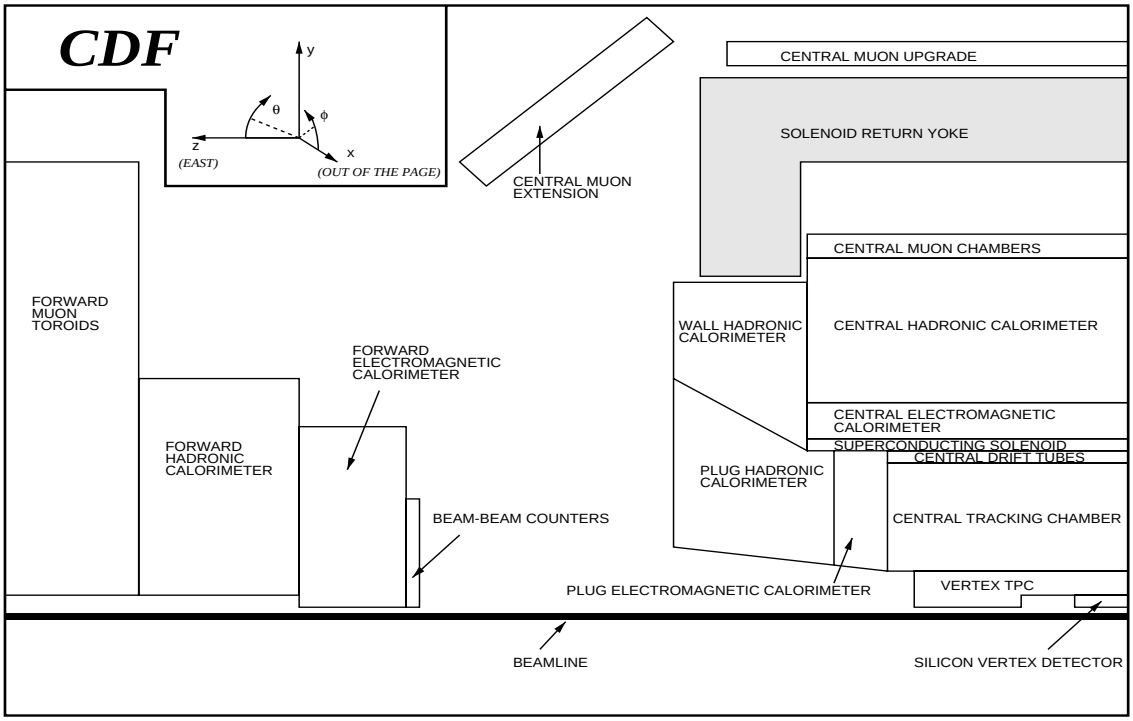


Figure 2.3: One quadrant of the CDF detector in Run 1. The nominal $p\bar{p}$ interaction point is on the beamline at the right end of the diagram. In the coordinate system, z denotes distance along the beamline from the centre of the detector. The protons move in the $+z$ direction, θ denotes polar angle from the proton beam and ϕ denotes azimuthal angle. The two halves of CDF at positive and negative z are called the east and west halves respectively. From [76].

Two phase helium cools the coil to an operating temperature of about 4.5 K. The coil is contained within a cylindrical structure which contains the cryostatic system as well as aluminum alloy supports, which support the coil against the large magnetic force pointing radially outward. The magnetic flux return outside the coil is provided by an iron yoke and parts of the calorimeter.

2.2.2 Central tracking chamber

The CTC is the primary system for observing the tracks of individual charged particles [78]. It is a cylindrical drift chamber [79] 3.2 m in length (including endplates), occupying the volume at radii between 277 mm and 1380 mm from the beamline. The endplates and outer cylinder are aluminum and the inner cylinder is carbon-fibre reinforced plastic. The CTC contains 84 radial layers of sense wires grouped in nine superlayers, which alternate between axial alignment (parallel to the beamline) and stereo (canted at $\pm 3^\circ$ from the beamline). There are five axial layers and four stereo superlayers; the stereo angle alternates between $+3^\circ$ and -3° in successive stereo superlayers. Tracks with $|\eta|$ less than about 1.0 pass through all nine superlayers. Tracks at larger $|\eta|$, up to 2.0, can also be reconstructed using the inner superlayers, but the precision is not as good.

The superlayers are divided azimuthally into drift cells. The superlayers and their cells are shown in Figure 2.4. The axial cells contain twelve sense wires each and the stereo cells contain six each. Positioned about the sense wires are various HV field wires which provide the electric field and close off the cell. Their arrangement keeps the electric field uniform throughout the cell to within 1.5%. The sense wires are made of 40 μm gold plated tungsten, whereas the other wires are stainless steel of various gauges. The sense wires in a cell are arranged in a line at an angle of 45° to the radial direction[5]. This geometry ensures that any radial track will pass close to at least one sense wire per superlayer. It also causes the drift electrons to move in the azimuthal direction due to the Lorentz force of the magnetic field. This implies that the electrons move essentially orthogonally to the track, which simplifies drift time measurements. The high voltage on the field wires is set

[5] An illustration of this is available in Figure 3.3.

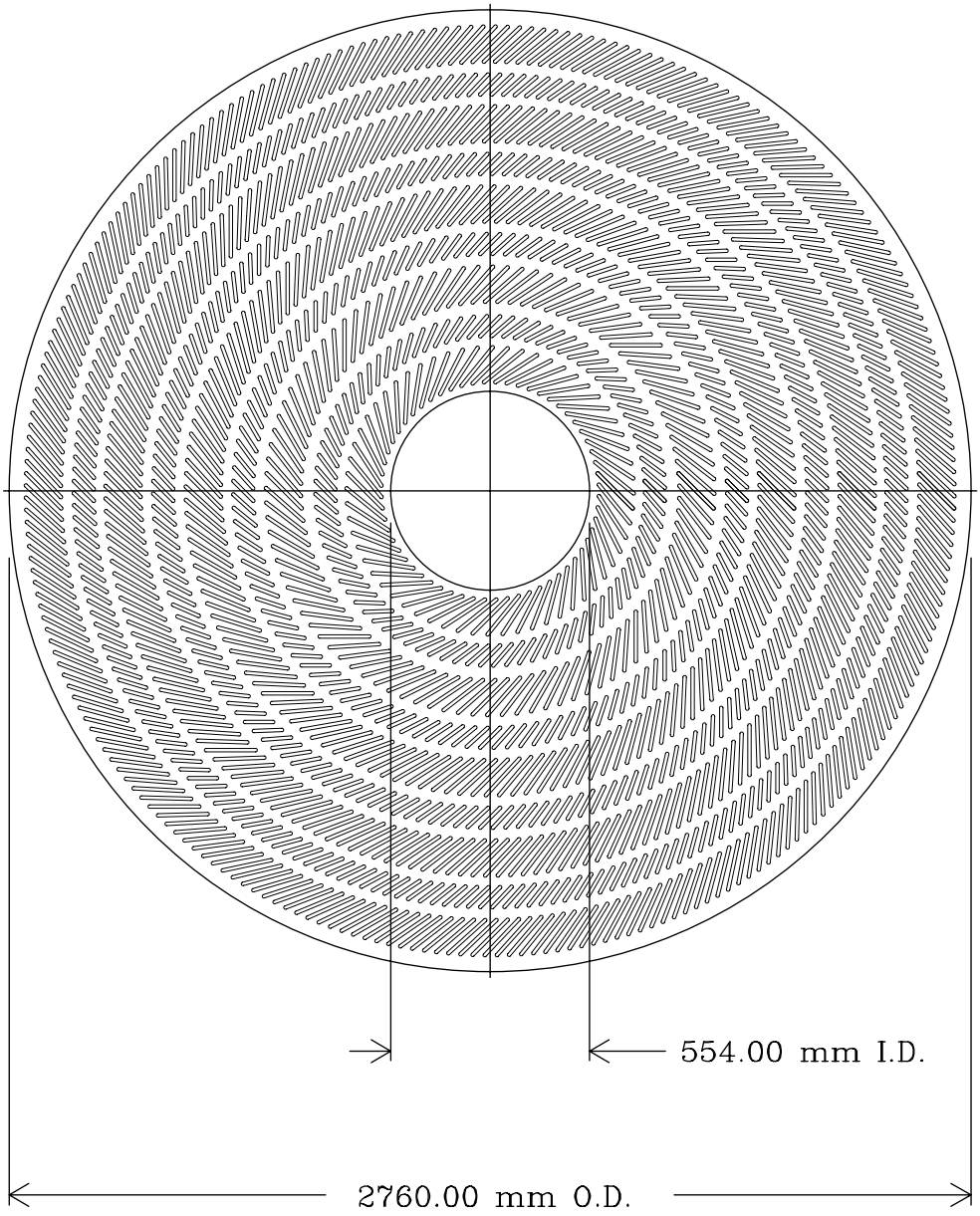


Figure 2.4: A CTC endplate, showing the wire feedthrough slots for the cells in the nine superlayers. Each cell is tilted at 45° to the radial. From [78].

to give a drift field of about 1350 V/m, which saturates the electron drift velocity. The drift gas is an equal mixture of argon and ethane with a small amount ($\sim 0.8\%$) of ethanol. The maximum drift distance in a cell is ~ 40 mm corresponding to a maximum drift time of ~ 800 ns, well less than the bunch crossing time.

Each sense wire is attached to a preamplifier mounted on the CTC endplate. The preamplified analog signal is fed into an amplifier-shaper-discriminator circuit, which produces a differential ECL pulse with width equal to the signal's time over threshold. The pulse is then transmitted to time-to-digital converters (TDC's) in the counting room on the first floor of the B0 assembly building. The drift distance resolution has been measured to be between 170 μm (in the outer superlayers) and 220 μm (in the inner superlayers) [80]. The time-over-threshold also provides a measurement of the track's energy deposition, which is useful for particle species identification. The TDC's are designed to be able to read at least 8 hits per wire per event.

The CTC can efficiently reconstruct tracks with transverse momenta above 0.4 GeV/c (the efficiency is about 95% [81]). It also provides information used in the Level 2 trigger, which is discussed further in Section 3.2.2. The stereo superlayers provide z measurements with a hit resolution of about 4 mm. Together the axial and stereo layers provide three dimensional track reconstruction, with a momentum resolution better than $0.002 \cdot P_T$ (P_T in GeV/c) for central tracks [75]. The resolution for discerning two tracks close together is approximately 5 mm. Figure 2.5 is a picture generated by the CDF event display software, which shows the reconstructed CTC tracks in a typical event.

2.2.3 Silicon vertex detector

The silicon vertex detector (SVX) is the closest detector system to the beamline. It is a four-layer single-sided silicon microstrip detector [82] which provides high precision tracking information complementary to that of the CTC. Its primary purpose is to identify displaced decay vertices characteristic of long-lived charm and beauty hadrons. The SVX was the first silicon vertex detector to be operated at a hadron collider. There were two incarnations of the SVX: the original device [83, 84], used in 1992-93, and SVX′ [85, 86], used in 1994-

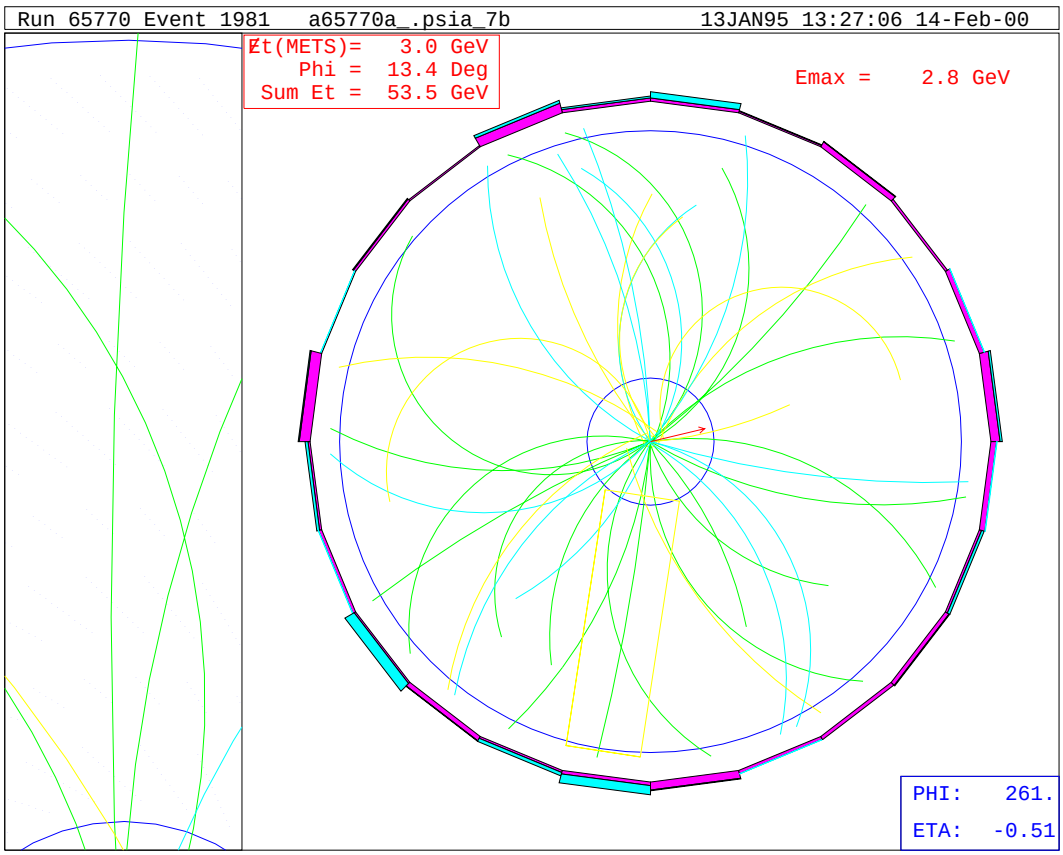


Figure 2.5: A typical $J/\psi \to \mu^+\mu^-$ candidate event reconstructed in the CTC, seen in the plane transverse to the beamline. The two muon candidates are identified by hits in muon chambers outside the calorimeters (not shown). The negative muon candidate is centred in the box; it has the highest P_T of all the tracks (3.8 GeV/c) and consequently the least curvature. Its reconstructed track is shown in the closeup at left with sense wires also visible. The positive muon candidate is the next stiffest track and can be seen about 60° clockwise of the negative muon. Histograms around the edge of the CTC represent energy deposits in the central calorimeter.

95. They are similar in design, but SVX′ has improved radiation hardness and some other changes which are listed below. Unless specified, SVX will be used to refer to both devices.

The Tevatron beampipe inside CDF is made of beryllium and has a radius of 1.91 cm. The SVX consists of four concentric layers of silicon sensors located at distances between 3.01 cm and 7.87 cm from the beamline. Each layer consists of twelve ladders, each subtending 30° in azimuth, hence the sensors are wider in the outer layers. The four ladders in a radial line are called a wedge, and the layers are numbered in increasing radius from 0 to 3. Ladders are described further below. They are mounted at each end onto beryllium bulkheads which form the ends of cylinders. The SVX consists of two such cylinders, or barrels, each 25.5 cm long, with a 2.2 cm gap in between. The Tevatron produces a distribution of $p\bar{p}$ interactions that in the z direction is approximately Gaussian in shape with $\sigma \simeq 30$ cm. This implies that about 60% of primary vertices are contained in the fiducial volume of the SVX. Figure 2.6 shows a view of one barrel. Layer 3 extends to $|\eta| = 1.9$. Each ladder is tilted at 3° to provide some overlap between adjacent wedges. However, in Layer 0 of SVX there was no overlap, causing a small ϕ gap in coverage; this was corrected in SVX′ by moving the layer in to $r = 2.86$ cm and tilting it an extra 1.5°.

A ladder is the basic mechanical and electrical unit of the SVX. It consists of three sensors wirebonded end to end, with the associated mechanical supports and readout electronics. Each sensor is 8.5 cm long and contains aluminum readout strips running parallel to the beamline, thus making measurements in the $r - \phi$ coordinate only. The strip pitch is 60 μm for the first three layers and 55 μm for layer 3. SVX sensors were 300 μm thick DC-coupled single-sided sensors of n-type bulk with p^+ implants. SVX′ took advantage of then-mature AC-coupled sensor technology for improved radiation hardness, using 300 μm thick sensors [6] with a FOXFET biasing scheme [87]. The sensors are supported on a Rohacell foam backing reinforced with carbon fibre strips. The readout strips are wirebonded to readout chips located at the $|z| \simeq 25$ cm end of the ladder. The readout chips are mounted on an aluminum-nitride-substrate hybrid circuit called the ear board, which routes power and signals between the ladder and the outside world through a Kapton pigtail

[6] Both generations of sensors were manufactured by Micron Semiconductor Ltd., Lancing, Sussex, U.K.

cable. Layers 0-3 have 2, 3, 4 and 6 readout chips respectively. Figure 2.7 shows the layout of a ladder.

The readout chip is a custom designed 128-channel CMOS devices called the SVX IC [88]. The chips used in SVX had a 3 μm feature size, whereas the chips in SVX$'$ were 1.2 μm and were fabricated using a radiation-hard process. The SVX IC is a mixed analog-digital device, with analog preamplifiers, sample-and-hold and threshold storage sections, and digital data sparsification and serial readout. There are a total of 46,080 readout channels in the SVX. The total heat generated by the chips is about 100 W and is removed using chilled-water tubes and gas flow.

The SVX data acquisition system starts with the SVX IC's, which are connected to port cards mounted on the outer rim of the bulkheads. Each port card reads out one wedge and is in turn connected to Digitizer modules located in the collision hall. The 24 Digitizers are located in 4 crates, with one Controller module per crate. Each Controller module provides is interfaced to a FASTBUS Sequencer module in the counting room and hence to the Scanner Processors[7]. The Sequencers are in phase with the Tevatron master clock and generate the control line signals for the SVX chips. The chips go through a cycle of integrating charge over each beam crossing and storing the result on a sample-and-hold capacitor. When a Level 1 Trigger Accept is received, this acquisition stops. In the case of SVX (but not SVX$'$) the chips perform a second charge integration outside the beam crossing window, to measure the DC leakage current for subtraction[8]. If a Level 2 Accept is subsequently received, the detector is read out. Only channels above a programmed charge threshold, and their nearest neighbours, are read out. The strip signals are digitized by 12 bit ADC's in the Digitizers.

Radiation damage to the silicon due to incident tracks and beam conditions is a serious concern. The radiation dose is monitored by a system of thermoluminescent dosimeters and silicon diodes, as well as by tracking the detector's gain and noise performance over time.

[7] The CDF DAQ system is described below in Section 2.2.8.

[8] This process of subtracting the leakage current by taking a second charge integration is called quadruple-correlated sampling. SVX$'$ is an AC-coupled device so the second integration is not required; this case is called double-correlated sampling.

Radiation damage was the primary reason for the replacement of SVX with the "radiation hard" SVX′. By the end of Run 1A the inner layer had received about 15 krad and the deterioration in performance was evident. DC-coupled sensors are particularly sensitive to the increase in DC leakage current caused by irradiation: it may saturate the preamplifiers. AC-coupled sensors display improved radiation hardness because they do not subject the preamplifiers to the leakage current.

Since the SVX is a high precision tracking device, its alignment is crucial. Optical surveys were performed during barrel assembly and mounting in the VTX and then in the CTC. Further alignment corrections are made to SVX data offline using tracking measurements. SVX data is also used to measure the position of the beamline on a run-by-run basis. In general, the SVX is not a standalone tracking device: SVX data is combined with tracks reconstructed in the CTC to improve their impact parameter and momentum resolution. Individual SVX strips with signals are first grouped into clusters of one, two or more strips. The cluster position resolution depends on the number of strips but averages 13 μm over all clusters [86]. Clusters are then matched to CTC tracks which have been extrapolated into the region of the SVX. The combined SVX+CTC tracks have an impact parameter resolution of $(13 + 40/P_T)$ μm and a P_T resolution of $0.0009P_T \oplus 0.0066$ [76].

2.2.4 Vertex time projection chamber

Between the SVX and CTC there is a vertex time projection chamber (VTX) [89], which is used to identify the position of $p\bar{p}$ collision vertices along the beamline. At the luminosities encountered during Run 1, one event may contain several $p\bar{p}$ collisions. The VTX replaced an older time projection chamber (the VTPC [90]) in 1992. It is similar in design, but consists of 28 modules along the beamline rather than 8. Each module consists of eight azimuthal octants, with arrays of sense wires and cathode pads at each end. The total length of the VTX is 287 cm, and it can provide standalone tracking to a maximum $|\eta|$ of 3.25. It provides z and $r-\phi$ information on charged tracks, as well as dE/dx measurements, out to a radius of 22 cm. In its primary role, the VTX uses the observed tracks to measure the z position of each primary vertex with a resolution of 1 mm. Information from the VTX

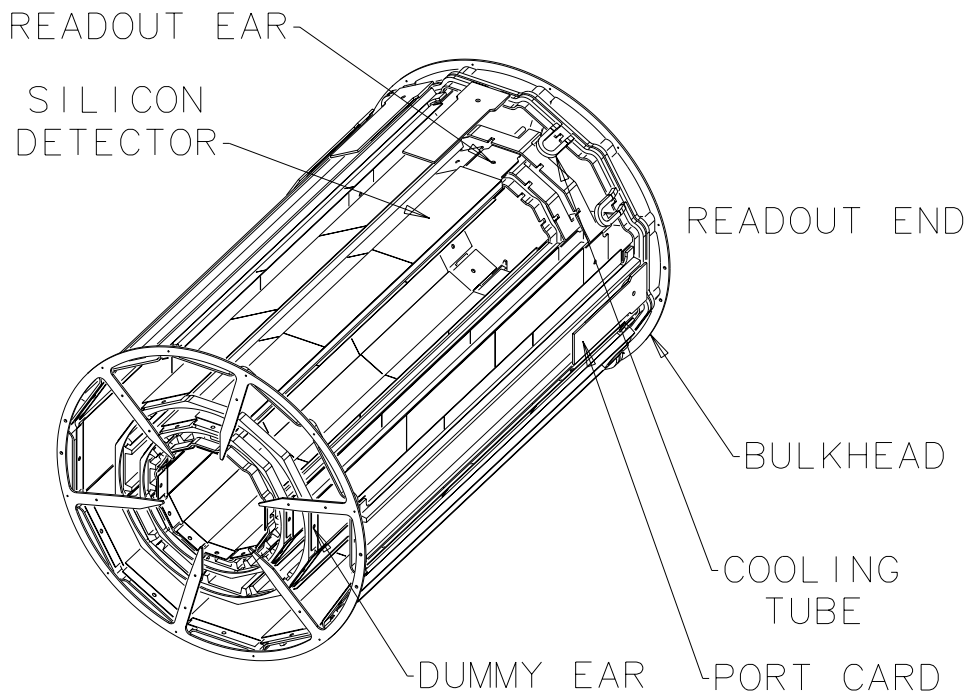


Figure 2.6: An SVX barrel. Two such barrels constitute the SVX detector; the readout ends are located furthest from the interaction point. The positions of the four layers and twelve wedges of ladders can be seen. From [86].

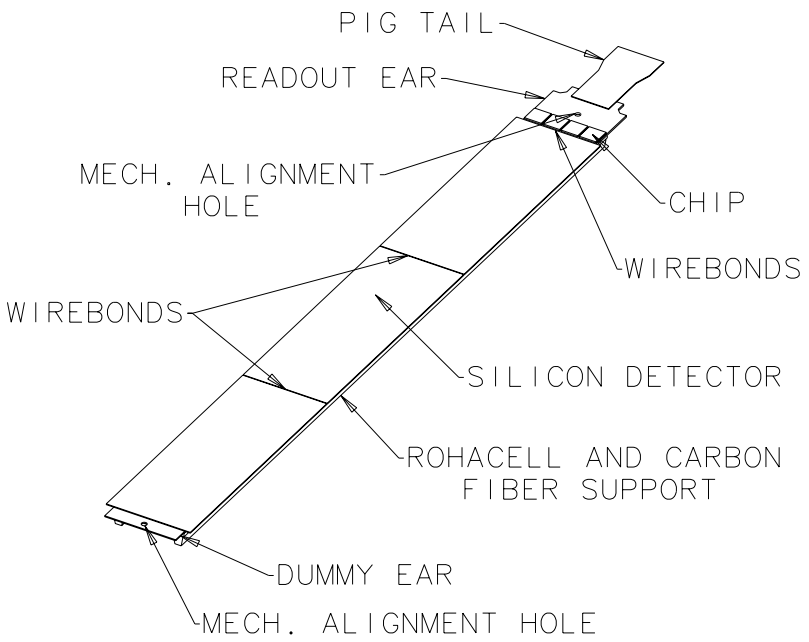


Figure 2.7: An SVX layer 2 ladder with 4 SVX IC chips. The three sensors are wirebonded together to form one electrical unit. The dummy ear is a mechanical piece which connects that end of the ladder to the bulkhead.

is used to help reconstruct tracks in the CTC.

Where possible, low mass materials such as foam and carbon fiber are used in the construction, so the VTX only comprises about 3% of a radiation length for central tracks. A schematic diagram of two octants of the VTX is shown in Figure 2.8.

2.2.5 Calorimeters

The CDF calorimeter system is designed to measure the energies of particles and jets by fully absorbing all particles, except muons and neutrinos. The calorimeters are exterior to the tracking systems and solenoid, and provide contiguous coverage out to $|\eta| = 4.2$, i.e. between 2° and 178° in polar angle. They are divided longitudinally into electromagnetic (EM) and hadronic calorimeters. The EM compartment is closer to the beam, and contains and measures electromagnetic showers caused by photons and electrons. The hadronic compartment comprises the bulk of the calorimeter, since the hadronic showers it measures require more material to contain than do EM showers.

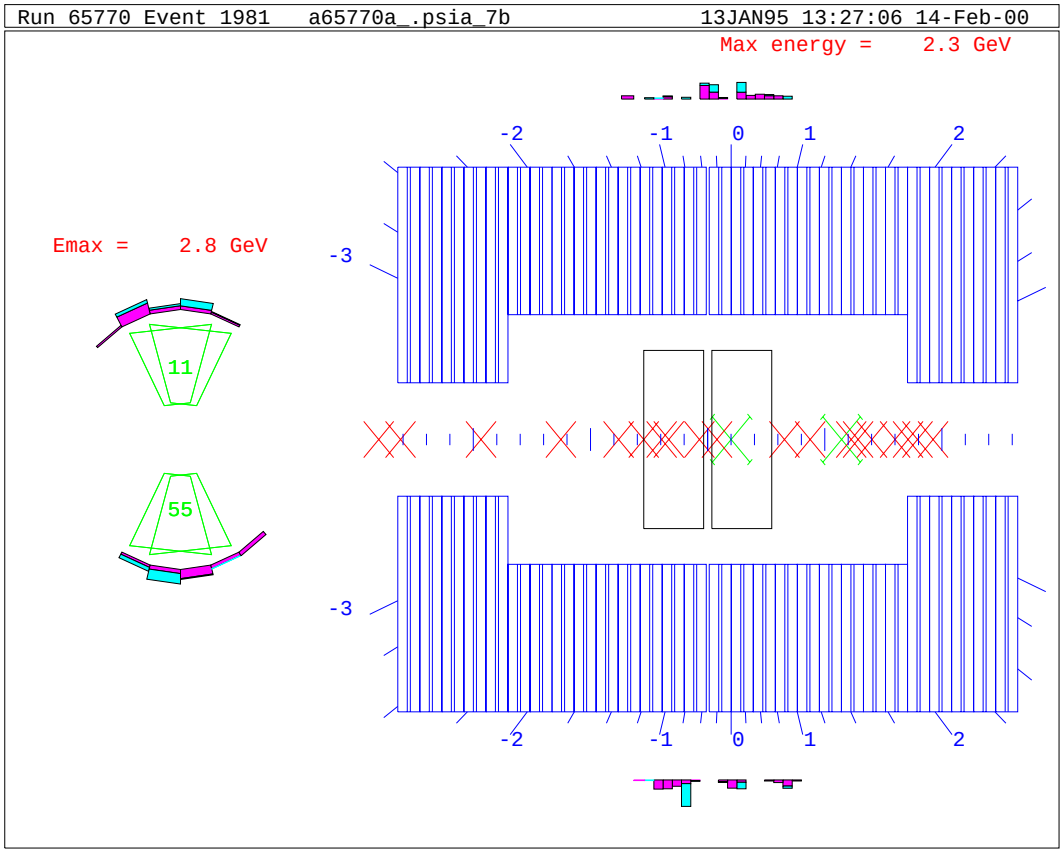


Figure 2.8: Side view of two opposite octants of the VTX, showing the two primary vertices in the event of Figure 2.5. The two genuine $p\bar{p}$ collision vertices are identified by larger lighter crosses; the smaller darker crosses are poorly reconstructed vertices which are essentially noise. The genuine vertices are at $z = 10.0$ cm and $z = 57.2$ cm. The J/ψ candidate originates at the former vertex and both muons have been reconstructed in the SVX. The two boxes in the centre show the location of the SVX. Outer histograms represent energy deposits in the central calorimeter. Hits and track segments in the VTX are not shown. Note that the vertical and horizontal axes are not drawn on the same scale.

Table 2.1: Selected characteristics of the various calorimeters. Total thickness is quoted in radiation lengths for EM calorimeters and nuclear interaction lengths for hadronic calorimeters.

Calorimeter:	Central EM	Central Hadron	Endwall Hadron	Plug EM	Plug Hadron	Forward EM	Forward Hadron
$\|\eta\|$ coverage	0-1.1	0-0.9	0.7-1.3	1.1-2.4	1.3-2.4	2.2-4.2	2.3-4.2
Tower size, $\Delta\eta \times \Delta\phi$	$0.1 \times 15^\circ$	$0.1 \times 15^\circ$	$0.1 \times 15^\circ$	$0.09 \times 5^\circ$	$0.09 \times 5^\circ$	$0.1 \times 5^\circ$	$0.1 \times 5^\circ$
Absorber, thickness	Pb 3.2 mm	Fe 25 mm	Fe 51 mm	Pb 2.7 mm	Fe 51 mm	Pb/Sb 4.8 mm	Fe 51 mm
Number of layers	31	32	15	34	20	30	27
Total thickness	18 X_0	4.5 λ_I	4.5 λ_I	19 X_0	5.7 λ_I	25 X_0	7.7 λ_I
σ_E/E at 50 GeV	2%	11%	14%	4%	20%	4%	20%

There are several distinct calorimeter systems in CDF, covering different ranges of pseudorapidity. In order of increasing $|\eta|$, they are called central, end wall, end plug and forward. All are sampling calorimeters [91]. The active medium of the central and endwall calorimeters is scintillator, whereas the plug and forward calorimeters use proportional tubes. The absorber is lead in the EM compartment and iron in the hadronic. To match the expected energy distribution in hadron collisions, each calorimeter is segmented into towers of equal size in pseudorapidity and ϕ. The segmentation is fine enough that one jet will spread over several towers. Table 2.1 summarizes some properties of the calorimeter systems. References [92, 93, 94, 95, 96] describe their design and construction in detail.

The central+endwall calorimeter contains two halves, referred to as east ($z > 0$) and west ($z < 0$). Each half contains with 24 wedges in ϕ and $\sim$ 10 towers in η. A wedge is shown in Figure 2.9. The central EM calorimeter includes a set of strip chambers (the CES) embedded at a depth of 5.9 radiation lengths (this number includes the coil). The CES measures the position of EM showers in the z and $r - \phi$ directions, and is located at the depth corresponding to the maximum shower development. A similar set of chambers, called the central preshower detector, is located between the solenoid and the beginning of the EM calorimeter, but provides $r - \phi$ measurements only.

2.2.6 Muon detectors

Muon detection is performed by a set of drift chambers outside the calorimeters. The calorimeters provide the necessary shielding, absorbing most of the charged hadrons which would otherwise be background in the muon chambers. CDF possesses several muon systems. The central muon system covers the pseudorapidity range $|\eta| \leq 1.0$, while the forward muon system covers $2.0 \leq |\eta| \leq 3.6$. Each half of the forward muon system [97] consists of two magnetized iron toroids instrumented with planes of drift chambers and scintillators.

The central muon system itself consists of three detectors: the original Central Muon chambers (CMU), the Central Muon Upgrade (CMP) and the Central Muon Extension (CMX). The CMU [98] is located at the outside of the central calorimeter and extends to $|\eta| \simeq 0.6$. The central calorimeter provides 4.9 interaction lengths of material (at $\eta = 0$) to

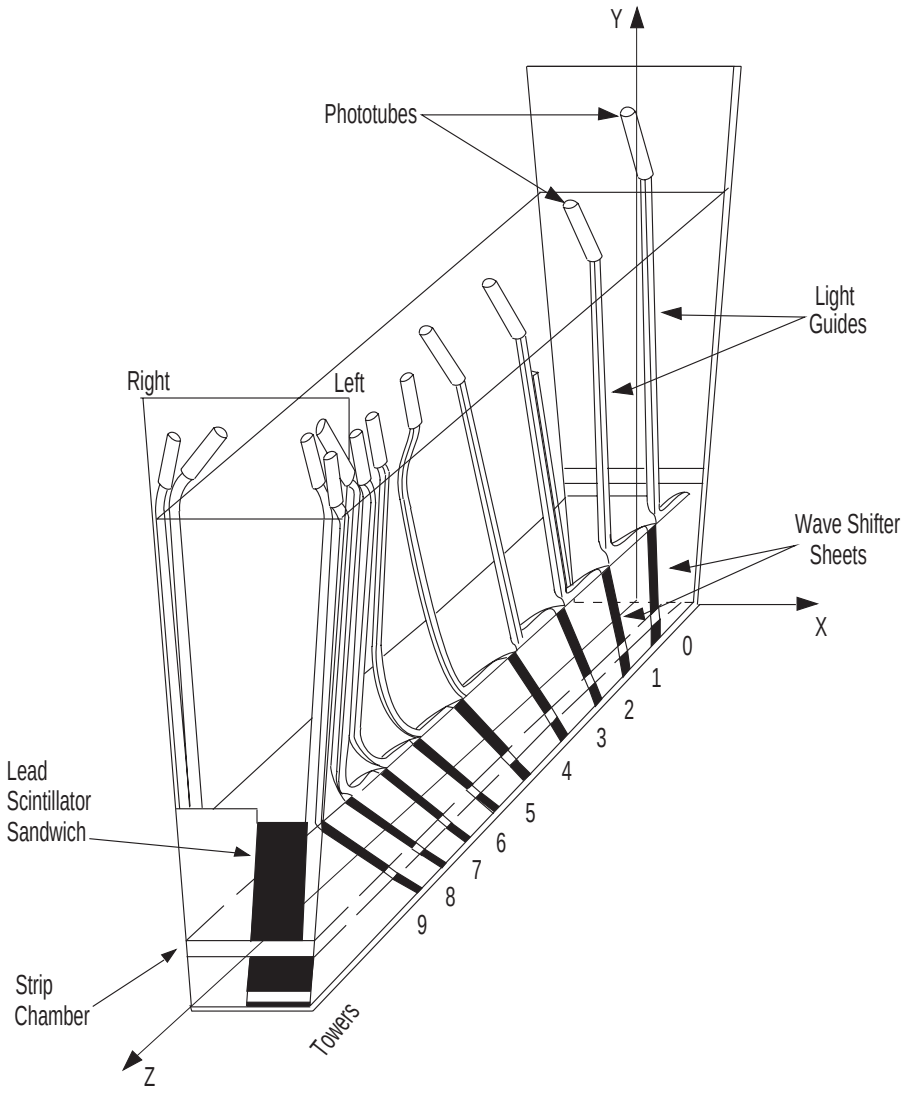


Figure 2.9: One wedge of the central calorimeter, showing the ten towers in η. A wedge subtends 15° in azimuth. The EM compartment is the lower portion and includes the strip chamber; the rest is the hadronic compartment. The endwall calorimeter, which completes the central hadronic coverage, is not shown. From [92].

filter out hadrons. The CMP and CMX were added in 1992 [99]. The CMP covers the same region as the CMU but is located behind an additional ~ 2.4 interaction lengths of steel shielding. The CMP thus provides a higher signal purity, although not all CMU muons have sufficient energy to reach the CMP. The CMX extends the $|\eta|$ coverage out to ~ 1.0. Muons reaching the CMX traverse an average of 6.2 interaction lengths. Figure 2.10 shows the coverage of the central muon systems.

The basic setup of all the central muon systems is similar: they consist of several layers of single-wire drift cells, with the wires oriented parallel to the beamline[9]. The CMX and CMP also include scintillator planes, called CSX and CSP, mounted on their inner and outer surfaces. The scintillators provide precise timing measurements used in the trigger; for the CMU this function is performed by the TDC's of the central hadron calorimeter. For details of the muon chambers it will suffice to describe the CMU.

The CMU cells are located in the top of the central calorimeter wedges, as shown in Figure 2.11, at a radius of 347 cm from the beamline. There are three adjacent modules per 15° wedge. Each module subtends 4.2° so there are small gaps in ϕ coverage between wedges. Each module consists of a four by four array of drift cells, shown in Figure 2.12. Aluminum sheets held at ground form the top and bottom of each cell. The sides of the cells are aluminum I-beams or C-beams, held at -2500 V and insulated from the sheets by G-10 spacers (see Figure 2.13). At the centre of the cell is a 50 μm stainless steel sense wire held at 3150 V. The drift gas is an even mixture of argon and ethane with $\sim 1\%$ ethanol. The maximum drift time is on the order of 700 ns.

The cells are not all the same width, rather, they are arranged so that the sense wires of two alternating layers lie on a radial line from the centre of the detector (see Figure 2.12). The other two sense wires are displaced from this line by 2 mm to resolve whether tracks pass to the left or to the right. The Level 1 muon trigger, described in Section 3.2.1, makes use of this geometry. Alternating cells in ϕ, meanwhile, use the same sense wire, which is connected at the $\eta = 0$ end of the cell. The sense wires are read out through a blocking

[9]The CMX wires are actually at an angle to the beamline, but they are still oriented to measure the $r\phi$ coordinate.

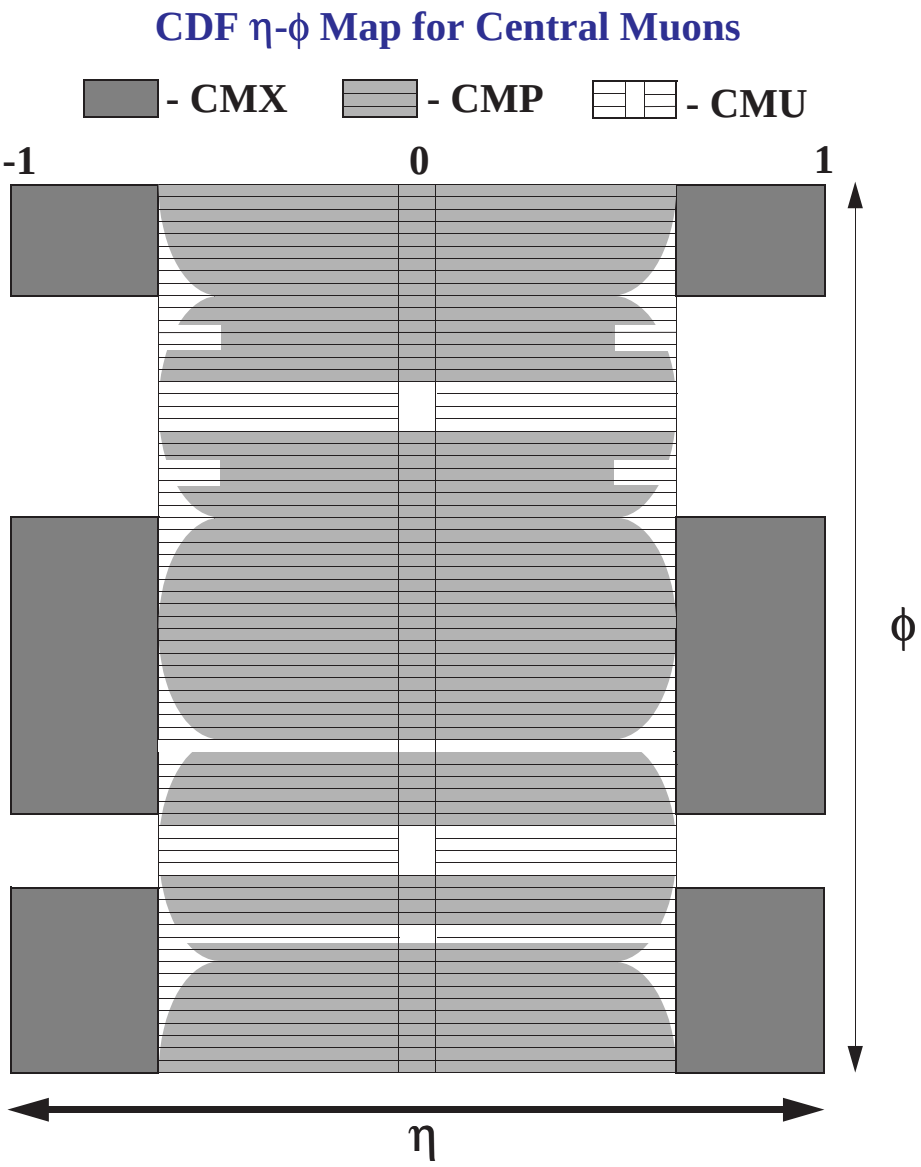


Figure 2.10: Central muon coverage in pseudorapidity and azimuth. The gaps in CMX ϕ coverage are due to the Main Ring and the floor of the collision hall. The CMU has a 6 cm long gap between the east and west halves, which is not drawn to scale. The CMU also has gaps in ϕ between wedges which are too small to be illustrated here. From [99].

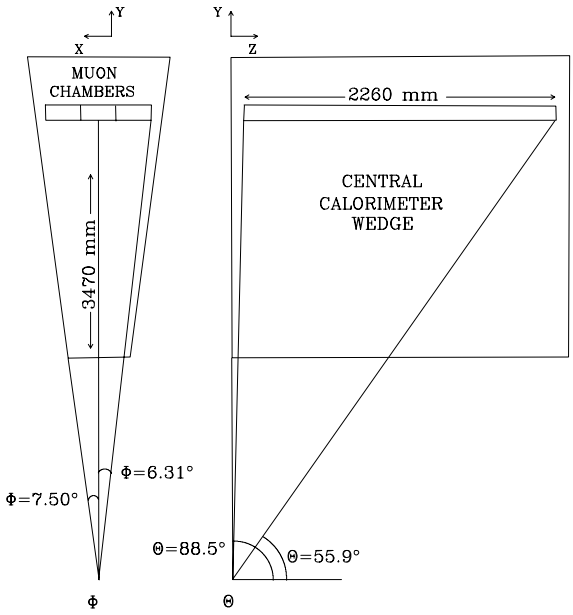


Figure 2.11: Location of the central muon chambers. Each of the three modules shown contains 16 drift cells. From [98].

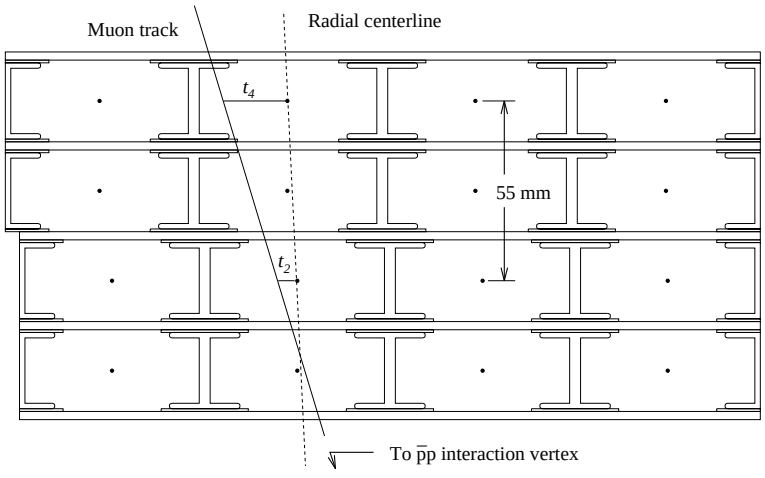


Figure 2.12: A central muon module, consisting of four layers of four cells. A group of cells two wide and four deep is called a tower, hence a module consists of two towers. A muon track at angle α to the radial is shown, with two measured drift times (t_2 and t_4) shown. These times measure α and are used in the Level 1 muon trigger. From [100].

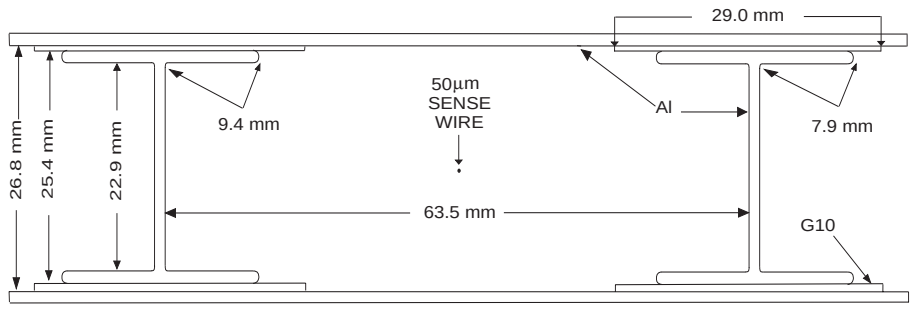


Figure 2.13: A CMU cell, showing the aluminum sheets and I-beams, G-10 spacers and the steel sense wire. CMU cells come in different widths. From [98].

capacitor at the $|\eta| = 0.6$ end of each cell. RABBIT muon TDC-ADC cards use charge division to measure z, and drift times to measure $r - \phi$. The z measurement resolution is 1.2 mm and the azimuthal resolution is 250 μm.

2.2.7 Beam-beam counters

The beam-beam counters (BBC's) [75] consist of two planes of scintillator counters, mounted on the front wall of the forward calorimeters 5.8 m from the interaction point. They cover the region $3.2 \leq |\eta| \leq 5.9$ with a timing precision better than 200 ps. The BBC's are used to measure the beam luminosity received at CDF[63]; the BBC cross section is $\sigma_{BBC} = 51.15 \pm 1.60$ mb [101]. They are also used in triggering: BBC hits can be required in Level 1 triggers, and an east/west BBC coincidence in time with the bunch crossing provides a minimum-bias trigger.

2.2.8 Data acquisition and trigger system

The data acquisition (DAQ) system is responsible for extracting the information recorded by each detector subsystem and combining the channel-by-channel data into a coherent record of each event. A vital part of this system is the trigger system, which selects those events that are sufficiently interesting to be recorded. Due to the large $p\bar{p}$ cross section, most bunch crossings during Run 1 contain at least one $p\bar{p}$ interaction, so interactions are occuring at a rate of ~ 280 kHz. However, the maximum reasonable rate at which events

can be written to mass storage on tape is less than 10 Hz. A three level trigger system uses event data as it is being recorded to effect the necessary data reduction. The subsequent levels perform increasingly detailed analysis of detector information, only accepting events of potential interest for analysis. The first, second and third level triggers typically accept events at a rate of about 1 in 600, 1 in 100, and 1 in 4 respectively [80].

The data acquisition system [102] evolved considerably before and during Run 1, therefore this section will only describe the overall setup, leaving out details of the electronic hardware. The "front end" electronics are the first stage of the DAQ after the detector components, and consist of crate-based modules. FASTBUS modules are used for the tracking chambers, and RABBIT [103] modules are used for the calorimeters, central muon systems and SVX. The RABBIT crates are located in the collision hall. These modules perform basic functions such as signal amplification analog-to-digital conversion, time-to-digital conversion, pedestal subtraction and threshold comparison. Detector signals are stored at the front end while the Level 1 and Level 2 trigger decisions are made.

Level 1 trigger

The Level 1 trigger system [104] is a hardware trigger implemented in FASTBUS crates in the counting room. It receives fast output analog signals from the calorimeters and central muon systems, on dedicated cables separate from the general DAQ. The Level 1 trigger makes its decision before the next bunch crossing occurs and thus incurs no deadtime. Calorimeter signals are summed into "trigger towers" which cover 0.2 units of η and 15° in ϕ. Muon towers with hits are identified (the Level 1 dimuon trigger is described in detail in Section 3.2.1). The hardware checks whether any calorimeter or muon trigger towers contain signals above preset thresholds. If the event passes, further event acquisition stops and the event is processed by the Level 2 trigger. The details of the Level 1 requirements are programmable and are maintained in a "trigger table". The trigger table also contains instructions for the Level 2 and 3 triggers, and may be altered as necessary. At an instantaneous luminosity of 5×10^{30} cm^{-2}s^{-1}, the typical Level 1 acceptance rate is 1 kHz [76].

Level 2 trigger

The Level 2 trigger is also a FASTBUS based hardware trigger, and makes use of the same information as the Level 1 trigger, as well as CTC information. It takes 20 μs to analyze an event; the bunch crossings that occur during this time are lost. The Level 2 trigger searches for energy clusters in the calorimeter, does simple CTC track reconstruction (see Section 3.2.2 for details) and can match tracks to calorimeter or muon clusters. Further selection requirements are applied to these clusters. The typical acceptance rate at $\mathcal{L} = 5 \times 10^{30}$ $\mathrm{cm}^{-2}\mathrm{s}^{-1}$ is 12 Hz.

Event readout and Level 3 trigger

The Level 1 and Level 2 triggers report their acceptance or rejection of the event to a FASTBUS module called the Trigger Supervisor (TS). The TS in turn communicates to a set of processing units called scanners. When a Level 2 Accept occurs, the scanners read out the digitized data from the front end electronics. At this stage the information from individual detector subsystems is still separate; the event fragments are next gathered together by an Event Builder system and passed to the Level 3 trigger.

The Level 3 trigger [105] is a farm of CPU's connected on a local area network. Each CPU runs software algorithms on an event to reconstruct physics objects such as tracks, jets and lepton candidates in three dimensions. This analysis is coded in Fortran and is as similar as possible to the offline event reconstruction software. A full event reconstruction allows several further criteria to be applied. It is possible for the Level 3 trigger to impose a wide variety of requirements for passing events. If the event passes Level 3, it is allocated to a separate process (the Data Logger) to be recorded on 8-mm tape. The acceptance rate for Level 3 was about 5 Hz during Run 1A [76]. Once an event is stored on tape, it is possible to reprocess it to apply calibrations and corrections, and to analyze its contents offline.

Chapter 3

Data Sample and Event Selection

The experimental signature of the decay $J/\psi \to \mu^+\mu^-$ is simply two muons, each consisting of a hit in the muon chambers associated with a track in the CTC. Histograms of the $\mu^+\mu^-$ invariant mass in the region around 3.1 GeV/c^2 clearly show the J/ψ signal peak. The relative simplicity of observing the decay $J/\psi \to \mu^+\mu^-$ has long made it a standard detection channel in high energy physics experiments. This chapter provides an overview of the J/ψ data sample collected by CDF and used in this analysis. The Tevatron running period is described first, followed by the specific triggers used to collect dimuon events, then the offline selection criteria applied to events in the data sample.

3.1 Run 1 of the Tevatron

As mentioned previously, this analysis uses data recorded during Run 1 of the Tevatron. Run 1 consisted of several periods. Run 1A began in August of 1992 and ended in May 1993. The average instantaneous luminosity at CDF during Run 1A was 3.3×10^{30} cm^{-2}s^{-1}, and CDF recorded an integrated luminosity of 19.7$\pm$0.7 pb^{-1} [63]. Run 1B began in January 1994, after a shutdown which CDF used to replace SVX with SVX$'$ and to improve the DAQ system. Run 1B lasted until July 1995, with CDF recording 86.5$\pm$3.5 pb^{-1} of data. The instantaneous luminosity was significantly higher during Run 1B, averaging 9.1×10^{30} cm^{-2}s^{-1} and reaching up to 27×10^{30} cm^{-2}s^{-1}. Two more runs, Run 1C and a run at

$\sqrt{s} = 630$ GeV, lasted until February 1996 but are not included in this analysis. The CTC suffered a broken wire in Run 1C. This analysis uses the Run 1A and Run 1B data samples, which correspond to a total integrated luminosity of 106.1 ± 4.1 pb^{-1}.

3.2 Dimuon Triggers

The dimuon trigger is configured to record pairs of muons in the CMU and CMX detectors. Forward muon triggers also exist but are not used in this analysis. In order to maximize the acceptance for J/ψ decays, the dimuon trigger should accept muons with as low P_T as possible. This goal is limited by several factors. Firstly, because of ionization energy loss in the central calorimeter, only muons with $P_T \gtrsim 1.4$ GeV/c are capable of reaching the CMU. Secondly, only a limited fraction of the DAQ system's bandwidth can reasonably be devoted to dimuon events, so the trigger rate must be limited. Muon signals and backgrounds both increase significantly at low P_T. As a result, CDF dimuon triggers typically record muons with P_T down to about 2 GeV/c .

Single muon triggers also exist, but because of bandwidth these triggers can only be used for higher P_T muons, typically above 5 GeV/c . The single muon triggers require CMU hits to be confirmed by the CMP, to reduce backgrounds. These triggers are usually used to select events with single high P_T muons, such as semileptonic B decays or W decays. However, they also provide useful control samples for studying the efficiencies of the dimuon triggers.

3.2.1 Level 1

The first level muon trigger uses hits in the CMU and CMX drift chambers to identify muon candidates [100]. Figure 2.12 illustrates the passage of a charged particle through a CMU module (the CMX has more layers of cells but the trigger procedure is analogous). The difference in drift times between pairs of radially aligned wires (for example $|t_4 - t_2|$) measures the angle (α) between the track and the radial line from the centre of the detector. As shown in Figure 3.1, this angle provides a measurement of the transverse momentum

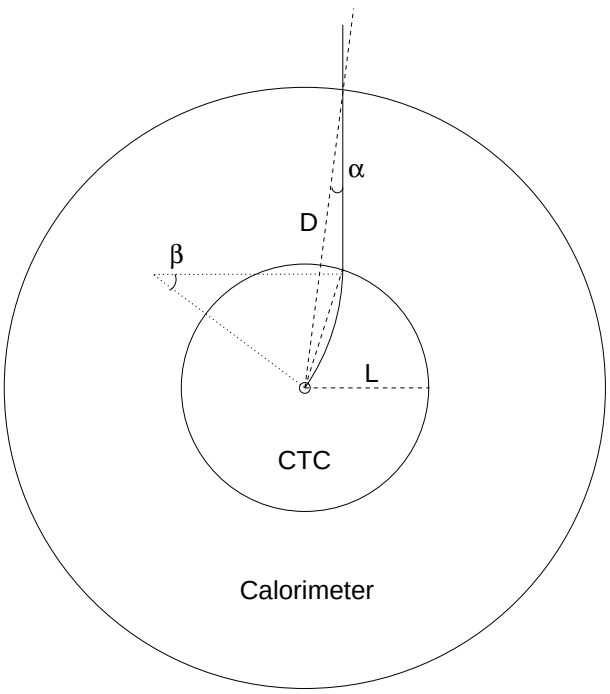


Figure 3.1: Transverse momentum measurement in the Level 1 muon trigger. The curved line represents the path of a charged particle deflected through angle β by the magnetic field B. This geometry allows the transverse momentum to be derived from α using $\sin(\alpha) = eL^2B/2DP_T$. Here $L = 1.44$ m and $D = 3.47$ m. Based on a figure in [98].

of the track; they are approximately inversely proportional. For each tower, the Level 1 trigger compares the drift time differences with a preset threshold to generate a decision. In effect this requires a minimum P_T for particles to fire the trigger[1], nominally 3.3 GeV/c . However, multiple scattering of the muon in the calorimeter smears α and so the trigger efficiency does not exhibit a sharp turn-on. The trigger efficiency is plotted in Figure 3.2.

Tracks in the muon towers are referred to as "stubs" to distinguish them from CTC tracks. To reduce background, the muon trigger requires that CMX stubs are confirmed by CSX scintillator hits in time with the beam crossing [106]. In Run 1B this function was performed for the CMU by the TDC's of the central hadron calorimeter. A hadron TDC coincidence was also required of CMX stubs to reject background from particles originating

[1]There are two thresholds, at 3.3 GeV/c and at 6 GeV/c . The dimuon trigger uses the lower one.

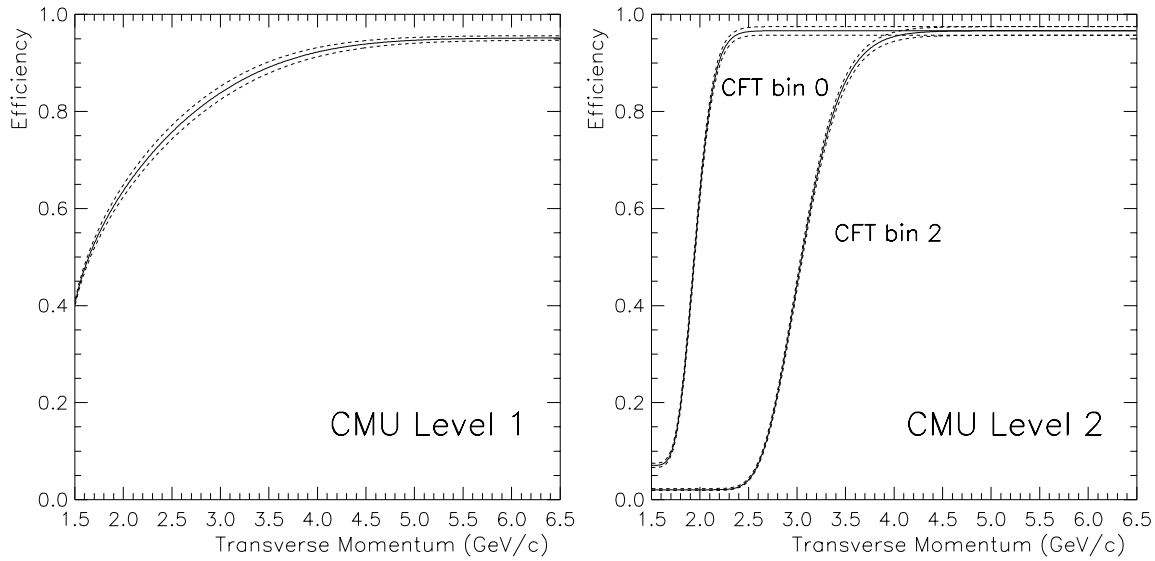


Figure 3.2: Level 1 and 2 muon trigger efficiencies in the CMU as functions of P_T. The first plot shows the measured efficiency for a muon to pass the Level 1 low-P_T trigger. The dotted lines show the 1σ variations in the fitted parameterization. The efficiency presented is for Run 1B but is not significantly different in Run 1A. The second plot shows typical Run 1B efficiencies for muons to be found at Level 2 in CFT bin 0 or higher, and bin 2 or higher, again with 1σ variations in the fitted parameterization. From the analysis in [106].

outside the central detector [107].

The muon trigger merges pairs of towers into "trigger towers" which subtend 5° in azimuth [107] (i.e. a trigger tower is equivalent to a CMU module). The first level dimuon trigger requires the presence of two stubs in non-contiguous trigger towers. The trigger treats the east and west halves of the detector separately, and also for the CMU and CMX. Level 1 dimuon triggers are thus possible with two CMU stubs, two CMX stubs, or one of each. Lastly, the Level 1 trigger also requires signals in the BBC, to ensure that a genuine beam crossing has occurred.

3.2.2 Level 2

At Level 2, the Central Fast Track (CFT) trigger processor [108] reconstructs tracks in the CTC with $P_T \gtrsim 2$ GeV/c . The second level dimuon trigger operates by matching CFT

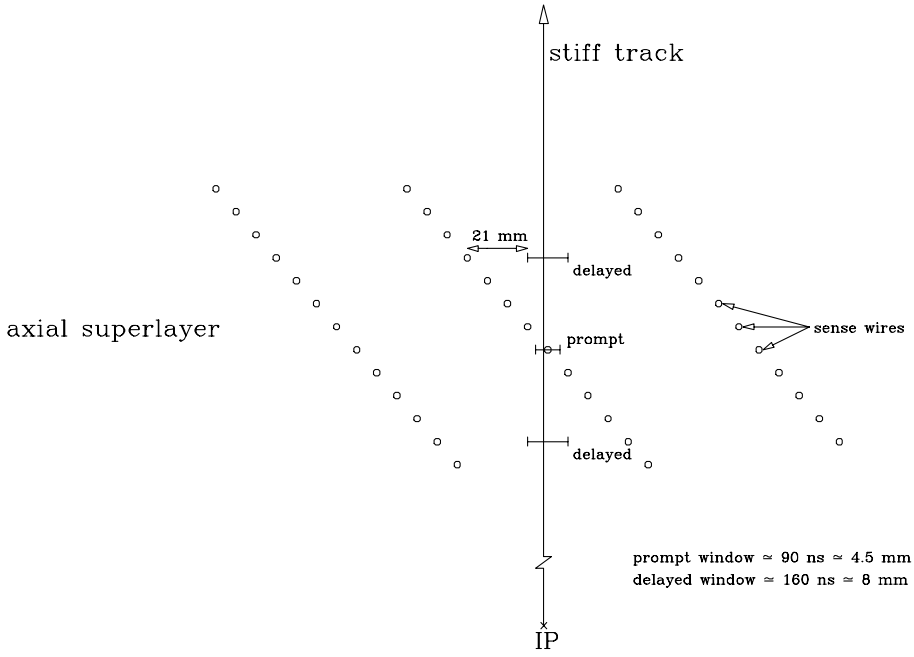


Figure 3.3: A high P_T track passing through an axial superlayer of the CTC. Only the sense wires are shown. The CFT processor uses the prompt and delayed hits from each axial superlayer to reconstruct the track and measure its momentum. From [109].

tracks to muon towers which triggered at Level 1.

The CFT uses $r - \phi$ information from the axial superlayers of the CTC only. A track which traverses all layers of the CTC must pass close to one sense wire in each axial superlayer, as illustrated in Figure 3.3. This results in a "prompt" hit recorded within a ~ 90 ns window after the beam crossing by the CTC TDC's [109]. A later time window at $\sim 530 - 690$ ns is defined for two subsequent "delayed" hits. The CFT processor starts by searching for cells with prompt and delayed hits in the outermost superlayer, then moves inward, finding matching hits on inner layers and adding them to track candidates. Typically, at least 14 of a maximum possible 15 hits are required for a track to pass the CFT. The CFT uses the curvature of reconstructed tracks to assign them to 8 P_T bins, with a P_T resolution is $\sim 3.5\%$. The 90% efficiency thresholds for the bins relevant to this analysis are 3.0 GeV/c for bin 0 (the lowest bin) in Run 1A, 2.2 GeV/c for bin 0 in Run 1B and 3.4 GeV/c for bin 2 in Run 1B.

Each CFT track is next extrapolated to the muon chambers using a lookup table. If the track matches a muon trigger tower which fired at Level 1, it is recorded as a muon candidate. The azimuthal matching requirement was originally $\Delta\phi < 15^\circ$ but this was reduced to $\Delta\phi \lesssim 5^\circ$ early in Run 1B. Areas of the calorimeter which contain muon candidates are marked as "muon clusters". The Level 2 trigger logic operates on clusters rather than individual muon stubs. The muon clusters are one wedge wide in azimuth, and three (two) calorimeter trigger towers[2] long in η for CMU (CMX) muons. Adjacent clusters are merged to form five-tower clusters, in the case of a CMU and a CMX cluster, or six-tower clusters, in the case of two CMU clusters. Typical efficiencies for individual muons at Level 2 are shown in Figure 3.2; they depend on P_T because of the efficiency turn-on of each CFT P_T bin.

The Level 2 trigger logic then considers pairs of muon clusters. There are a total of four specific Level 2 triggers relevant to this analysis, one from Run 1A and three from Run 1B (the Level 2 dimuon trigger changed substantially between runs). Each has a prerequisite in the Level 1 dimuon trigger. They are [106]:

- TWO_CMU_ONE_CFT_3: from Run 1A. Requires one CMU cluster, with an associated CFT track in any P_T bin, and a second Level 1 CMU stub.

- TWO_CMU_TWO_CFT_2_2: from Run 1B. Requires two CMU clusters each with an associated CFT track in any P_T bin. Due to cluster merging, the clusters cannot be adjacent.

- TWO_CMU_CMX_ONE_CFT_3_4: from Run 1B. Requires one CMU cluster with an associated CFT track in P_T bin 2 or higher, and a second Level 1 stub in either CMU or CMX.

- TWO_CMU_ONE_CFT_2_2_6TOW: from Run 1B. Requires one CMU cluster with an associated CFT track in any P_T bin; the highest P_T muon cluster must have six or more towers. This trigger is used to record muon pairs which are close in azimuth and thus fail TWO_CMU_TWO_CFT_2_2.

[2] A calorimeter trigger tower is two adjacent central calorimeter towers and covers 0.2 units in η.

3.2.3 Level 3

The third level dimuon trigger makes use of three-dimensional CTC tracking information. In Run 1A, the trigger relevant to this analysis required two muon candidates with opposite charge and invariant mass between 2.8 and 3.4 GeV/c^2 [81]. In Run 1B the relevant trigger required an invariant mass between 2.7 and 4.1 GeV/c^2 , but not opposite charge. The Level 3 trigger also performs more precise matching between the CTC track and the muon stub. The track is extrapolated to the position of the muon chambers and required to match the stub position in both the ϕ and z directions. The match was required to be within $\sim 4\sigma$ ($\sim 3\sigma$) during Run 1A (1B), taking the uncertainty due to multiple scattering and position measurement into account.

3.3 Data Storage

After being written to tape by the data acquisition system, events are processed again. In this step, run-dependent calibration and alignment corrections are made, and more sophisticated track reconstruction takes place. Since this takes place "offline", time is not a major constraint for the processing. An example of a correction would be one for the relative alignment of the SVX and CTC. Minor differences in the geometry of the detector between Run 1A and Run 1B are also taken into account. Events are also sorted into physics categories; dimuon events are thus separated from the rest of CDF's data and directed into a specific dimuon sample for storage. Events are stored in the YBOS format [110], in which selected physics objects in each event are stored sequentially in indexed banks. The bank for an object contains information about the object as reconstructed by offline analysis software. Examples of objects in YBOS banks used in this analysis are muon candidates, CTC tracks (with SVX information included if available), and records of which triggers fired.

The dimuon data sample is frequently used by members of the CDF collaboration so it is also stored on hard disk. Each event in the sample contains about 13 kB of information on average, however not all the detector data for each event have been stored; to save space some banks have been dropped, for example forward calorimetry. The dimuon sample

contains about 970,000 events and occupies about 13 GB on disk.

3.4 Event Requirements

In selecting the data sample, the first step which is specific to this analysis is to select J/ψ candidates with appropriate characteristics. This selection is performed by software written specifically for the J/ψ polarization analysis. The software processes the dimuon data sample, searching for J/ψ candidates and applying selection criteria which are described in detail below. If an event contains a good J/ψ candidate, the software records all the necessary information in an HBOOK ntuple [111] for further analysis.

One important requirement is that only muons in the CMU are used: CMX muons are rejected. The trigger efficiency plays a major role in this analysis and so must be well understood. While the CMU is a cylindrically symmetric detector, the CMX is not: CMX muons pass through the solenoid return yoke, which has a box-like geometry. The amount of material and hence multiple scattering varies significantly with azimuth and pseudorapidity, and the effect of this on the CMX trigger efficiency is not fully understood. Only about a quarter of all J/ψ candidates in the dimuon data sample involve the CMX, so the loss of statistics is not serious [112].

Data is processed in order of run number. The first set of requirements is applied to each run as a whole. If a run fails any of these requirements, no events in the run are included in the analysis. First, particular running periods with known problems are omitted: a period during Run 1A in which the bunch crossing time was not well measured due to a cable problem, and period during Run 1B when the CFT did not account for gravitational wire sagging [106]. Next, the status of the detector systems, as recorded in a run database, is checked. The trigger, tracking and calorimetry systems must be functioning normally. Specific checks are also made for the status of the CMU and the SVX. Next, the beam position is required to be well measured for the run. The beam positions have been measured on a run-by-run basis using SVX track information, and recorded in a database [113]. These requirements reduce the integrated luminosity available for analysis from 106

Table 3.1: Muon P_T requirements depend on the CFT bin used in the Level 2 trigger. A J/ψ candidate must satisfy at least one of the listed trigger/muon P_T requirements.

Level 2 dimuon trigger	Minimum P_T^{μ} (GeV/c)
TWO_CMU_ONE_CFT	one > 2.7, other > 1.7
TWO_CMU_TWO_CFT	both > 2.0
TWO_CMU_CMX_ONE_CFT_3_4	one > 2.9, other > 1.7
TWO_CMU_ONE_CFT_2_2_6TOW	both > 2.0

pb^{-1} to 101 pb^{-1}.

The next set of requirements is applied to each event and to the muon candidates in that event. The event is required to have passed at least one of the four Level 2 triggers listed in Section 3.2.2. Each muon candidate is required to be present in the CMU (candidates with hits in the CMP only or in the CMX only are rejected). The match between the CMU stub and the CTC track is required to have χ^2 less than 9 and 12 (for one degree of freedom) in the ϕ and z directions respectively. A few malfunctioning CMU towers had low efficiency over the course of Run 1A or Run 1B; muons in these towers are rejected.

J/ψ candidates are formed from all possible pairings of oppositely charged muon candidates in the event. To reject muons originating from different primary vertices, the measured z positions of the two tracks at the beamline are required to be within 5.0 cm of each other. Since there may be more than two muons in an event, it is verified that the two muons in the candidate J/ψ correspond to the towers which fired the trigger. This requirement also removes "volunteer" events which do not pass the second level dimuon trigger, but enter the sample by passing the third level dimuon trigger or a single-muon trigger. The muons must also satisfy minimum P_T requirements listed in Table 3.1. This ensures that the muon P_T is high enough that the second level trigger efficiency is well known.

The next step in the J/ψ reconstruction depends on whether the muons have been reconstructed in the CTC only (CTC muons) or in both the CTC and the SVX (SVX muons). Whether or not a muon has SVX information depends on its passing through the

active area of the SVX, on the SVX detection efficiency and on the reconstruction efficiency. SVX muons must have clusters matched to their track in at least three of the four layers of the SVX. If there are only two SVX clusters they are likely to be random coincidences. Muons with two clusters have poor impact parameter resolution so they are reclassified as CTC muons.

SVX-SVX and SVX-CTC muon pairs have their tracks refitted, with the constraint that the two muons originate at a common vertex. The SVX measures impact parameters well enough that significant displacements of this vertex from the beamline can be resolved. The constrained fit is performed by custom-written CDF software [114]. In the case of SVX-CTC pairs, the dimuon momentum is also constrained to point from the beamline to the vertex. This is necessary to compensate for the poorer impact resolution of the CTC muon. In both the SVX-SVX and SVX-CTC cases, the candidate is dropped if the fit χ^2 probability is less than 0.1%.

CTC-CTC pairs, on the other hand, do not have sufficient impact parameter resolution to provide useful vertex displacement information. Their tracks are simply refit with the constraint that they originate from the beamline. This constraint improves the dimuon mass resolution; after it is applied the CTC-CTC pairs have very similar mass resolution to the SVX-SVX and SVX-CTC pairs.

In the case of SVX-SVX and SVX-CTC muon pairs, the displacement of the dimuon decay vertex from the beamline can be expressed by the transverse decay length L_{xy}. Let $\vec{\Delta}$ be the two-dimensional vector pointing from the beamline to the fitted decay vertex. The position of the beamline is taken from the database mentioned above. Then the transverse decay length is the projection of $\vec{\Delta}$ onto the dimuon transverse momentum:

$$L_{xy} = \frac{\vec{\Delta} \bullet \vec{P}_T^{\mu\mu}}{P_T^{\mu\mu}} \tag{3.1}$$

This is illustrated in Figure 3.4. Prompt J/ψ mesons have Δ, and hence L_{xy}, consistent with zero, whereas those produced in B-hadron decays have positive L_{xy}. The uncertainty on L_{xy} is calculated using the uncertainty on the fitted decay vertex position and using a beam spot size of 25 μm. To ensure that L_{xy} is well measured, $\sigma_{L_{xy}}$ is required to be less

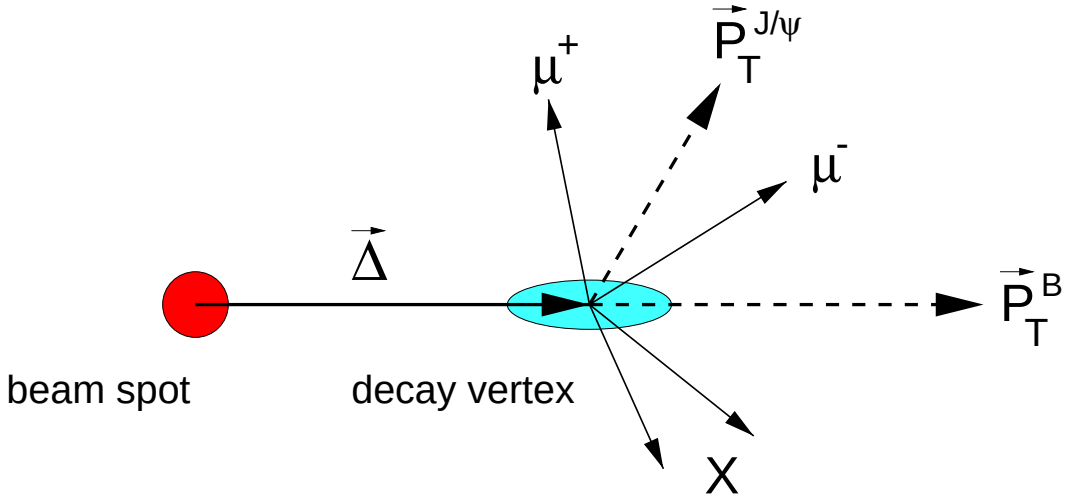


Figure 3.4: Transverse decay length measurement in an inclusive $B \to J/\psi$ decay. The beamline is orthogonal to the page. The muons tracks yield $\vec{P}_T^{J/\psi}$ and $\vec{\Delta}$. The other B-decay products, X, are not identified. There are uncertainties on the positions of the primary vertex and the B-decay vertex. The decay angles are exaggerated and are not intended to be realistic.

than 300 μm. With this requirement, the average values of $\sigma_{L_{xy}}$ are approximately 60 μm and 110 μm for SVX-SVX and SVX-CTC events respectively. Candidates with $\sigma_{L_{xy}}$ over 300 μm are reclassified as CTC-CTC events and refitted.

After this selection procedure, the fractions of the three types of dimuon candidates are approximately 33% CTC-CTC, 54% SVX-SVX and 13% SVX-CTC. From here on, SVX-SVX and SVX-CTC events, which both have precise vertex information, are grouped together into the "SVX sample". CTC-CTC events, which do not have precise vertex information, are called the "CTC sample".

The measurement of L_{xy} for events in the SVX sample is converted into an estimate of the proper decay time of the J/ψ decay vertex. For J/ψ mesons originating from B-hadron decays, the distribution of proper decay times would be exponential, decaying with a time constant equal to the average B-hadron lifetime of 1.533 ± 0.036 ps[3]. If the B-hadron were

[3]Although the B^0, B^+, B_S^0 and Λ_b have somewhat different lifetimes, this is the average lifetime for the mixture of B-hadrons produced at the Tevatron [115].

fully reconstructed, its momentum would be known and its proper decay time t_{proper} could be determined exactly:

$$ct_{proper} = \frac{L_{xy}^B \cdot m_B}{P_T^B} \qquad L_{xy}^B = \frac{\vec{\Delta} \bullet \vec{P}_T^B}{P_T^B} \tag{3.2}$$

However, for this analysis it is not practical to reconstruct the B-hadron decays fully, since the efficiency for doing so is low. Therefore a quantity called the "pseudo-proper decay length" (and denoted ct) is used instead:

$$ct = \frac{L_{xy} \cdot m_{J/\psi}}{F_{corr} \cdot P_T^{J/\psi}} \tag{3.3}$$

This uses the known transverse momentum of the J/ψ candidate, rather than the B-hadron. The world average value of 3.09688 GeV/c^2 is used for $m_{J/\psi}$ [116]. The factor F_{corr} is necessary to correct for the usage of the J/ψ kinematic quantities rather than the B-hadron quantities. It is obtained by Monte Carlo simulation of $B \to J/\psi$ decays [115]. The numerical value depends on $P_T^{J/\psi}$:

$$F_{corr}(P_T^{J/\psi}) = 2.438 \cdot e^{-1.177 \cdot P_T^{J/\psi}} + 0.8357 \tag{3.4}$$

Section 4.1 describes how the ct of each J/ψ candidate in the SVX sample is used to separate prompt production from B-decay.

The final selection requirements are then applied to the J/ψ candidate. The z position of its decay vertex must be within 60 cm of the centre of the detector. This is a standard CDF requirement, used to remove the long tails of the z vertex distribution. The J/ψ rapidity must satisfy $|y^{J/\psi}| < 0.6$. Because the CMU covers $|\eta| \lesssim 0.6$ there are very few events beyond $|y^{J/\psi}| < 0.6$, but it is useful to have a definite kinematic boundary. Candidates with $P_T^{J/\psi} < 4.0$ GeV/c are rejected as they are not kinematically suitable for the polarization measurement. The trigger efficiency is very low in this region. Approximately 180,000 signal J/ψ events remain in the data sample after all of the above requirements.

The candidates are divided into eight bins in $P_T^{J/\psi}$, spanning the range $4 - 30$ GeV/c . The P_T spectrum falls quite steeply, so the higher P_T bins are wider; even so they contain significantly fewer candidates. The last bin, from $20-30$ GeV/c , does not contain a sufficient number of events for a good polarization measurement, but is listed here for comparison.

Table 3.2: Dimuon mass signal and sideband windows for each $P_T^{J/\psi}$ bin. The values of σ have been measured and rounded to the nearest 2.5 MeV/c^2 . The last column lists the number of signal events, estimated from sideband subtraction.

P_T bin (GeV/c)	σ (MeV/c^2)	Signal region (MeV/c^2)	Lower sideband (MeV/c^2)	Upper sideband (MeV/c^2)	Events (signal)
4-5	15	3052-3142	2992-3037	3157-3202	45,000
5-6	17.5	3044.5-3149.5	2974.5-3027	3167-3219.5	46,000
6-8	17.5	3044.5-3149.5	2974.5-3027	3167-3219.5	51,000
8-10	20	3037-3157	2957-3017	3177-3237	21,000
10-12	22.5	3029.5-3164.5	2939.5-3007	3187-3254.5	8,000
12-15	27.5	3014.5-3179.5	2904.5-2987	3207-3289.5	4,200
15-20	30	3007-3187	2887-2977	3217-3307	1,600
20-30	35	2992-3202	2852-2957	3237-3342	380

The dimuon mass distributions in each P_T bin are shown in Figure 3.5. The signal to background ratio is on the order of 10:1 and improves as P_T increases. For subsequent use in discriminating between properties of signal and background events, signal and sideband windows are defined about the J/ψ peak. The peak widens with increasing $P_T^{J/\psi}$, due to the deteriorating momentum resolution of the CTC at high track P_T. So, the signal and sideband windows are defined as $\pm 3\sigma$ and $\pm(4-7)\sigma$ around the J/ψ mass, where σ is the width of the peak. These values are summarized in Table 3.2.

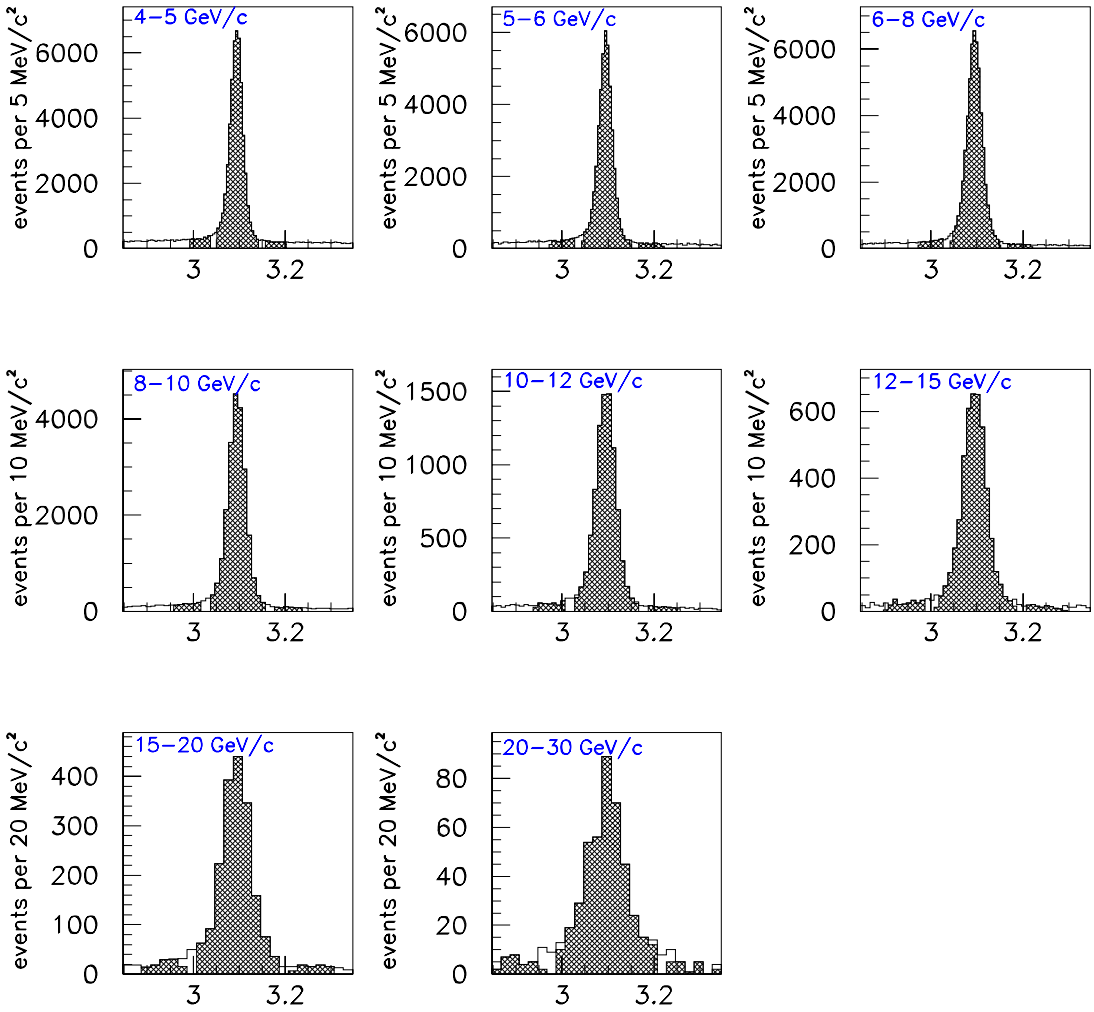


Figure 3.5: The J/ψ peak in the dimuon mass distribution, in eight $P_T^{J/\psi}$ bins. Shaded areas denote signal and sideband windows. Note that the signal and sideband boundaries do not all coincide with the boundaries of the histogram bins.

Chapter 4

J/ψ Polarization Analysis

In general, polarizations are measured using the angular distribution of daughter particles produced in a particle decay. In this analysis, the primary quantity of interest is the polarization of directly produced J/ψ charmonia. In the case of direct production, the appropriate axis for defining a decay angle is the direction of J/ψ movement in the $p\bar{p}$ centre-of-mass frame (which is also the CDF lab frame). The decay angle is called θ^* and is defined to lie between the positive muon direction[1] in the J/ψ rest frame and the J/ψ direction in the lab frame. Figure 4.1 provides an illustration.

The polarization determines the distribution of the decay angle:

$$\frac{d\Gamma}{d\cos\theta^*} \propto \frac{3}{2(\alpha+3)}(1+\alpha\cos^2\theta^*) \tag{4.1}$$

This distribution is derived in Appendix A. The quantity $\cos\theta^*$ can take on values between -1 and $+1$; the factor $\frac{3}{2(\alpha+3)}$ normalizes the above expression to unit area. The distribution is symmetric about $\cos\theta^* = 0$ in accordance with parity conservation. The polarization parameter α is equal to $+1$ for fully transversely polarized production, where transverse polarization refers to helicity ± 1. For fully longitudinal (helicity 0) polarization α is equal to -1. Between these two extremes lies a mixture of transverse and longitudinal production. Unpolarized production consists of equal fractions of helicity states $+1$, 0 and -1, and corresponds to $\alpha = 0$. Another parameter which is used to quantify polarization is the

[1] The negative muon direction would serve equally well, but one or the other should be used consistently.

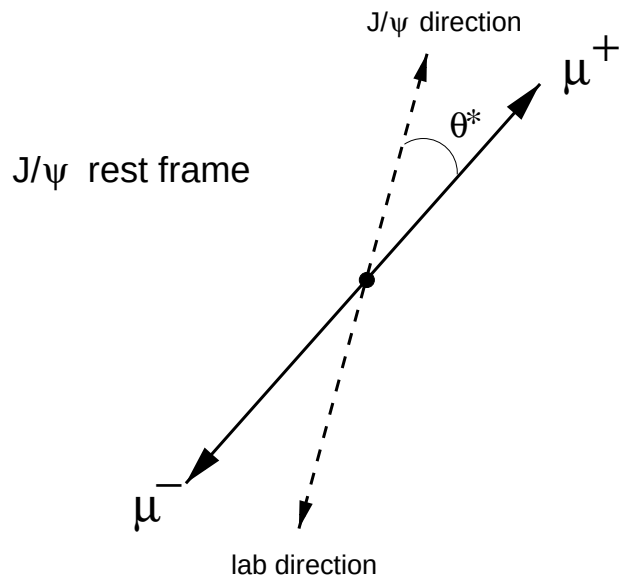


Figure 4.1: The J/ψ decay shown in its rest frame. The muons emerge with equal and opposite momenta, with polar decay angle θ^*.

longitudinally polarized fraction η,

$$\eta = \frac{1-\alpha}{\alpha+3} \tag{4.2}$$

which is equivalent to the production density matrix element ρ_{00} [117]. This analysis only concerns the diagonal elements of the density matrix. The off-diagonal elements produce terms in the decay distribution which depend on the azimuthal decay angle ϕ^*, which are discussed further in Appendix A but are not measured here.

The natural way to measure polarization, then, is to fit the distribution of $\cos\theta^*$ in the data to Equation 4.1. The method used for this fit is described in Section 4.3. However, several effects need to be dealt with and incorporated into the fit. The first is the dependence of the detector acceptance upon $\cos\theta^*$. For example, in a decay with a large value of $|\cos\theta^*|$, one muon emerges nearly in the same direction as the J/ψ, but the other is emitted almost backwards and so has a low momentum in the lab frame. For a J/ψ moving more or less orthogonally to the beamline, this implies that the second muon will have a low transverse momentum, and is likely to fail the trigger or the selection requirements. Therefore events with large values of $|\cos\theta^*|$ have a significantly lower probability of entering the data sample.

It is important to model the detector, trigger and event selection acceptance accurately, so that they can be taken into account in the polarization fit. The acceptance modeling is described in Section 4.2.

The second effect to be dealt with is the existence of different sources of J/ψ production: direct, feeddown and B-decay. The direct polarization is the quantity of greatest interest, however, direct J/ψ mesons cannot always be distinguished from other types on an event by event basis. In this analysis, prompt and B-decay production can be separated to a large extent based on their ct distributions. This procedure is incorporated in the fit, which obtains separate polarizations for prompt production (α_P) and B-production (α_B). Section 4.1 describes how the ct distribution of events in the SVX sample is used to make an approximate separation of prompt and B-decay production.

Prompt production itself comprises direct production and feeddown from the decay of heavier charmonia. The fraction of prompt J/ψ production due to feeddown has been measured to be $36 \pm 6\%$ [51]. This fraction does not vary significantly with $P_T^{J/\psi}$. The feeddown consists mainly of χ_{c1} and χ_{c2} decays to $J/\psi\ \gamma$, as well as $\psi(2S) \rightarrow J/\psi\ \pi\pi$. The χ_c signal can be reconstructed by combining J/ψ candidates with photon candidates, as shown in Figure 4.2. While it would be desirable to isolate the direct polarization from that of the feeddown by identifying feeddown events, this is not feasible, for two reasons. Firstly, due to the low energy photon, the acceptance and efficiency for reconstructing the decay $\chi_c \rightarrow J/\psi\ \gamma$ are small. Only about 10% of the decays can be reconstructed. Polarization measurements on reconstructed χ_c decays therefore have poor statistical precision. Secondly, the photon reconstruction efficiency depends very strongly on its energy, which is correlated with the angle θ^*. The reconstructed χ_c sample is therefore seriously biased in its polarization. In light of these difficulties, this analysis only goes so far as to extract the prompt polarization. This quantity can in fact be predicted theoretically, as will be discussed in Chapter 5.

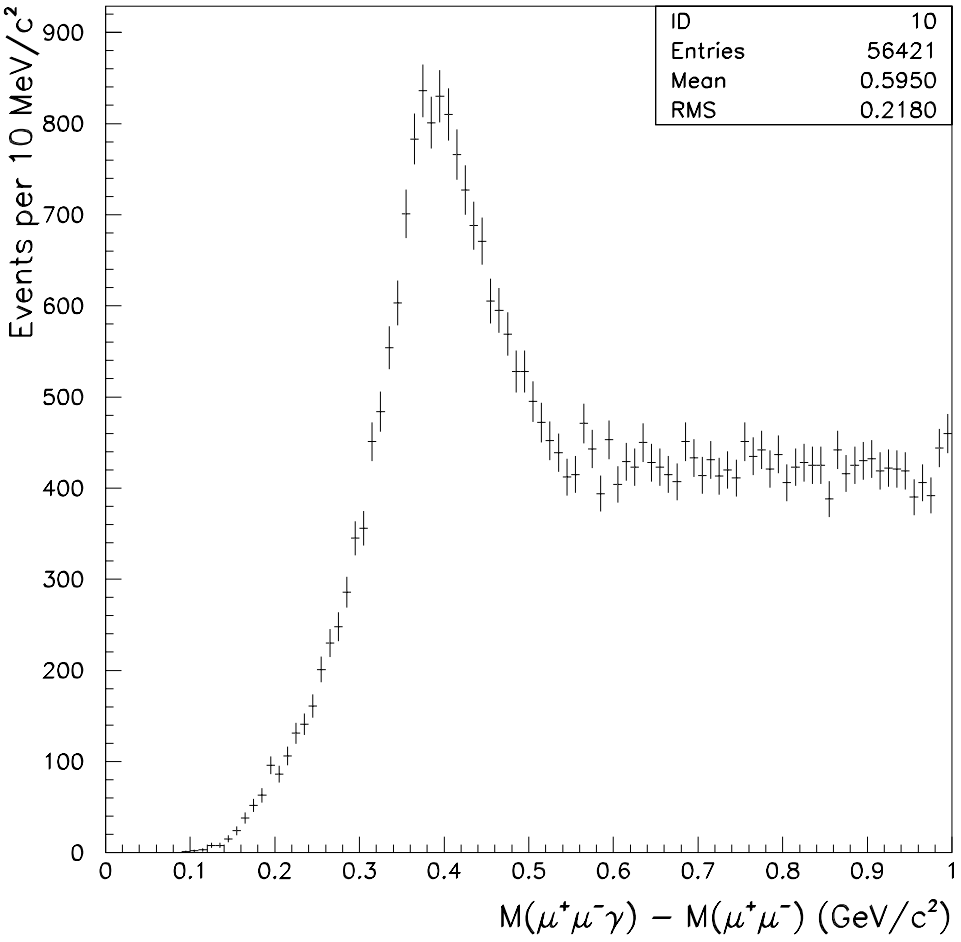


Figure 4.2: Reconstructed $\chi_c \to J/\psi\ \gamma$ decays in the J/ψ data sample. Photon candidates consist of CES clusters in CEM towers with at least 1.0 GeV of deposited energy. The χ_c signal appears as a peak at 0.4 GeV/c in the mass difference ($M_{\mu^+\mu^-\gamma} - M_{\mu^+\mu^-}$) histogram, on top of a sizeable background. The peak only contains on the order of 7,000 reconstructed χ_c decays. It consists of χ_{c1} and χ_{c2} peaks which cannot be resolved; the χ_{c0} has a much smaller branching fraction to $J/\psi\ \gamma$ and is not observed.

4.1 The ct Fit

The pseudo-proper decay length of J/ψ candidates in the SVX sample is used to separate prompt and B-decay polarization. Prompt events have ct consistent with zero, whereas B-decays have an exponential ct distribution. To provide a nearly pure prompt sample and a nearly pure B-decay sample, the SVX sample will be divided into two ranges of ct: a short-lived sample of events with ct near zero, and a long-lived sample of events with ct significantly greater than zero. The finite resolution on ct implies that the two samples will not be pure. A maximum likelihood fit is applied to the overall ct distribution to determine the actual purities, which will be used in the polarization fit.

Fits to ct distributions have previously been used by CDF to measure average B-hadron lifetimes [115], and this analysis uses the same general procedure. First, the ct distribution of non-J/ψ background is determined using events in the sideband windows. A second fit then determines the prompt and B-decay fractions in the signal window.

4.1.1 Background fit

Events in the dimuon mass sidebands are used to model the ct distribution of background beneath the J/ψ peak. Their ct distribution is parameterized as a prompt Gaussian centered at $ct = 0$, with asymmetric exponential tails at positive and negative ct. The negative tail simply reflects the fact that the ct resolution of CDF is not a perfect Gaussian. The positive tail also allows for dimuon background produced at positive ct, for example sequential muonic B-decays ($b \to c\mu^- \to s\mu^+\mu^-$).

The background ct shape parameterization is:

$$\begin{aligned} \text{for } ct > 0: \quad Bgnd(ct) &= (1-\phi^+-\phi^-)G(ct;\sigma_b) + \phi^+ E(ct;\lambda^+) \\ \text{for } \ ct \le 0: \quad Bgnd(ct) &= (1-\phi^+-\phi^-)G(ct;\sigma_b) + \phi^- E(-ct;\lambda^-) \end{aligned}$$

where the normalized Gaussian and exponential functions are:

$$\begin{aligned} G(x;\sigma) &= \tfrac{1}{\sqrt{2\pi}\sigma} e^{-x^2/2\sigma^2} \\ E(x;\lambda) &= \tfrac{1}{\lambda} e^{-x/\lambda} \end{aligned}$$

The five fit parameters are:

σ_b	standard deviation of prompt Gaussian
ϕ^+	fraction of positive exponential
ϕ^-	fraction of negative exponential
λ^+	length scale of positive exponential
λ^-	length scale of negative exponential

The resulting log likelihood function is:

$$\mathcal{L} \;=\; -\sum_{i}^{events} \ln(Bgnd(ct_i)) \tag{4.3}$$

It is minimized, using the general function minimization software MINUIT [118], which returns the fitted values of the parameters.

4.1.2 Signal fit

After the sidebands are fitted to determine the background distribution, events in the signal window are fitted to a sum of background, prompt signal and B-decay signal distributions. The prompt signal ct distribution is parameterized as a prompt Gaussian with two pairs of symmetric exponential tails. In effect this is the ct resolution function, and it is implicitly assumed to be symmetric about $ct = 0$. The two pairs of tails are necessary to reproduce the shape of the data well at negative values of ct. The first, shorter, tail has a length scale λ on the order of 50 μm whereas the second tail is on the order of 400 μm. The parameterization is:

$$Prompt(ct) \;=\; (1 - f^1_{tail} - f^2_{tail})G(ct;\sigma) \;+\; \sum_{i=1}^{2} \frac{f^i_{tail}}{2} E(|ct|;\lambda^i_{tail}) \tag{4.4}$$

The B-decay signal ct distribution is parameterized as a positive exponential decay, convoluted with the above resolution function:

$$B(ct) \;=\; \int_0^\infty Prompt(y - ct) \cdot E(ct;\lambda_B)\; dy \tag{4.5}$$

The total ct distribution in the signal window is the sum of the background, prompt and B-decay components:

$$Total(ct) \;=\; F_{bgnd} \cdot Bgnd(ct) + (1 - F_{bgnd})(F_B \cdot B(ct) + (1 - F_B) \cdot Prompt(ct)) \tag{4.6}$$

The eight parameters introduced above are:

F_{back}	overall background fraction
F_B	overall B signal fraction
σ	sigma of prompt Gaussian in resolution function
f^1_{tail}	fraction of resolution function in short exponential tails
λ^1_{tail}	length scale of short exponential tails
f^2_{tail}	fraction in long exponential tails
λ^2_{tail}	length scale of long exponential tails
λ_B	average B-hadron lifetime, multiplied by c

The five background parameters in $Bgnd(ct)$ are fixed to the values obtained in the background fit. The background fraction F_{back} is constrained to the number of events in the sidebands. This is done by multiplying the likelihood function by a Poisson function[2] of the number of sideband events and the fitted number of background events. The log likelihood function to be minimized, again using MINUIT, is:

$$\mathcal{L} \;=\; -\sum_{i}^{events} \ln(Total(ct_i)) \quad - \ln P_{Poisson}(N_{side}; F_{back} \cdot N_{signal}) \tag{4.7}$$

4.1.3 ct fit results

The first ct fit to be performed is applied to data over the whole P_T range: $4 - 30$ GeV/c . The purpose of this is to determine the optimum value of ct at which to separate the short-lived sample from the long-lived sample. Figure 4.3 shows the fitted prompt and B-decay ct distributions in a limited ct range near zero. They cross at $ct = 0.013$ cm, so this value is chosen as the boundary between the short-lived and long-lived sample. The full ct fit is shown in Figure 4.4. The fitted value of λ_B is 445 ± 5 μm, which is consistent with published CDF measurements [115].

After the fit over the full P_T range is done, one fit for each of the seven P_T bins is performed. The procedure is the same, except that the B lifetime parameter is fixed to 445 μm, to improve the resolution on the parameters of interest. Also, in the highest P_T

[2] Approximated here by a Gaussian: $P_{Poisson}(a;b) = \frac{1}{\sqrt{2\pi}a} e^{-(b-a)^2/2a^2}$.

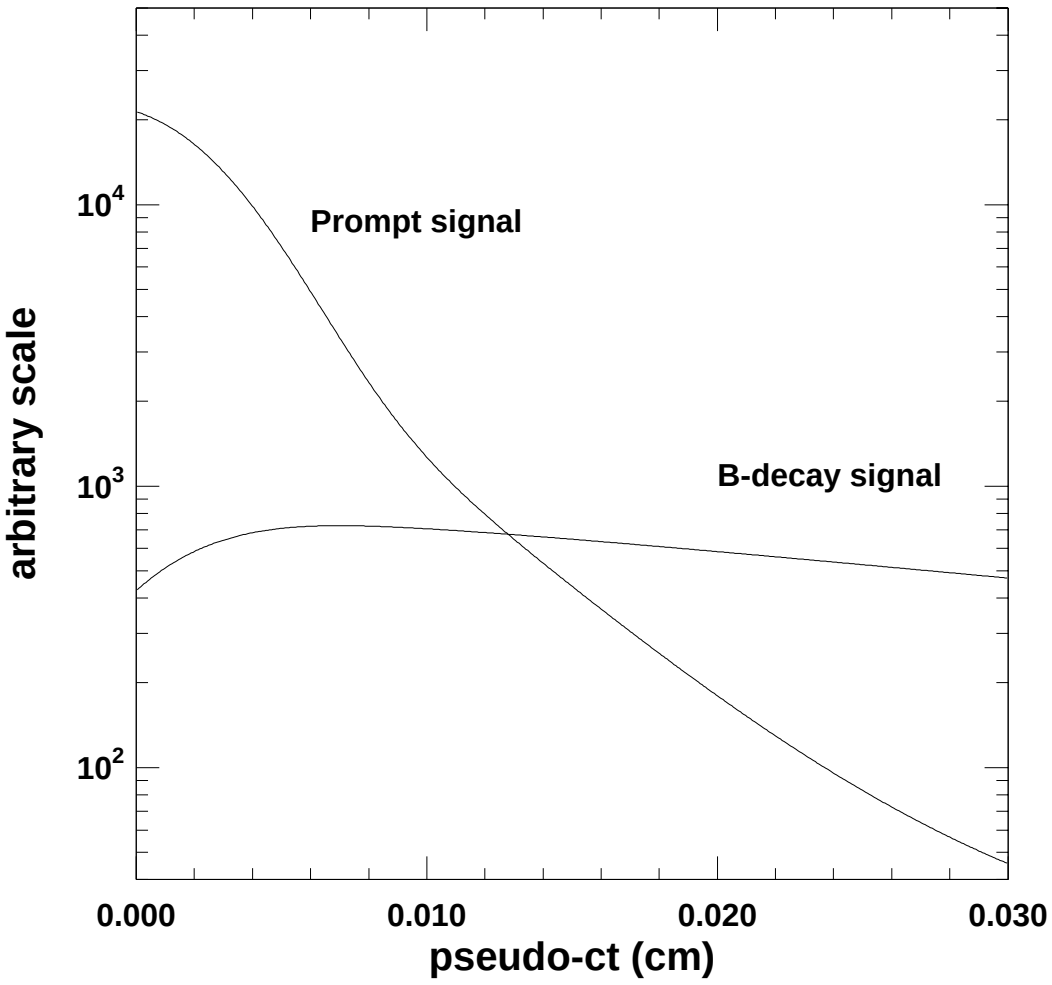


Figure 4.3: Fitted prompt and B-decay ct distributions for the full P_T range, shown over a limited ct range. The B-decay component becomes larger than the prompt component at $ct = 0.013$ cm, so this value is chosen as the boundary between the short-lived and long-lived samples.

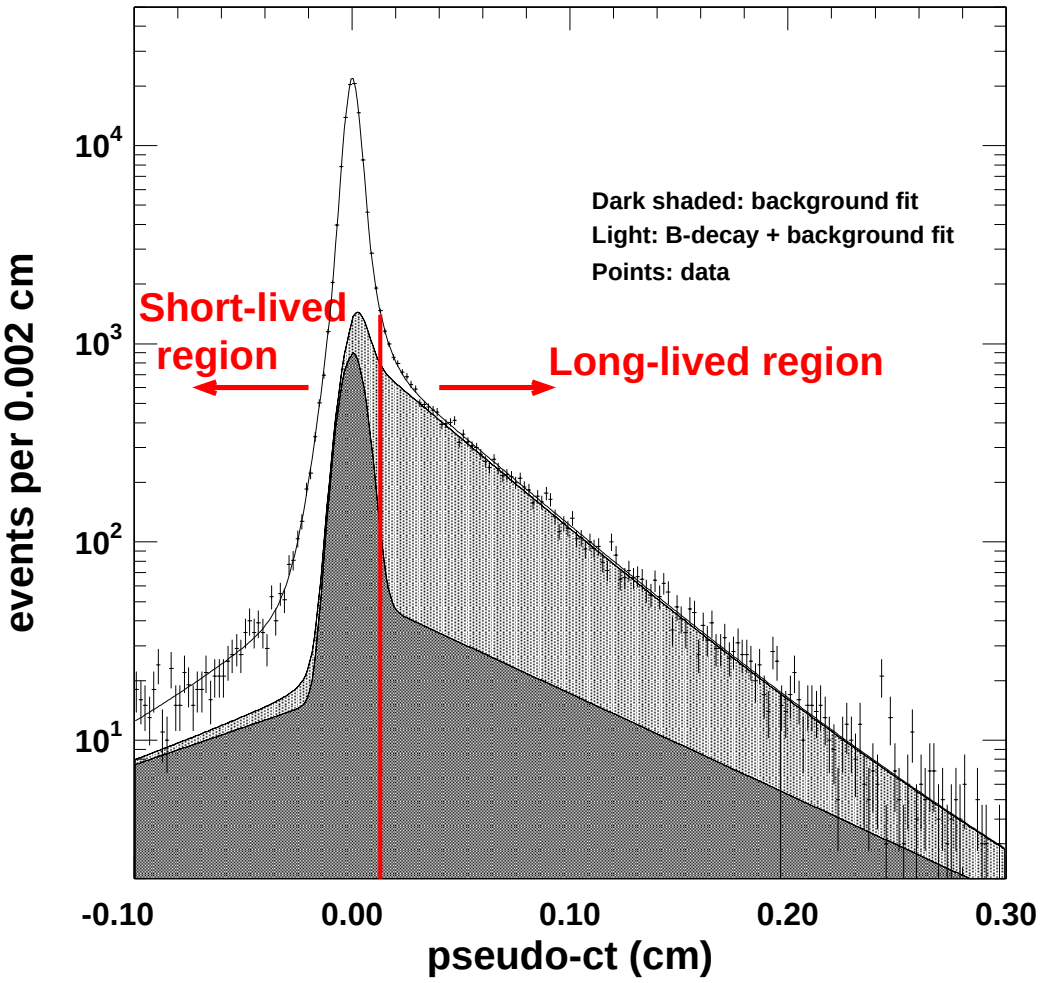


Figure 4.4: The ct fit for the full P_T range. The data is represented by points with statistical uncertainties. The lowest shaded area shows the background as fitted in the sidebands. The larger shaded area is the fitted sum of background and B-decay signal; its constant slope at positive ct shows the exponential distribution of B-decay times. The highest curve is the full fit including the prompt peak around $ct = 0$. The boundary between short- and long-lived regions is also shown. The vertical line near 0.2 cm is only a graphics artefact.

Table 4.1: The ct background fit results, from the mass sidebands.

$P_T^{J/\psi}$ (GeV/c)	σ_b (μm)	ϕ^+ (%)	ϕ^- (%)	λ^+ (μm)	λ^- (μm)
4-5	61.3±1.4	17.9±0.8	11.2±0.6	1011±47	1263±75
5-6	59.9±1.5	20.8±0.9	9.4±0.6	873±42	1388±98
6-8	57.7±1.8	29.0±1.1	11.4±0.8	893±38	1007±68
8-10	41.8±2.6	34.9±2.0	11.8±1.3	616±40	817±91
10-12	35.3±4.6	45.1±3.2	13.9±2.2	647±57	780±130
12-15	29.9±4.5	51.9±4.0	12.0±2.4	635±65	730±150
15-20	25.1±4.4	55.5±5.4	9.4±3.0	530±72	570±190
4-30	57.4±0.8	24.9±0.5	10.8±0.4	853±19	1151±40

bins some of the tail parameters need to be fixed for the fit to converge. Tables 4.1 and 4.2 summarize the fitted parameters for the full-range fit and for each P_T bin.

The SVX sample is now split into short-lived and long-lived samples. They are defined as:

$$\text{short-lived sample:} \quad -0.100 \text{ cm} \leq ct \leq 0.013 \text{ cm}$$

$$\text{long-lived sample:} \quad 0.013 \text{ cm} \leq ct \leq 0.300 \text{ cm}$$

Outside the range of -0.1 to 0.3 cm there are very few events, and those are likely to be poorly reconstructed, so they are dropped. The short-lived and long-lived samples are to be used separately in the polarization fit, where it will be necessary to know fractions of prompt production and B-decay in each. These fractions are obtained by integrating the fitted ct distributions over the appropriate ranges. The resulting fractions are 1) f_p^0, the fraction of signal events in the short-lived region which are prompt, and 2) f_B^+, the fraction of signal events in the long-lived region which come from B-decays. They are listed in Table 4.3.

In the CTC sample, events have no ct measurement, so no lifetime fitting can be performed. However, the overall B-fraction in the CTC sample is needed in the polarization fit. This is taken to be the same as the overall B-fraction in the SVX sample: the value of

Table 4.2: The ct signal window fit results. An asterisk denotes a fixed parameter.

$P_T^{J/\psi}$	F_{back} (%)	F_B (%)	σ (μm)	f_{tail}^1 (%)	λ_{tail}^1 (μm)	f_{tail}^2 (%)	λ_{tail}^2 (μm)
4-5	8.91±0.16	12.96±0.28	39.29±0.40	31.9±2.6	53.9±2.4	2.1±0.3	472±54
5-6	8.20±0.16	14.84±0.31	35.22±0.43	36.6±3.0	53.7±3.1	3.1±0.4	407±60
6-8	6.41±0.13	18.12±0.29	30.54±0.36	37.7±2.0	56.4±2.2	1.6±0.3	479±94
8-10	5.82±0.20	23.80±0.49	25.44±0.65	50.5±3.8	44.1±2.4	2.0±0.6	350±110
10-12	6.07±0.30	28.87±0.83	24.13±0.76	37.3±5.0	46.5±4.8	2.1±0.9	380±130
12-15	7.06±0.51	33.0±1.2	22.8±1.3	52±10	33.6±3.6	2.0±1.2	350*
15-20	8.91±0.92	40.1±1.9	21.3±1.2	14.4±9.1	41±15	2.0*	350*
4-30	7.52±0.08	17.62±0.16	32.56±0.22	42.9±1.4	49.4±1.0	2.3±0.2	395±32

Table 4.3: Fractions of prompt and B in short- and long-lived ct regions, calculated from ct-fit results. Quoted uncertainties correspond to varying fitted value of F_B by $\pm 1\sigma$ (see Section 4.4.1).

$P_T^{J/\psi}$ (GeV/c)	f_p^0 (%)	f_B^+ (%)
4-5	$96.31\mp^{0.08}_{0.09}$	$83.16\pm^{0.34}_{0.35}$
5-6	95.68∓0.10	82.52±0.35
6-8	94.60∓0.10	$86.89\pm^{0.22}_{0.23}$
8-10	$92.58\mp^{0.19}_{0.18}$	$92.09\pm^{0.19}_{0.20}$
10-12	$90.56\mp^{0.35}_{0.34}$	94.18±0.22
12-15	88.83∓0.54	$96.74\pm^{0.17}_{0.18}$
15-20	85.4∓1.0	$98.05\pm^{0.14}_{0.16}$

F_B in Table 4.2. This assumption is justified by previous comparisons between SVX and CTC events, which indicate that their B-decay content is the same [119]. Also, separate ct fits to SVX-SVX and SVX-CTC events give consistent B-fractions, indicating that the CTC-CTC composition is unlikely to be significantly different.

4.2 Acceptance Modeling

Several factors determine the acceptance[3] for produced J/ψ mesons to reach the data sample. A muon pair must first have the correct geometric and kinematic configuration for both muons to reach the CMU. The trigger must then fire at all three levels. The muons must subsequently be reconstructed offline and pass all of the event requirements listed in Section 3.4.

As mentioned at the beginning of this chapter, the most significant aspect of the J/ψ acceptance is that decays at large $|\cos\theta^*|$ are unlikely to reach the recorded data sample. To account for this and other acceptance effects, the polarization fit makes use of large simulated samples of $J/\psi \to \mu^+\mu^-$ decays. As described in Section 4.3, the distribution of $\cos\theta^*$ in data is compared with the distribution in these Monte Carlo samples, which have the acceptance taken into account.

The Monte Carlo simulation uses the same software framework as the offline data analysis. The creation of a Monte Carlo sample begins with the generation of J/ψ mesons distributed uniformly in azimuth and rapidity, as is expected physically. They are generated with a transverse momentum distribution based on CDF's measured differential cross section $d\sigma/dP_T^{J/\psi}$ [50]. There are in fact three different $P_T^{J/\psi}$ distributions which may be used: the prompt spectrum, the B-decay spectrum and the inclusive spectrum, which is the sum of the two. In each case, the measured cross sections are fitted to a smooth parameterization:

$$\frac{d\sigma}{dP_T} \propto \frac{1}{(b^2 + P_T^2)^n} \tag{4.8}$$

Figure 4.5 shows the data and fit, and Table 4.4 lists the fitted parameters.

[3] For simplicity, the term acceptance is used here to include efficiencies and well as acceptances.

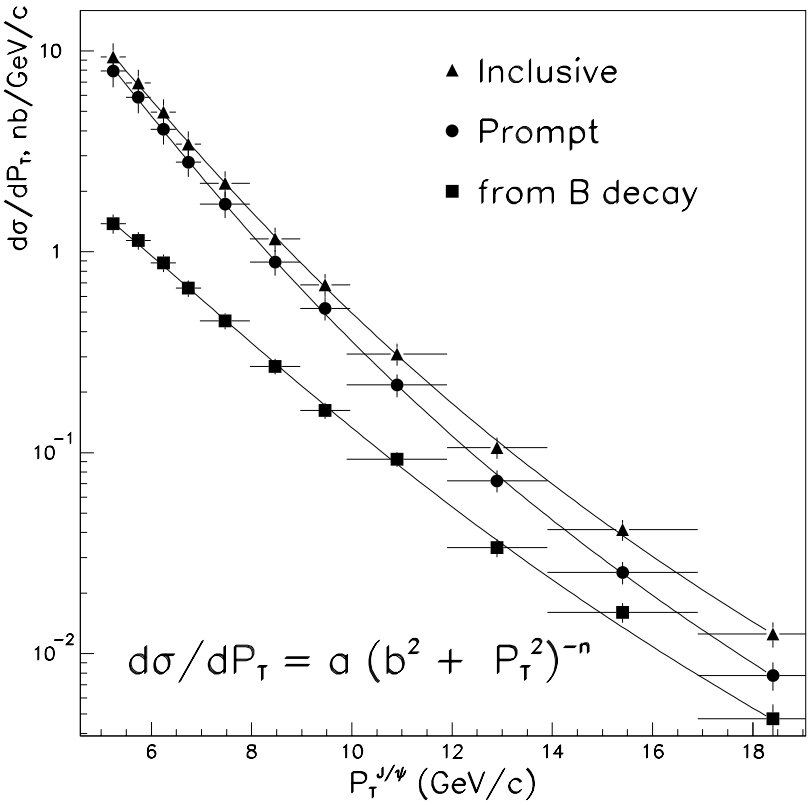


Figure 4.5: Parameterization of J/ψ transverse momentum spectra. Points: Run 1A $d\sigma/dP_T$ measurement. Curves: fitted parameterizations, used in Monte Carlo generation.

Table 4.4: Fitted parameters for the $P_T^{J/\psi}$ spectra used in acceptance Monte Carlo.

Spectrum	b (GeV/c)	n
Inclusive J/ψ	5.07±0.26	3.442±0.035
Prompt J/ψ	5.02±0.26	3.613±0.036
J/ψ from B-decay	6.27±0.22	3.251±0.027

Next, the J/ψ decays are simulated, using the appropriate distribution of $\cos\theta^*$. For the polarization fit, both transverse ($\alpha = 1$) and longitudinal ($\alpha = -1$) Monte Carlo samples are generated. For validation purposes unpolarized samples are also generated. The distribution of the the azimuthal decay angle ϕ^* is generated flat.

The simulated muons are then passed through a CDF detector simulation called QFL [120]. QFL is a fast simulation which uses parameterizations to model the response of the tracking detectors, calorimeters and muon chambers to particles. When QFL simulates the passage of particles through CDF, its output resembles the output of the actual DAQ system, so the same offline reconstruction software can be applied here as for real data. QFL replicates the geometric and kinematic acceptance of the detector.

At this point a trigger efficiency simulation is applied. The Level 1 and Level 2 dimuon trigger efficiencies have been measured [106, 121] and the parameterized efficiencies can be applied to simulated muon pairs using two CDF software packages. The routines are called MU2TRG [121] for the Run 1A trigger and DIMUTG [122] for the three Run 1B triggers. To simulate the effects of the trigger efficiency, DIMUTG (or MU2TRG in the case of a Run 1A simulation) is used to evaluate each simulated event and calculate the probability for it to pass the Level 1 and 2 dimuon triggers. Events are then randomly discarded based on their probability. The Level 3 efficiency is not simulated. It is not correlated with $\cos\theta^*$ because the Level 3 trigger does not consider quantities which depend strongly on muon P_T.

In the last stage of the simulation, each J/ψ decay is reconstructed using the same software routine as is used for data reconstruction. The same event requirements are applied. The only difference is that ct information is not simulated; it is not needed because separate prompt and B-decay samples can be generated.

Figure 4.6 shows examples of the $\cos\theta^*$ distributions in a simulated sample of unpolarized events. Since an unpolarized sample starts with a flat distribution of $\cos\theta^*$, Figure 4.6 in effect shows the relative acceptance as a function of $\cos\theta^*$. The cutoff in $\cos\theta^*$ is very clear, moreover the cutoff value increases as P_T increases. This is why it is necessary to reproduce the P_T spectrum accurately: events at the lower end of any P_T bin have slightly lower acceptance than those at the higher end of that bin.

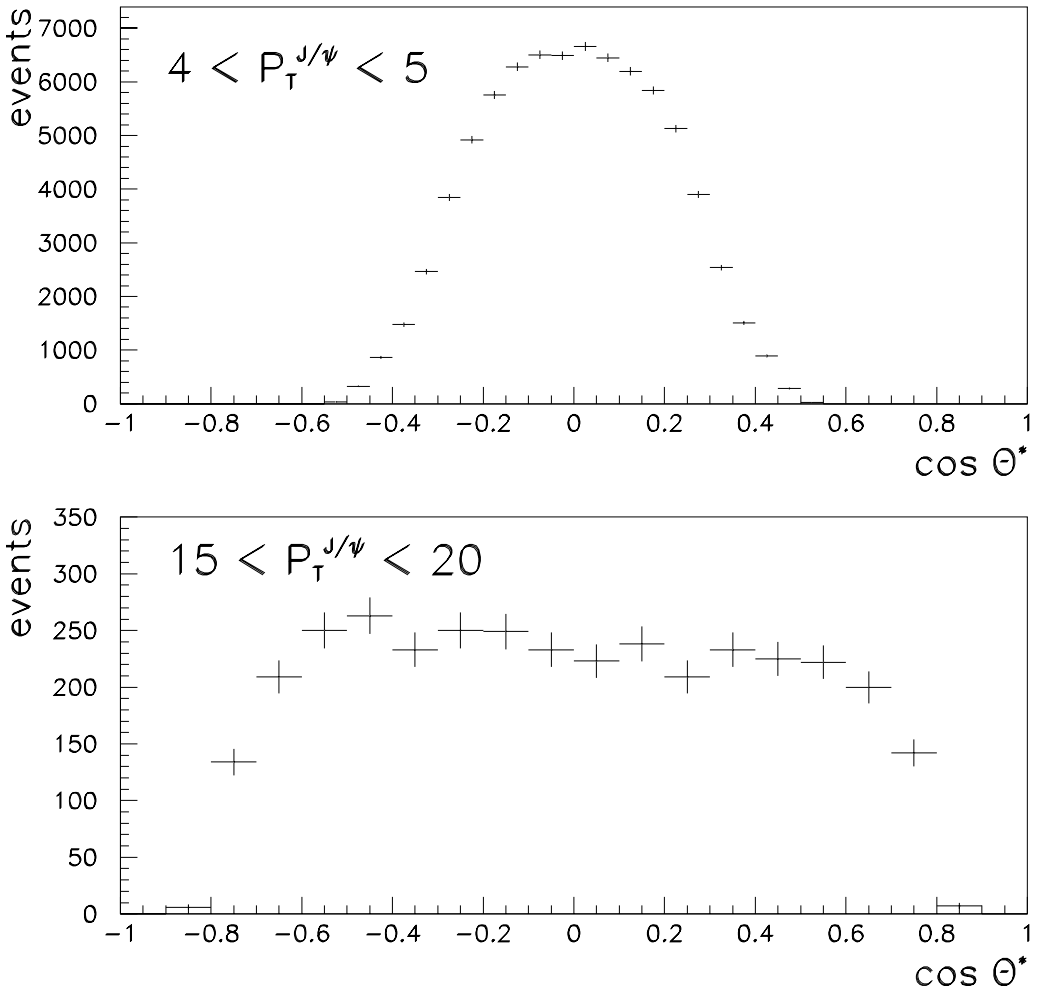


Figure 4.6: Distributions of $\cos\theta^*$ in simulated unpolarized Run 1B sample. The distributions are proportional to the acceptance, but the vertical scales are arbitrary. Two $P_T^{J/\psi}$ ranges are illustrated: the lowest P_T bin (4-5 GeV/c) and the highest (15-20 GeV/c). The acceptance reach in $|\cos\theta^*|$ increases as P_T increases.

When kinematic distributions, such as muon P_T, $P_T^{J/\psi}$ and J/ψ rapidity, are compared in the data and in the Monte Carlo samples, it is seen that the simulation reproduces the acceptance well. Figures 4.7 and 4.8 compare the distributions of J/ψ transverse momentum and rapidity in data and simulation.

4.3 Polarization Fit

The J/ψ polarization is measured using a chi-squared fit to the $\cos\theta^*$ distribution in the data. The data events are histogrammed in $\cos\theta^*$, with typical bin widths[4] of 0.05. The fit is called a "template fit", as the Monte Carlo samples are used to make histogram templates of $\cos\theta^*$ distributions. The data is then fitted to a weighted sum of two or more Monte Carlo templates to obtain the polarization. In the simplest case, one data histogram can be fit to a sum of two Monte Carlo templates: one from a longitudinally polarized sample and one from a transversely polarized sample. Longitudinal and transverse Monte Carlo samples are always generated beginning with the same number of events, before the acceptance is applied. Therefore the fitted weighting between the longitudinal and transverse templates yields the longitudinal fraction η, and hence α, by Equation 4.2. The machinery of this basic fit is described in Section 4.3.1.

The actual polarization fit used to obtain the results of this analysis is more complex, involving several data samples (SVX short-lived, SVX long-lived and CTC) and Monte Carlo samples (prompt and B-decay). It is an extension of the simple template fit, and is described in Section 4.3.2.

4.3.1 Inclusive polarization fit

In the simplest case, the "inclusive" polarization can be fitted, without separating data into subsamples or separating prompt and B-decay polarization. All J/ψ candidates are treated as CTC events, meaning that no SVX tracking information is used. This fit is not used to obtain the results of the analysis, but is described here to help explain the full fit. It is also

[4] The detector resolution on $\cos\theta^*$ is typically 0.005.

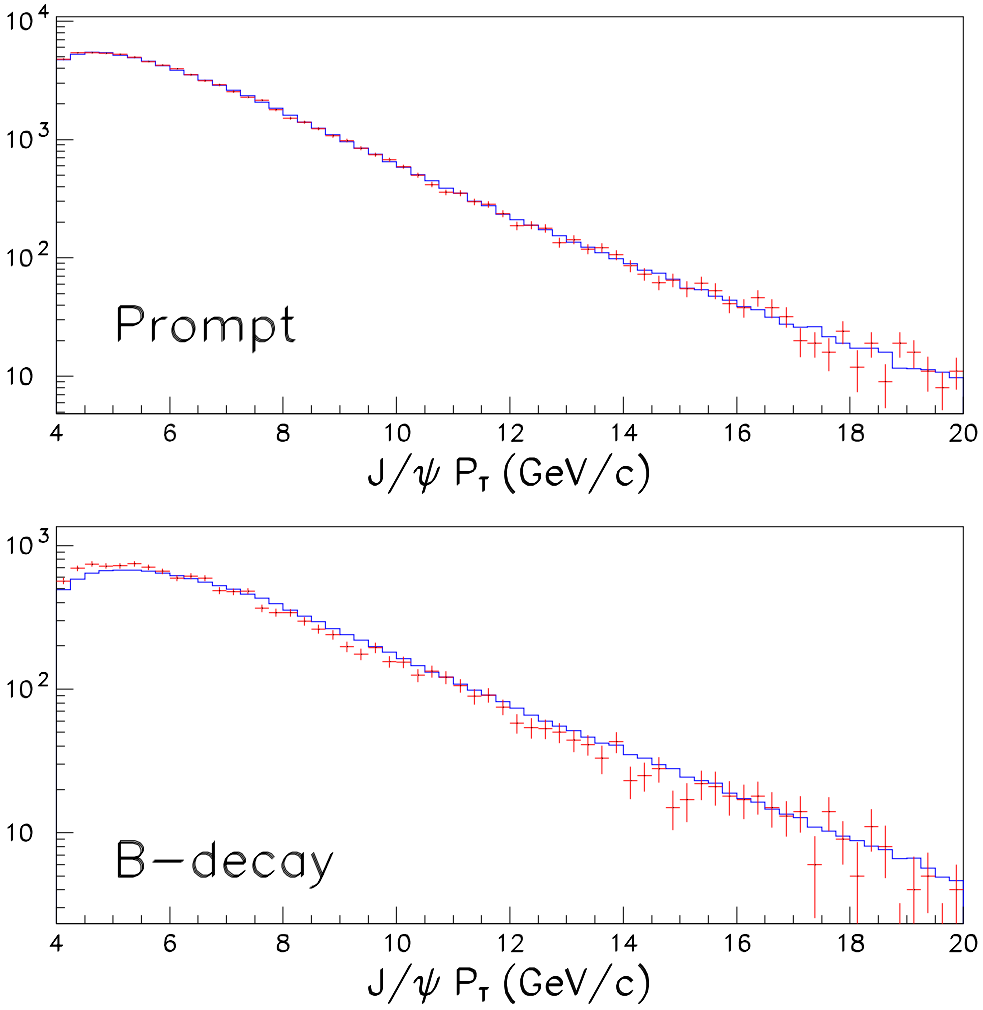


Figure 4.7: Comparison of $P_T^{J/\psi}$ distributions in data and Monte Carlo samples. Points are data, solid lines are simulation normalized to data. Separate comparisons are made for prompt production and B-decay; in data they are separated using strict ct requirements in the SVX sample, in Monte Carlo separate prompt and B-decay samples are generated, both with $\alpha = 0$.

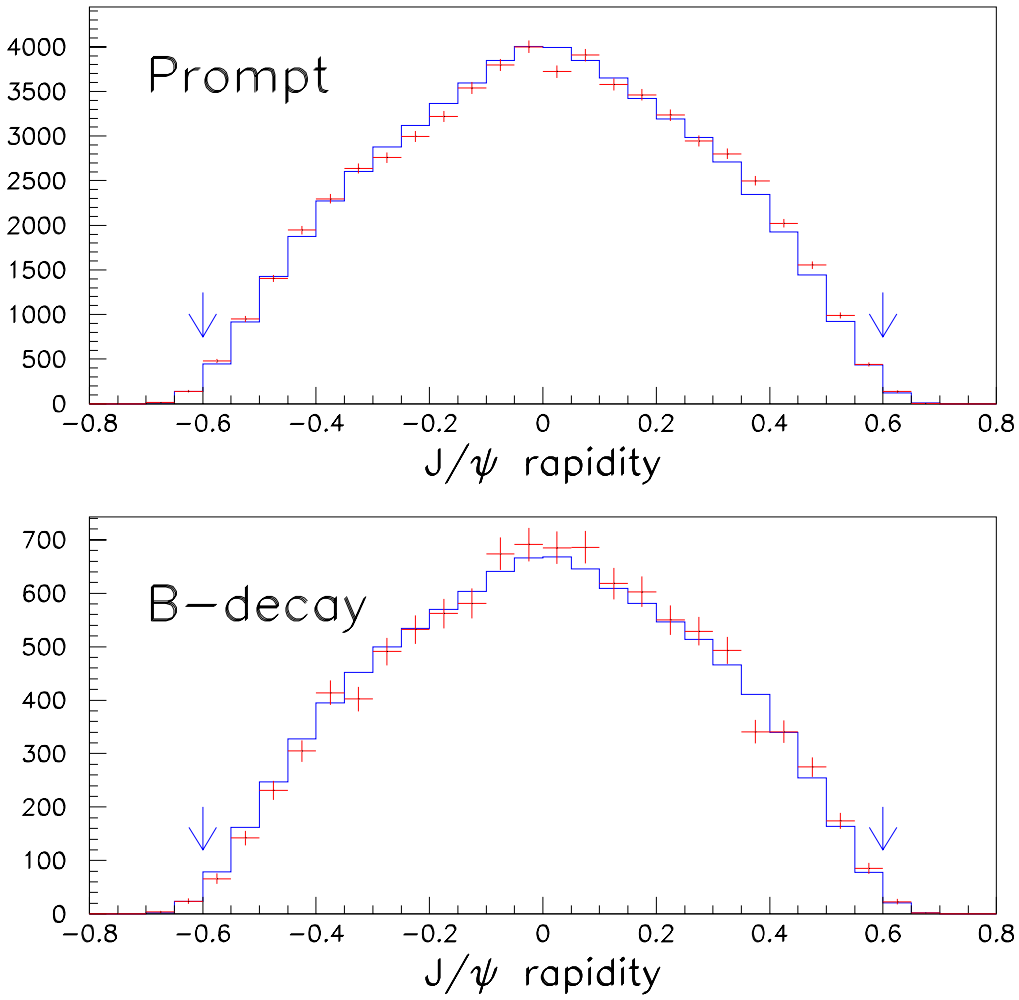


Figure 4.8: Comparison of $y^{J/\psi}$ distributions in data and Monte Carlo samples. Points are data, solid lines are simulation normalized to data. Arrows denote the selection requirement $|y^{J/\psi}| < 0.6$. Prompt and B-decay components are separated as in Figure 4.7. The Monte Carlo simulation assumes that J/ψ mesons are produced with a flat rapidity distribution.

used to test the template fitting method (see Section 4.3.3) and in one of the systematic uncertainty calculations (Section 4.4.3).

This fit uses two data $\cos\theta^*$ histograms: one from the mass signal window and one from the mass sideband windows. The sideband windows are used to estimate the $\cos\theta^*$ distribution of background events under the J/ψ peak. Two Monte Carlo templates are used: one transverse and one longitudinal. As will be described in Section 4.3.2, separate Run 1A and Run 1B samples are generated and then combined. The four histograms in $\cos\theta^*$ are denoted:

D_i: Number of signal window data events in $\cos\theta^*$ bin i

S_i: Number of sideband window data events in bin i

L_i: Number of longitudinal template events in bin i

T_i: Number of transverse template events in bin i

Although in most bins there are sufficient numbers of events for the numbers to follow Gaussian distributions, a χ^2 function is defined which takes into account the Poisson distribution of both signal and background events [123]:

$$\chi^2 = 2 \cdot \sum_i (E_i + \beta_i - D_i) - D_i \cdot \ln\left(\frac{E_i + \beta_i}{D_i}\right) + (\beta_i - S_i) - S_i \ln\left(\frac{\beta_i}{S_i}\right) \tag{4.9}$$

where E_i is the expected number of signal events in bin i, and β_i is the expected number of background events. Bins with no signal data events are not included in the fit. The β_i do not introduce any extra degrees of freedom into the fit, but are derived explicitly by requiring that

$$0 = \frac{\partial\chi^2}{\partial\beta_i} = 2(1 - \frac{D_i}{E_i + \beta_i} + 1 - \frac{S_i}{\beta_i}) \tag{4.10}$$

Equation 4.10 is quadratic in β_i, but only one of the solutions is physical. It is:

$$\beta_i = \frac{1}{4}\left(-(2E_i - D_i - S_i) + \sqrt{(2E_i - D_i - S_i)^2 + 8S_iE_i}\right) \tag{4.11}$$

The expected number of signal events is derived from the templates and depends on the polarization:

$$E_i = F_{norm}(\eta \cdot L_i + (1 - \eta) \cdot T_i) \tag{4.12}$$

Table 4.5: Results of the inclusive polarization fit applied to data. Since this is only for reference, only the statistical uncertainties are listed.

$P_T^{J/\psi}$ (GeV/c)	$\cos\theta^*$ bin width	Inclusive α	χ^2/d.o.f., C.L.
4-5	0.05	0.236±0.097	18/21, 67%
5-6	0.05	-0.001±0.073	30/23, 14%
6-8	0.05	0.209±0.054	36/27, 12%
8-10	0.05	0.266±0.065	22/29, 81%
10-12	0.05	0.084±0.084	37/29, 14%
12-15	0.1	0.14±0.11	37/15, 0.1%
15-20	0.1	-0.30±0.12	18/16, 31%

where η is the longitudinal polarization fraction. An arbitrary number of Monte Carlo events can be generated, so the factor F_{norm} is used to normalize the templates to the data. The total number of expected signal events to the total sideband-subtracted number of data events:

$$F_{norm} = \frac{\sum_i (D_i - S_i)}{\sum_i (\eta \cdot L_i + (1-\eta) \cdot T_i)} \tag{4.13}$$

In practice, the Monte Carlo samples generated are several times larger than the data sample, so that statistical fluctuations in the templates are negligible.

The software package MINUIT is used to minimize the χ^2 function. The lone fitted parameter is α, derived from η. The fit returns α and its one-standard-deviation statistical uncertainties. MINUIT allows for asymmetric uncertainties, but in practice the uncertainties are only significantly asymmetric when they are large. For reference, Table 4.5 lists the results of the inclusive fit applied to the data sample.

4.3.2 Data analysis polarization fit

The fit used to obtain the results of this analysis is based on the χ^2 method described above, but it is extended to allow for the separate measurement of prompt polarization (α_P) and B-decay polarization (α_B). The data is split into three samples: short-lived SVX, long-lived

Table 4.6: The eight Monte Carlo samples used in the data analysis polarization fit. Each contains events over the full P_T range of interest.

Sample type	Prompt $P_T^{J/\psi}$ spectrum	B-decay $P_T^{J/\psi}$ spectrum
Transversely polarized	1 Run 1A, 1 Run 1B	1 Run 1A, 1 Run 1B
Longitudinally polarized	1 Run 1A, 1 Run 1B	1 Run 1A, 1 Run 1B

SVX and CTC. More Monte Carlo templates are also required. Separate prompt and B-decay Monte Carlo samples are generated, the only difference being their $P_T^{J/\psi}$ distribution, as discussed in Section 4.2.

Separate Run 1A and Run 1B Monte Carlo samples are also generated. This accounts for the different trigger acceptances in the two running periods. Effects due to the slightly different detector geometries and $p\bar{p}$ interaction region profiles are also taken into account. The ratio of sizes of the 1A and 1B samples generated is set[5] to the ratio of their integrated luminosities: about 1:5.5. The total number of events in the Monte Carlo samples is on the order of thirty times the number of data events. The eight samples are listed in Table 4.6.

Next, Run 1A and Run 1B samples are combined, for both the data and the Monte Carlo samples. A total of six data histograms and eight Monte Carlo histograms are then filled:

D_i^0, S_i^0: SVX short-lived data, signal and sideband windows

D_i^+, S_i^+: SVX long-lived data, signal and sideband windows

D_i^{CTC}, S_i^{CTC}: CTC data, signal and sideband windows

P_{Ti}^{SVX}, P_{Li}^{SVX}: SVX prompt Monte Carlo, transverse and longitudinal

P_{Ti}^{CTC}, P_{Li}^{CTC}: CTC prompt Monte Carlo, transverse and longitudinal

B_{Ti}^{SVX}, B_{Li}^{SVX}: SVX B-decay Monte Carlo, transverse and longitudinal

B_{Ti}^{CTC}, B_{Li}^{CTC}: CTC B-decay Monte Carlo, transverse and longitudinal

Note that Monte Carlo events are separated into SVX and CTC samples just as data events

[5]The ratio of prompt and B-decay generated sample sizes, on the other hand, does not matter, as they will be normalized to the data during the fit.

are; this is to take any difference in acceptance into account. The simulation reproduces the ratio of SVX to CTC events satisfactorily, although this does not matter as the SVX and CTC samples will be separately normalized to the data in the fit. This set of histograms is generated for each of the seven P_T bins. The bin width in $\cos\theta^*$ is chosen to be 0.05 for the five P_T bins between 4 and 12 GeV/c . The highest two P_T bins have fewer events and so their $\cos\theta^*$ bin width is 0.1.

The χ^2 function is now a sum over the three data samples

$$\chi^2 = 2 \cdot \sum_{j}^{0,+,CTC} \sum_{i} (E_i^j + \beta_i^j - D_i^j) - D_i^j \cdot \ln\left(\frac{E_i^j + \beta_i^j}{D_i^j}\right) + (\beta_i^j - S_i^j) - S_i^j \ln\left(\frac{\beta_i^j}{S_i^j}\right) \quad (4.14)$$

The expected backgrounds β are calculated as before. The expected signal, however, now includes both prompt and B-decay components, each with their own polarization (α_P and α_B, or equivalently η_P and η_B). This step requires the measured prompt and B-fractions in each data sample (f_P^0, f_B^+ and F_B):

$$\begin{aligned} E_i^0 &= F_{norm}^{P0} \cdot f_P^0 \cdot (\eta_P P_{Li} + (1-\eta_P) P_{Ti}) \\ &+ F_{norm}^{B0} \cdot (1 - f_P^0) \cdot (\eta_B B_{Li} + (1-\eta_B) B_{Ti}) \end{aligned}$$

$$\begin{aligned} E_i^+ &= F_{norm}^{B+} \cdot f_B^+ \cdot (\eta_B B_{Li} + (1-\eta_B) B_{Ti}) \\ &+ F_{norm}^{P+} \cdot (1 - f_B^+) \cdot (\eta_P P_{Li} + (1-\eta_P) P_{Ti}) \end{aligned}$$

$$\begin{aligned} E_i^{CTC} &= F_{norm}^{BCTC} \cdot F_B \cdot \left(\eta_B B_{Li}^{CTC} + (1-\eta_B) B_{Ti}^{CTC}\right) \\ &+ F_{norm}^{PCTC} \cdot (1 - F_B) \cdot \left(\eta_P P_{Li}^{CTC} + (1-\eta_P) P_{Ti}^{CTC}\right) \end{aligned}$$

As before, a set of factors F_{norm} normalize the templates to the data:

$$\begin{aligned} F_{norm}^{P0} &= \frac{\sum_i^{short} (D_i^0 - S_i^0)}{\sum_i^{short} (\eta_P \cdot P_{Li}^{SVX} + (1-\eta_P) \cdot P_{Ti})} \\ F_{norm}^{B0} &= \frac{\sum_i^{short} (D_i^0 - S_i^0)}{\sum_i^{short} (\eta_B \cdot B_{Li}^{SVX} + (1-\eta_B) \cdot B_{Ti})} \\ F_{norm}^{B+} &= \frac{\sum_i^{long} (D_i^+ - S_i^+)}{\sum_i^{long} (\eta_B \cdot B_{Li}^{SVX} + (1-\eta_B) \cdot B_{Ti})} \\ F_{norm}^{P+} &= \frac{\sum_i^{long} (D_i^+ - S_i^+)}{\sum_i^{long} (\eta_P \cdot P_{Li}^{SVX} + (1-\eta_P) \cdot P_{Ti})} \end{aligned}$$

$$F_{norm}^{BCTC} = \frac{\sum_i^{CTC}(D_i^{CTC} - S_i^{CTC})}{\sum_i^{CTC}(\eta_B \cdot B_{Li}^{CTC} + (1-\eta_B) \cdot B_{Ti}^{CTC})}$$
$$F_{norm}^{PCTC} = \frac{\sum_i^{CTC}(D_i^{CTC} - S_i^{CTC})}{\sum_i^{CTC}(\eta_P \cdot P_{Li}^{CTC} + (1-\eta_P) \cdot P_{Ti}^{CTC})}$$

The fit contains two parameters, α_P and α_B. After the fit is performed once, the $P_T^{J/\psi}$ spectra of the Monte Carlo samples are compared with those in the data to ensure that they are in reasonable agreement. They are adjusted to improve the agreement and the fit is redone, resulting in a small change to the fitted polarizations. The adjustment is described fully in Section 4.4.2. The results of the fit are listed in Section 4.5. As an example, Figures 4.9 and 4.10 show the results of the fit in the fourth and sixth P_T bins.

4.3.3 Monte Carlo experiments

The template fitting method has been tested using Monte Carlo experiments. In this procedure, Monte Carlo samples of similar size to the data sample are generated with known polarizations. The fit is then applied to the samples, and the fit results are compared with the known polarizations.

This procedure has been used to test both the inclusive fit and the data analysis fit. In the first case, samples with various values of α $(-1, -0.5, 0, 0.5, 1)$ were generated. This procedure is limited by the large amount of CPU time required to generate the samples. Approximately 80 samples were generated with $\alpha = 0$, and about 40 samples with each of the other four values. The "pull" of a Monte Carlo experiment quantifies how well the fit measured the true value. It is defined as $(\alpha_{fit} - \alpha_{true})/\sigma_{fit}$. The pull distributions were examined in each of the seven P_T bins, for each value of α_{true}. They were found to have means consistent with zero and widths consistent with one, indicating that the template fit is unbiased and yields correct estimates of statistical uncertainty.

The data analysis fit was tested by generating 40 pairs of prompt/B-decay Monte Carlo sample pairs, with $\alpha_P = 0.5$ and $\alpha_B = 0$. A realistic fraction of the prompt and B-decay events were moved between samples to simulate ct smearing. After the data analysis fit had been applied, the pull distributions were examined and again were found to be satisfactory.

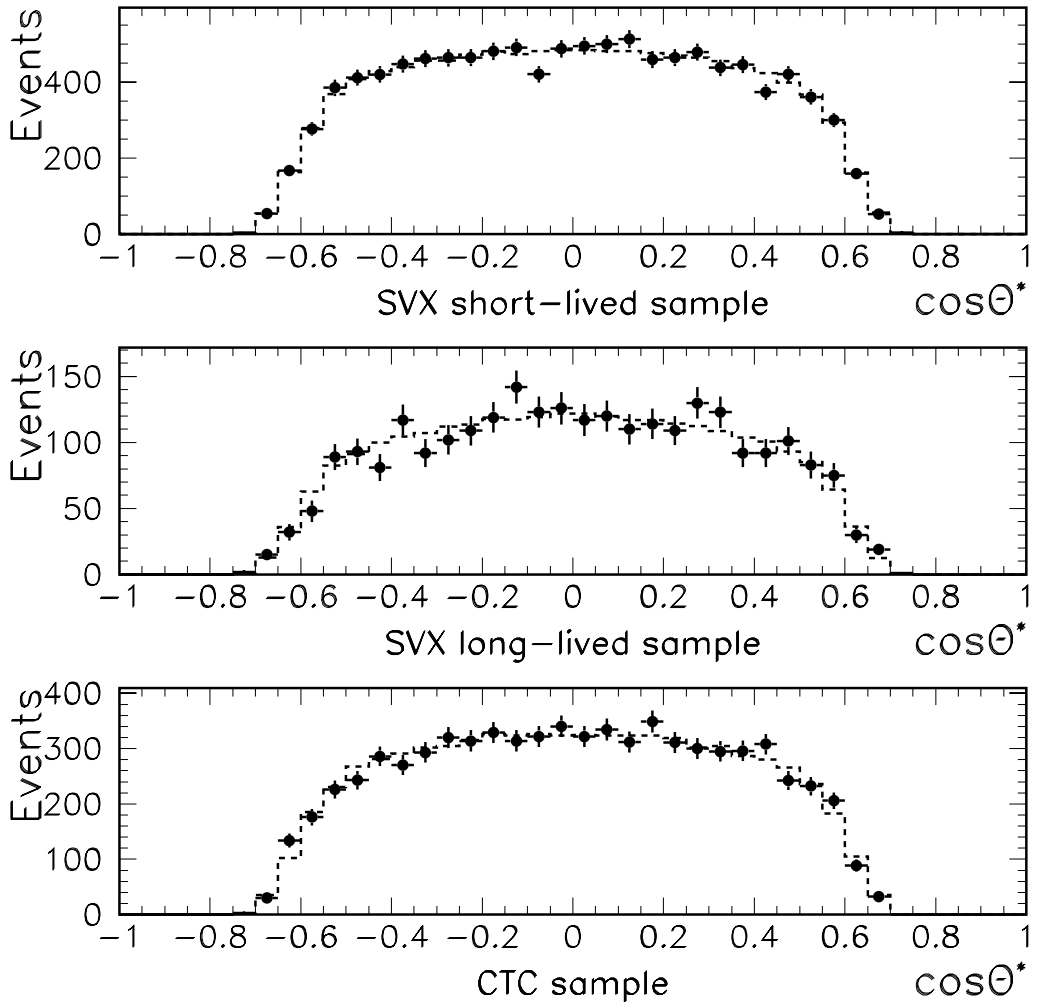


Figure 4.9: The polarization fit in the $8 - 10$ GeV/c bin. Points show the data in the three data subsamples. The data has been sideband-subtracted for ease of viewing. The dashed histograms show the fits, which include contributions of prompt and B-decay, longitudinal and transverse Monte Carlo templates.

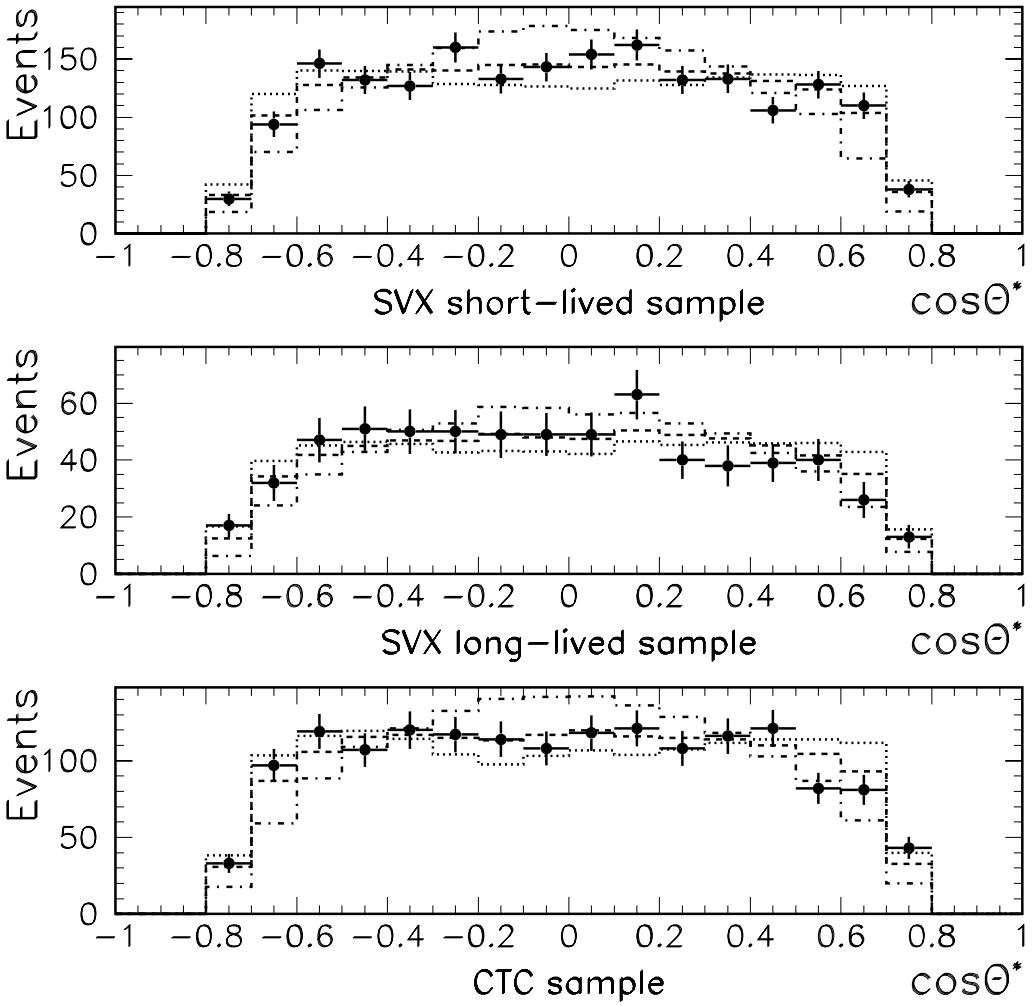


Figure 4.10: The polarization fit in the $12 - 15$ GeV/c bin. The notation is the same as in the previous figure, but the templates are also displayed. The dotted histograms show the normalized transverse templates (i.e. the case where $\alpha_P = \alpha_B = 1$) and the dot-dashed histograms show the longitudinal templates ($\alpha_P = \alpha_B = -1$).

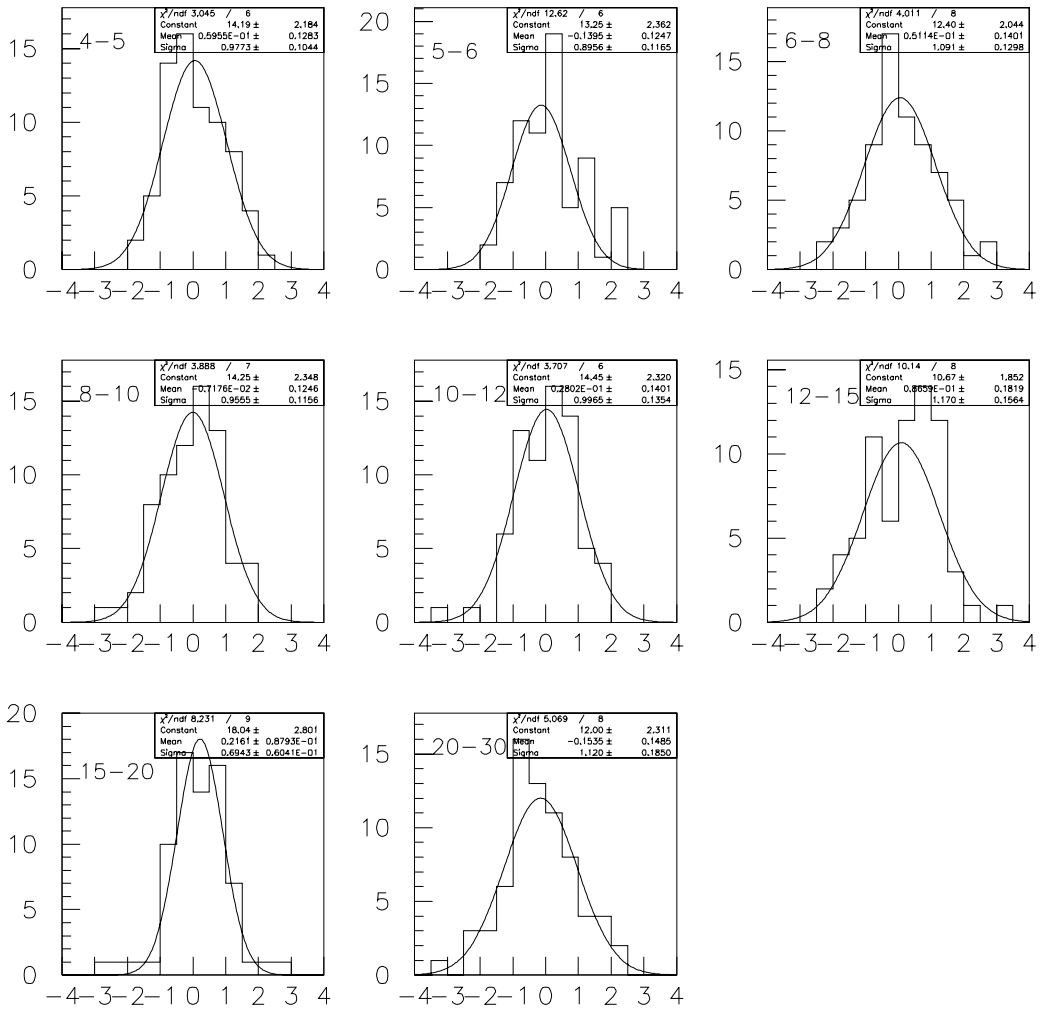


Figure 4.11: Pull distributions in each P_T bin, from inclusive fits in Monte Carlo experiments with $\alpha = 0$. The eighth P_T bin was also analyzed and is included here. Parameters of Gaussian fits to the distributions are included.

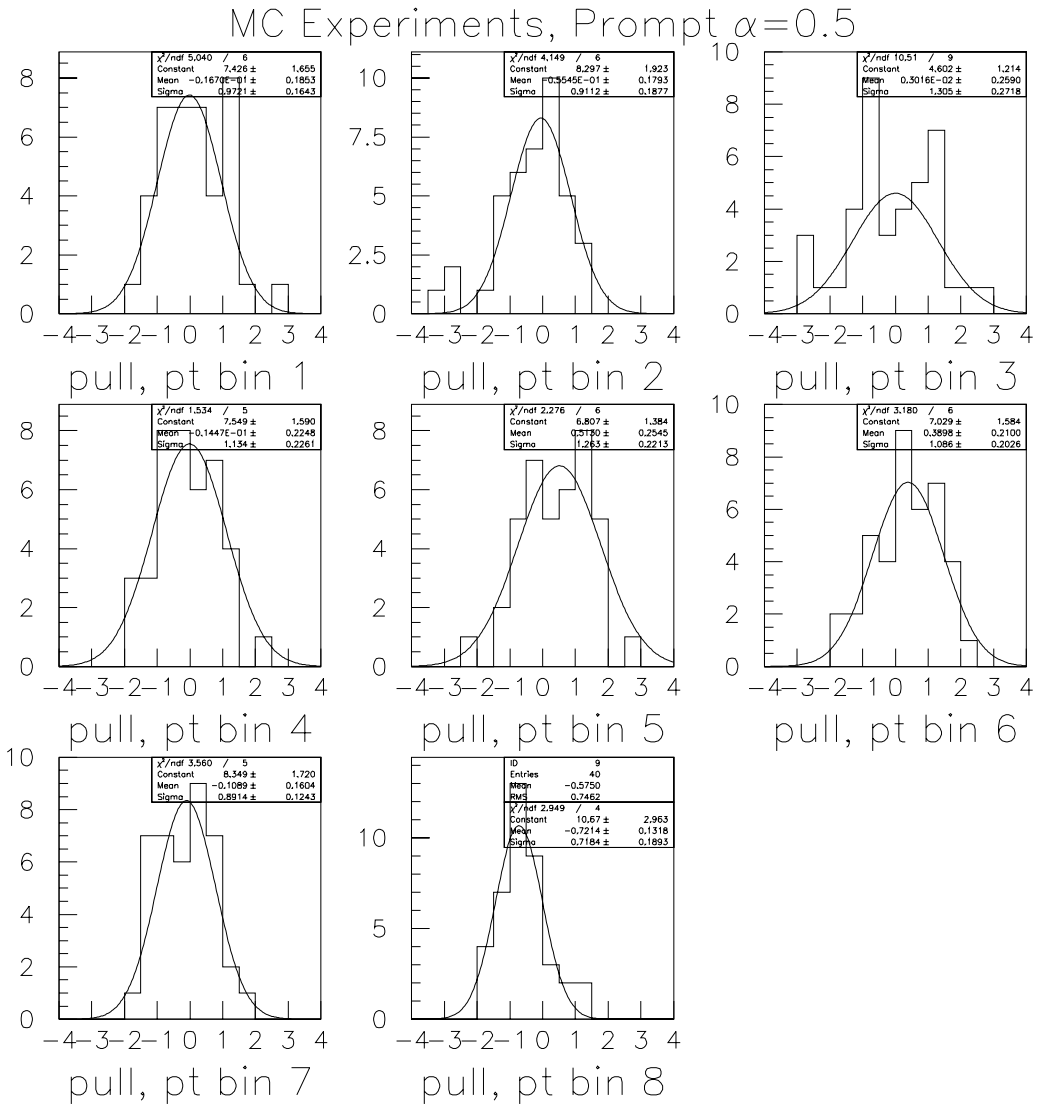


Figure 4.12: Prompt pull distributions from data analysis fits in Monte Carlo experiments with $\alpha_P = 0.5$ and $\alpha_B = 0$. Fit parameters are included.

4.4 Systematic Uncertainties

There are three sources of systematic uncertainty to be evaluated in this analysis. The first originates in the prompt and B-decay fractions used in the polarization fit, which are themselves measured with some uncertainty. The second is due to the $P_T^{J/\psi}$ spectra used in generating the Monte Carlo samples. The third is due to the dimuon trigger efficiency. The evaluation of each uncertainty is described below.

4.4.1 Prompt and B-fractions

The fractions f_p^0, f_B^+ and F_B used in the polarization fit are measured by the ct fit of Section 4.1. To estimate the systematic uncertainty on α_P and α_B due to the fraction measurements, the B-fraction returned from the ct fit is varied by $\pm 1\sigma$, and f_p^0 and f_B^+ are recalculated for each case. The resulting values can all be found in Table 4.3. The polarization fit is then redone with the new values of f_p^0, f_B^+ and F_B, and the resulting changes in α_P and α_B are taken as systematic uncertainties. The shifts in α are listed in Table 4.7.

Varying the other parameters in the ct fit (for example σ, f_{tail} or λ_{tail}) produces significantly smaller variations in the prompt and B-fractions than varying F_B does. Therefore, these variations are not included in the systematic uncertainty. Furthermore, the value of F_{corr}, which was derived from simulation, is not of concern as a systematic uncertainty. This is because F_{corr} simply affects the scale of ct. The polarization fit does not actually depend on the scale of ct: it only requires the relative prompt and B-fractions within the chosen ct regions.

4.4.2 Monte Carlo P_T spectrum

The paramaterization of $d\sigma/dP_T^{J/\psi}$ described in Section 4.2 is in general a good representation of the data. However, the polarization fit results do have some dependence on the Monte Carlo spectrum within each P_T bin, because the acceptance increases over the range of the bin. Therefore, the polarization fit procedure includes a correction to the Monte Carlo P_T

Table 4.7: The effect of B-fraction variation on fitted values of α. Evidently the effect is very small.

$P_T^{J/\psi}$	B-fraction (%)	$\Delta\alpha_P$, raise/lower F_B	$\Delta\alpha_B$, raise/lower F_B
4-5	12.96±0.28	+0.000/-0.000	+0.005/-0.005
5-6	14.84±0.31	+0.000/-0.001	+0.001/-0.001
6-8	18.12±0.29	+0.000/-0.000	+0.001/-0.000
8-10	23.80±0.49	+0.002/-0.001	+0.001/-0.001
10-12	28.87±0.83	+0.002/-0.003	+0.001/-0.002
12-15	32.9±1.2	-0.001/+0.001	+0.002/-0.003
15-20	40.1±1.9	-0.009/+0.009	+0.011/-0.012

Table 4.8: ct requirements used to define high-purity prompt and B-decay samples in SVX data, for the P_T comparison. The requirements vary with $P_T^{J/\psi}$ to maintain $> 95\%$ purity.

Prompt:	$P_T < 12$ GeV/c : $ct < 60$ μm	$P_T > 12$ GeV/c : $ct < 25$ μm
B-decay:	$P_T < 8$ GeV/c : $ct > 270$ μm	$P_T > 8$ GeV/c : $ct > 150$ μm

spectra, based on a comparison with data. The procedure is to fit the polarization, compare and correct the Monte Carlo P_T spectra, and then refit the polarization.

The first polarization fit gives a good estimate of the polarization in each P_T bin. Longitudinal and transvsere Monte Carlo samples can therefore be added with the appropriate weighting, and the Monte Carlo P_T distribution within each P_T bin is histogrammed. This is performed for both prompt and B-decay samples.

In the data, high-purity ($> 95\%$) prompt and B-decay samples are obtained using SVX events with strict ct requirements, listed in Table 4.8. The shape of the P_T spectrum within each P_T bin can then be compared with the Monte Carlo samples. The comparison is quantified by the variable r_{hl}, which is obtained by dividing the histogram of data P_T within a bin by the Monte Carlo histogram. The resulting histogram is fitted to a straight

Table 4.9: Results of comparison between Monte Carlo and data P_T spectra within each P_T bin. $\Delta\alpha_P^{corr}$ and $\Delta\alpha^{corr}$ is the change in α from the uncorrected to the corrected value. $\Delta\alpha^{\delta r_{hl}}$ is the change to α when the r_{hl} is varied by $\pm 1\sigma$.

$P_T^{J/\psi}$	r_{hl}^{Prompt}	r_{hl}^{B}	$\Delta\alpha_P^{corr}$	$\Delta\alpha_B^{corr}$	$\Delta\alpha_P^{\delta r_{hl}}$	$\Delta\alpha_B^{\delta r_{hl}}$
4-5	0.953±0.023	0.940±0.077	+0.034	-0.014	$\mp^{0.009}_{0.010}$	$^{+0.007}_{+0.061}$
5-6	0.991±0.025	0.954±0.073	+0.002	+0.028	$\mp^{0.009}_{0.011}$	$\mp^{0.024}_{0.020}$
6-8	0.953±0.022	0.823±0.054	+0.015	+0.068	∓0.008	$\mp^{0.023}_{0.010}$
8-10	1.042±0.040	0.943±0.073	-0.007	+0.010	$\mp^{0.006}_{0.007}$	$\mp^{0.012}_{0.020}$
10-12	0.932±0.061	1.07±0.12	+0.014	-0.002	$\mp^{0.009}_{0.004}$	$^{+0.006}_{+0.008}$
12-15	1.00±0.10	0.83±0.12	-0.004	+0.030	$\mp^{0.000}_{0.005}$	$\mp^{0.015}_{0.011}$
15-20	0.92±0.17	0.70±0.19	-0.014	+0.081	$^{-0.014}_{-0.031}$	$\mp^{0.058}_{0.027}$

line. The ratio of the line's value at the high end of the bin to its value at the low end is r_{hl}, which is thus equal to one if the spectra agree. If there are too many Monte Carlo events at the higher end of the bin then $r_{hl} < 1$, and conversely for $r_{hl} > 1$. The value of r_{hl} is fitted and the results are listed in Table 4.9.

The values of r_{hl} are then used to modify the Monte Carlo P_T spectra, by discarding Monte Carlo events based on their P_T. In general the agreement is already good, so the values of r_{hl} are close to one and only a small fraction of events are discarded. The modified Monte Carlo samples are then used to refit the data, resulting in a small correction to the values of α. As Table 4.9 shows the result of this correction is small. The fit concludes at this point, as further iterations have negligible effect.

The fit uncertainty on r_{hl} is used to estimate the systematic uncertainty due to the MC P_T spectrum. The polarization fit is redone with r_{hl}^{Prompt} and r_{hl}^{B} independently varied by $\pm 1\sigma$. The resulting changes in α_P and α_B are taken as the systematic uncertainties, and are also listed in Table 4.9. It is worth emphasizing that this systematic uncertainty is really due to the statistical uncertainty on determining the P_T spectrum of the data; the data has limited numbers of events. The original Monte Carlo $P_T^{J/\psi}$ parameterization is not

a significant source of uncertainty because of the correction. Varying the parameterization within reasonable limits has a negligible effect on the fit results.

4.4.3 Trigger efficiency

DIMUTG and MU2TRG use parameterizations of the Level 1 and Level 2 muon trigger efficiencies which are functions of muon P_T. These efficiency curves have been fitted from data, so the curve parameters have uncertainties associated with them. The shape of the efficiency curves has a significant effect on the polarization measurement, since the efficiency falloff at low P_T^μ contributes to the acceptance falloff at large $|\cos\theta^*|$.

To evaluate the systematic uncertainty due to the trigger, the parameters are varied to make the efficiency curves "shallower" or "steeper" with respect to muon P_T. This evaluation is done entirely with simulation. Monte Carlo samples using the steeper and shallower curves are used to fit a Monte Carlo sample of simulated data, and the fitted polarization is compared to the results of fits using the standard curves.

A large Monte Carlo sample is generated, including Run 1A and Run 1B components, using the prompt $P_T^{J/\psi}$ spectrum parameterization. A B-decay sample is not generated as the systematic effect should be the same for both. The simulated data is generated with $\alpha = 0$, to be generally similar to the actual data. Three pairs of Monte Carlo samples are also generated: one with the standard curves, one with steep curves and one with shallow curves.

The simulated data is fitted to each of the three template pairs. The results are summarized in Table 4.10. At low P_T, the shallower curves give higher values of α. The effect disappears at high P_T as expected. The measurement of the systematic shift in α is limited by the statistics of the Monte Carlo samples, so the shifts are fitted to a smooth function of P_T, symmetric for shallow and steep variation. Figure 4.13 shows the fit. The same uncertainty is quoted for α_P and α_B.

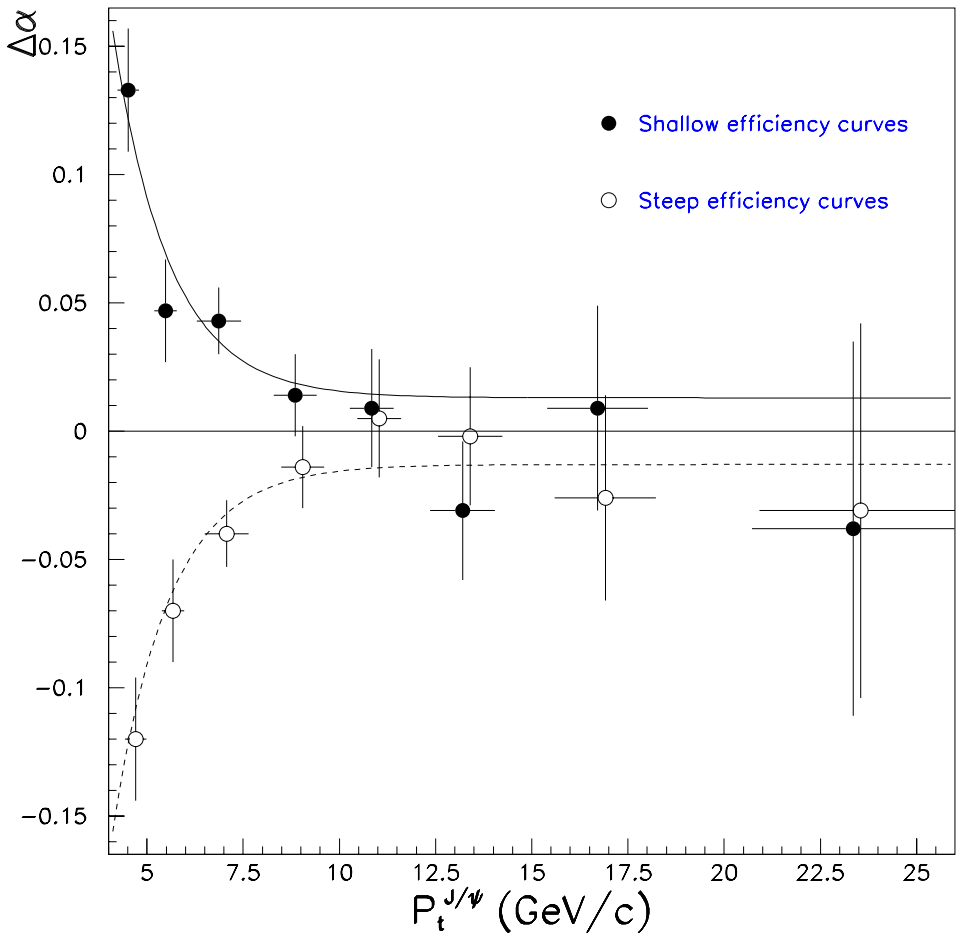


Figure 4.13: The trigger efficiency systematic uncertainty as a function of P_T. Points: shifts in α from shallow and steep variations in each P_T bin. Their uncertainties are taken from the second column of Table 4.10. Curves: a smooth symmetric parameterization, fitted to the points.

Table 4.10: Shifts in α with shallower/steeper trigger simulation efficiency curves. The fitted systematic is taken from the curve in Figure 4.13.

$P_T^{J/\psi}$	α, standard curves	$\Delta\alpha$, shallower curves	$\Delta\alpha$, steeper curves	fitted systematic
4-5	0.045 ± 0.024	+0.133	-0.120	±0.122
5-6	-0.009 ± 0.020	+0.047	-0.070	±0.069
6-8	0.016 ± 0.13	+0.043	-0.040	±0.035
8-10	-0.003 ± 0.016	+0.014	-0.014	±0.018
10-12	0.025 ± 0.023	+0.009	+0.005	±0.014
12-15	-0.039 ± 0.027	-0.031	-0.002	±0.013
15-20	0.026 ± 0.040	+0.009	-0.026	±0.013

4.5 Polarization Fit Results

Table 4.11 lists the fitted polarizations α_P and α_B and their statistical and systematic uncertainties. The fit confidence levels are also shown, and are evidently reasonable. The statistical uncertainties are smallest at intermediate values of P_T. At lower P_T they increase because of the loss of acceptance in $|\cos\theta^*|$. At higher P_T they increase because there are fewer events. The correlation coefficients between α_P and α_B are not large; they vary smoothly from -0.29 in the lowest P_T bin to -0.46 in the highest. This demonstrates that the measurements of α_P and α_B are largely independent, due to the good separation of prompt and B-decay events in the SVX sample.

The systematic uncertainty quoted in Table 4.11 consists of the three systematics described in Section 4.4 added in quadrature. Where the positive and negative systematics differ, they have been averaged. It can be seen that the systematic uncertainties are significantly smaller than the statistical uncertainties, except in the lowest bin where the trigger efficiency uncertainty is significant.

Figure 4.14 shows the measured polarization as a function of J/ψ transverse momen-

Table 4.11: Results of the data analysis polarization fit. The mean P_T column lists the average P_T of all signal events in that bin, and is used in plotting Figure 4.14. Statistical and systematic uncertainties are listed, as well as the polarization fit χ^2 per degrees of freedom and corresponding confidence level.

$P_T^{J/\psi}$ bin (GeV/c)	Mean P_T (GeV/c)	Prompt α	B-decay α	χ^2/d.o.f., C.L.
4-5	4.5	0.30±0.12±0.12	-0.49±0.41±0.13	66/63, 38%
5-6	5.5	0.01±0.10±0.07	-0.18±0.33±0.07	65/68, 57%
6-8	6.9	0.178±0.072±0.036	0.10±0.20±0.04	85/82, 40%
8-10	8.8	0.323±0.094±0.019	-0.06±0.20±0.02	77/87, 77%
10-12	10.8	0.26±0.14±0.02	-0.19±0.23±0.02	71/90, 93%
12-15	13.2	0.11±0.17±0.01	$0.11\pm^{0.31}_{0.28}\pm0.02$	40/46, 71%
15-20	16.7	-0.29±0.23±0.03	$-0.16\pm^{0.38}_{0.33}\pm0.05$	59/51, 20%

tum, as well as an NRQCD prediction for the prompt polarization. Comparisons between theoretical models and the results of this analysis are discussed in the next chapter.

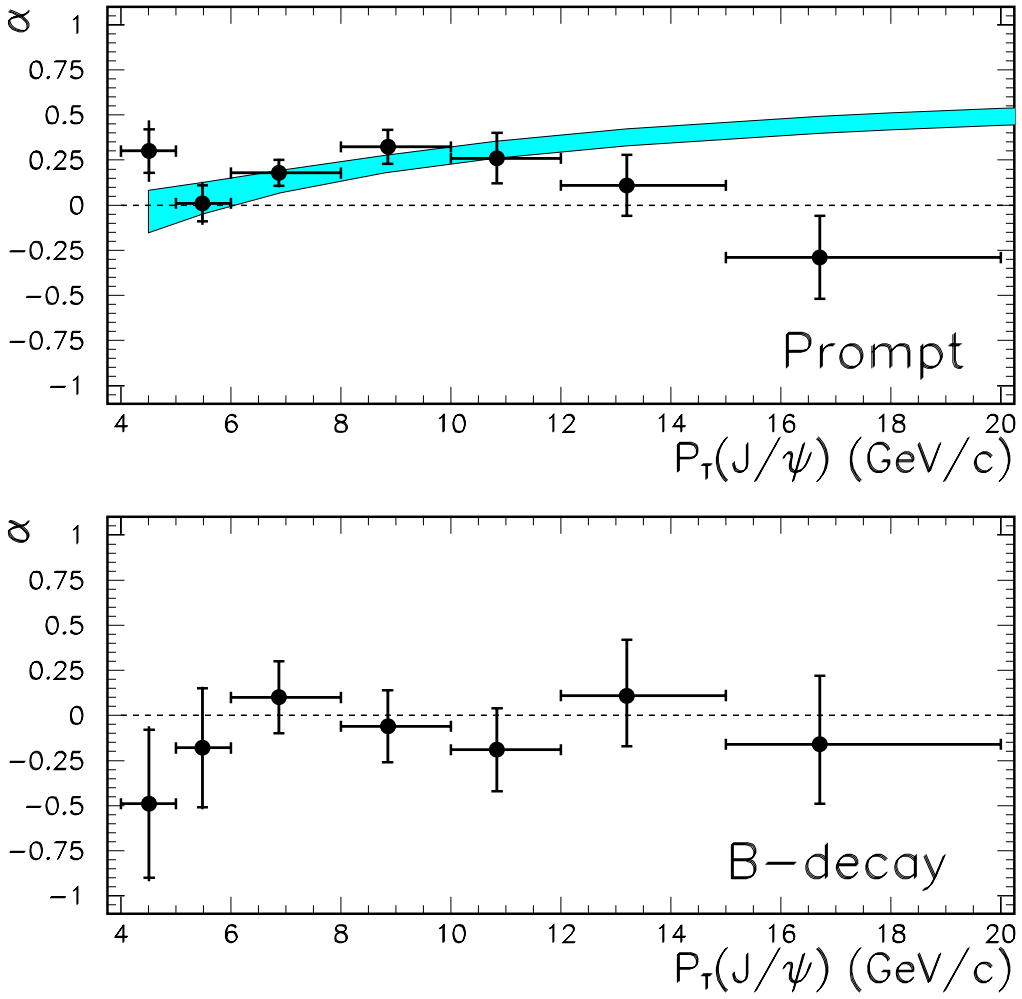


Figure 4.14: Polarization fit results. The ticks on the vertical error bars denote the statistical uncertainty alone; the full vertical error bars include the systematic uncertainty added in quadrature. In many cases the addition of the systematics is too small to be seen. The shaded area shows an NRQCD prediction which takes the feeddown into account [57]; the band represents the theoretical uncertainty.

Chapter 5

Conclusion

The principal results of this analysis are the polarizations of J/ψ mesons produced promptly and in B-decay at the Fermilab Tevatron. These properties are quantified by the polarization parameters α_P and α_B, and are measured over the transverse momentum range $4 - 20$ GeV/c and the rapidity range $|y| < 0.6$. The measured values are summarized in Table 4.11 and Figure 4.14. This chapter discusses these results, compares them with theoretical predictions and considers the future prospects for experimental work in this area.

5.1 Discussion

The prompt polarization is the quantity of real interest so it is considered first. The discussion of B-decay polarization then follows.

5.1.1 Prompt polarization

As Figure 4.14 shows, the measured value of α_P at intermediate P_T is positive, being significantly above zero in the range $6 - 10$ GeV/c . At higher P_T, however, α_P does not increase. In the two bins above 12 GeV/c , it is arguably consistent with zero. Although the statistical uncertainty must be kept in mind, this appears to disagree with predictions based on the NRQCD factorization formalism. The theoretical prediction of α_P [57] shown in Figure 4.14 displays good agreement with the data at the lower values of P_T, but as

with all NRQCD predictions it continues to rise as P_T increases. The data also appear to disagree with the general Color Evaporation Model prediction that α should be zero at all values of P_T.

To discuss the apparent discrepancy between the NRQCD factorization prediction and the data, it is worth outlining the prediction method used in [57]. This prediction includes the effects of χ_c and $\psi(2S)$ feeddown on α_P. (While the feeddown is expected to reduce α_P below the value of α_{direct}, it is very unlikely that this effect is drastic enough to cancel a large value of α_{direct} and reduce α_P to ~ 0 at high P_T.) First, the relevant NRQCD colour octet matrix elements for J/ψ, χ_c and $\psi(2S)$ production are estimated by fitting the P_T spectra previously measured by CDF [50, 51]. Both fusion and fragmentation processes are taken into account in this measurement. The colour singlet matrix elements are derived from the partial widths $\Gamma(\psi \to l^+l^-)$ and $\Gamma(\chi_{c2} \to \gamma\gamma)$. Next, these matrix elements are used to calculate the production cross sections for each J/ψ, χ_c and $\psi(2S)$ helicity state, again including fusion and fragmentation. The probabilities for each χ_c and $\psi(2S)$ helicity state to decay to a longitudinal J/ψ state are simply estimated from quantum mechanical spin rules.

The effective α from feeddown, calculated in this way, varies between about 0.2 and 0.5 over the range of P_T [57]. When combined with the predicted direct α, the result is the curve shown in Figure 4.14. The predominant theoretical uncertainties arise from the fitted values of the matrix elements and the choice of parton distribution function sets[1]. There are also uncertainties in the renormalization and factorization scale, and the charm quark mass. Most NRQCD factorization calculations encounter all of the above theoretical uncertainties.

Within the NRQCD framework, there are some suggestions for effects which could cause α_P to be lower than expected at high P_T. Firstly, contributions to the gluon fragmentation process at higher orders in α_s may reduce the transverse polarization of the resulting $c\bar{c}$ state. For example, the predictions in [43] and [57] treat these higher orders differently, and this produces a difference of around 0.2 between their predicted values of α_{direct}. Secondly,

[1] Leading-order sets are used: MRST98LO as the default, CTEQ5L as a variation.

there may be significant spin-symmetry breaking effects in the evolution of the $c\bar{c}$ pair to a J/ψ meson. Such effects occur at higher orders in v and do not preserve the $c\bar{c}$ spin alignment. Both of these possibilities were mentioned in Section 1.4. Thirdly, and perhaps more profoundly, factorization may be breaking down [57]. Factorization relies on a clear separation between the energy scales of the $c\bar{c}$ production and the binding process. The charm quark mass, which sets the lower limit of the production energy scale, is not much above the nonperturbative regime of QCD, so the production process may simply not be factorizing. These are all open questions being considered by theorists.

Lastly, the CEM and the NRQCD factorization pictures of quarkonium production are not entirely alone. There are models which have recently been proposed to explain the various experimental results on cross sections and polarizations. One approach [124] models the newly created $Q\overline{Q}$ pair as interacting perturbatively with a colour field. The field is created by radiation from the incoming gluons, or, in the case of high P_T production, from the fragmenting gluon. In effect, factorization does not hold in this model. One of its predictions is that directly produced ψ mesons are unpolarized at $P_T \gg m_\psi$. Another approach [125] considers the intrinsic transverse momentum of the incoming partons in the colliding hadrons. It calculates significantly different P_T spectra than the CSM or NRQCD factorization formalism do. This model has been used to explain the cross section for J/ψ production from χ_c decay without invoking colour octet mechanisms, although it has not yet been used for the important calculation of direct ψ cross sections. It has not yet made a polarization prediction, but appears to favour the dominance of colour singlet fragmentation at high P_T, which would probably not produce large polarization. It has also been suggested that initial state gluon radiation by the incoming partons enhances the intrinsic P_T effect [44].

5.1.2 B-decay polarization

The value of α_B measured in this analysis does not carry a great deal of physical significance. While production models can be applied to charmonium production in B-hadron decay [126], the predictions are not directly comparable to α_B. This is because of the way α_B is

defined and measured: it is fitted, like α_P, from the distribution of $\cos\theta^*$, which is defined using the $p\bar{p}$ center-of-mass frame. A proper measurement of the polarization of J/ψ mesons produced in B-hadron decay would require the use of a different angle, i.e. between the μ^+ momentum in the J/ψ rest frame and the J/ψ momentum in the B-hadron rest frame. Such a measurement is not possible in this analysis because the B-hadrons are not fully reconstructed. The full reconstruction of B-hadron decays is not efficient enough to be of practical use in this measurement. CDF has however performed a separate analysis of J/ψ polarization in exclusive B meson decays [127].

If the B-hadrons were at rest in the lab frame, then α_B would be equivalent to the actual polarization of the daughter J/ψ mesons. As it is, the Lorentz boost of the B-hadrons in the lab frame has the effect of "diluting" the value of α_B towards zero. Some simple Monte Carlo simulation has been performed to estimate the magnitude of this dilution. B mesons were generated with a realistic P_T distribution, and the typical decays $B \to J/\psi K^*$ were simulated[2]. The decays were generated isotropically since B mesons are pseudoscalars. Two samples were generated, one in which the produced J/ψ mesons were transversely polarized, and one in which they were longitudinally polarized. The polarized J/ψ mesons were then passed through the detector simulation and reconstruction code, and the value of α_B measured. The transversely polarized sample produced values of α_B between 0.3 and 0.4, depending on $P_T^{J/\psi}$. The longitudinally polarized sample produced values of α_B between -0.4 and -0.5. This illustrates the dilution of α from its generated values of ± 1.

The values of α_B measured in the data are generally consistent with zero, with uncertainties between 0.2 and 0.4. This is a reasonable result, given the dilution. The only experimental value of the actual J/ψ polarization in B-decay has been measured by the CLEO collaboration [128]. It is $\alpha = -0.37 \pm 0.14$, but cannot be compared directly to α_B, because it was only measured in $B \to J/\psi\ K/K^*$, and because of the dilution in α_B.

It has also been considered whether constraining α_B to some reasonable value in the polarization fit would improve the statistical precision on α_P [112]. However, α_B and α_P

[2]There are many other $B \to J/\psi$ decay modes, but this suffices for a simple estimate. Most weakly-decaying B-hadrons produced at the Tevatron are B mesons, with the Λ_b only accounting for $\sim 10\%$.

are not strongly correlated, so the improvement in σ_{α_P} is not large. Given that it would introduce an additional assumption (on α_B), the small improvement is not worthwhile.

5.2 Future Prospects

Because of the apparent disagreement between the predicted and measured values of α_P at large transverse momentum, J/ψ polarization will continue to be an important topic for experimental study. Run 2 of the Tevatron will begin in 2001, with the goal of providing at least 2 fb^{-1} of $p\bar{p}$ collisions at $\sqrt{s} = 2.0$ TeV.

This large data sample should allow for a significantly more precise polarization measurement, which will provide a more stringent test of production models. The CDF dimuon trigger will continue to provide the necessary J/ψ data sample in Run 2, although the muon P_T thresholds may change somewhat [129]. The use of muon detector systems beyond the CMU may allow further increases in the size of the data sample. The CMX is being extended in azimuthal coverage, and the new Intermediate Muon system will provide coverage in the pseudorapidity range $1 < |\eta| < 1.5$. A measurement of the dependence of polarization upon rapidity may therefore be feasible, but there are no theoretical predictions for this at present, and it may not be suitable for discriminating between production models. More importantly, with sufficient statistics the polarization may be measured at high P_T beyond 20 GeV/c .

The polarizations of $\psi(2S)$ and Υ mesons hold the same theoretical interest as that of J/ψ mesons. Measurements have been made using the Run 1 data sample [130, 131] but they are even more statistically limited than the J/ψ analysis, so these too will be a goal for Run 2. Another possible goal is the separation of the direct J/ψ polarization from the effects of feeddown. However, the upgraded CDF detector will be no more suited to measuring low energy photons than the Run 1 detector. The feeddown polarization measurement would require significant study of the $\cos\theta^*$ bias in $\chi_c \to J/\psi\ \gamma$ reconstruction.

Quarkonium production in experimental environments other than hadron colliders will also continue to be of interest. Charmonium production in fixed-target pion-nucleon scat-

tering is one such area of study [132]. Existing data indicates that the ψ mesons produced in πN collisions are unpolarized. However, the feeddown from χ_c mesons is significant, and will have to be separated before the polarization can constitute a test of production models. Another area is high-energy ep collisions produced by the HERA collider at the DESY laboratory in Hamburg. NRQCD predictions, using matrix elements from Tevatron data, appear to disagree with inelastic J/ψ production cross sections measured at HERA, although there are explanations which resolve the discrepancy [46, 47, 133]. The J/ψ angular decay distribution at HERA can also provide a test of production models [132].

To conclude, Run 2 of the Tevatron will provide valuable data, and significantly improved measurements on quarkonium polarization. The increase in statistics will also provide improved cross section measurements and hence a more precise determination of NRQCD matrix elements. Comparing these to matrix element values measured in other experimental environments tests their universality. Between them, the polarization and universality tests may resolve whether NRQCD factorization, or some other theoretical framework, gives the best description of quarkonium physics. This in turn would be a useful step in the ongoing effort towards understanding the strong force.

Appendix A

The J/ψ Angular Decay Distribution

This appendix describes the derivation of the $(1 + \alpha \cos^2 \theta^*)$ form of the J/ψ angular decay distribution. The derivation presented below applies not just to the decay $J/\psi \to \mu^+\mu^-$, but to all parity-conserving vector meson decays to spin-$\frac{1}{2}$ fermion-antifermion pairs. It is based on the analysis in [117], which provides a complete and general discussion of angular distributions in particle decays.

A.1 Derivation

To obtain an appropriate coordinate system for analyzing $J/\psi \to \mu^+\mu^-$ decays at CDF, the relevant independent vectors are:

- the proton momentum $\vec{p}_p$ in the lab frame
- the J/ψ momentum $\vec{p}_{J/\psi}$ in the lab frame
- the μ^+ momentum $\vec{p}_\mu{}^{J/\psi}$ in the J/ψ rest frame

The production plane is defined by the vectors $\vec{p}_p$ and $\vec{p}_{J/\psi}$. For this analysis, the decay coordinate system $(\hat{x}, \hat{y}, \hat{z})$ is then defined by the following conditions:

- $\hat{z}$ lies along $\vec{p}_{J/\psi}$

- $\hat{y}$ is the production plane normal, lying along $\vec{p}_p \times \vec{p}_{J/\psi}$
- $\hat{x}$ completes the right-handed coordinate system: $\hat{x} = \hat{y} \times \hat{z}$

Because $\hat{z}$ lies along $\vec{p}_{J/\psi}$, the directions of these unit vectors do not change under boosts between the lab frame and the J/ψ rest frame. Their lengths can be normalized to unity as necessary.

The angular distribution of the two-body decay in the J/ψ rest frame is then determined by two angles: the polar angle θ^* and the azimuthal angle ϕ^* of the positive muon.

$$\vec{p}_\mu^{\,J/\psi} \;=\; |\vec{p}_\mu^{\,J/\psi}| \;\cdot\; (\sin\theta^* \cos\phi^* \hat{x} \;+\; \sin\theta^* \sin\phi^* \hat{y} \;+\; \cos\theta^* \hat{z}) \tag{A.1}$$

The decay is analyzed in the helicity basis, in which the $\mu^+\,\mu^-$ final state is characterized by the helicities of the muons. The μ^+ and μ^- helicities, λ^+ and λ^-, can each be $+\frac{1}{2}$ or $-\frac{1}{2}$. There are thus four conceivable matrix elements[1] for the decay, $M(\pm\frac{1}{2}, \pm\frac{1}{2})$. Parity conservation forbids the two for which $\lambda^+ = \lambda^-$, and also implies that $M(+\frac{1}{2}, -\frac{1}{2}) = M(-\frac{1}{2}, +\frac{1}{2})$.

The information on the production polarization of the J/ψ mesons is contained in the density matrix ρ:

$$\rho = \begin{pmatrix} \rho_{11} & \rho_{10} & \rho_{1-1} \\ \rho_{01} & \rho_{00} & \rho_{0-1} \\ \rho_{-11} & \rho_{-10} & \rho_{-1-1} \end{pmatrix} \tag{A.2}$$

It is Hermitian and satisfies $\mathrm{Tr}(\rho) \equiv \rho_{11} + \rho_{00} + \rho_{-1-1} = 1$. The longitudinal and transverse polarization fractions are ρ_{00} and $(\rho_{11} + \rho_{-1-1})$ respectively. Since the $\hat{z}$ axis lies in the production plane, parity conservation imposes further constraints on ρ:

$$\begin{aligned} \rho_{-1-1} &= \rho_{11} \\ \rho_{-11} &= \rho_{1-1} \\ \rho_{-10} &= -\rho_{10} \\ \rho_{0-1} &= -\rho_{01} \end{aligned} \tag{A.3}$$

[1] These are not NRQCD matrix elements, and their actual value doesn't matter here.

This reduces the number of independent real parameters in ρ to four. A convenient set is ρ_{00}, ρ_{1-1}, $\mathrm{Re}(\rho_{01})$ and $\mathrm{Im}(\rho_{01})$.

For a given production density matrix, the angular distribution of decays $W(\theta^*, \phi^*)$ is:

$$W(\theta^*, \phi^*) \;=\; N \cdot \sum_{\lambda^+, \lambda^-, m, m'} |M(\lambda^+, \lambda^-)|^2 \; \rho_{mm'} \; D^{j*}_{m\lambda}(\phi^*, \theta^*, 0) \; D^{j}_{m'\lambda}(\phi^*, \theta^*, 0) \qquad \text{(A.4)}$$

Here N is a normalization factor, $\lambda = \lambda^+ - \lambda^-$, $j = 1$ (the J/ψ spin), and the D's are Wigner functions:

$$D^j_{mm'}(\alpha, \beta, \gamma) \;=\; e^{-im\alpha} \; d^j_{mm'}(\beta) \; e^{-im'\gamma} \qquad \text{(A.5)}$$

The d functions are widely used and can be looked up in various sources. They satisfy

$$d^j_{m'm} \;=\; (-1)^{m-m'} d^j_{mm'} \;=\; d^j_{-m-m'} \qquad \text{(A.6)}$$

which allows all the necessary d functions for this calculation to be derived from

$$d^1_{11}(\beta) = \frac{1 + \cos\beta}{2} \qquad d^1_{10}(\beta) = \frac{-\sin\beta}{\sqrt{2}} \qquad d^1_{1-1}(\beta) = \frac{1 - \cos\beta}{2} \qquad \text{(A.7)}$$

Calculating W is then tedious but straightforward algebra; the sum contains 18 terms, encompassing the two possible combinations of (λ^+, λ^-) and the nine possible combinations of (m, m'). The first step is to sum over (λ^+, λ^-) and simplify the Wigner functions:

$$W(\theta^*, \phi^*) \;\propto\; \sum_{m,m'} \; \rho_{mm'} \; e^{i(m-m')\phi^*} \; \Big(d^1_{m1}(\theta^*) \; d^1_{m'1}(\theta^*) \;+\; d^1_{m-1}(\theta^*) \; d^1_{m'-1}(\theta^*) \Big) \qquad \text{(A.8)}$$

Writing out the d functions and substituting out all the redundant elements of ρ, the eventual result is:

$$\begin{aligned} W(\theta^*, \phi^*) \;\propto\; & \tfrac{1+\rho_{00}}{2} \; (1 + \tfrac{1-3\rho_{00}}{1+\rho_{00}} \cos^2\theta^*) \;+\; \rho_{1-1} \; \cos 2\phi^* \; (1 - \cos^2\theta^*) \\ & + \sqrt{2} \; \mathrm{Re}(\rho_{01}) \; \cos\phi^* \; \sin 2\theta^* \end{aligned} \qquad \text{(A.9)}$$

With the change of variable $\alpha = \frac{1-3\rho_{00}}{1+\rho_{00}}$, the first term becomes the familiar expression $\frac{2}{\alpha+3}(1 + \alpha\cos^2\theta^*)$. The other two terms depend on $\cos 2\phi^*$ and $\cos\phi^*$, which both vanish when integrated over ϕ^*. In the polarization analysis, the data and Monte Carlo samples are always integrated over ϕ^* so these two terms are ignored.

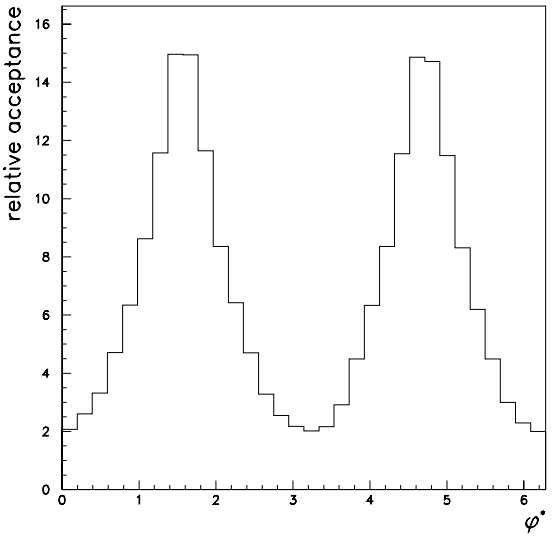


Figure A.1: Relative acceptance versus ϕ^*, over the P_T range $4 - 20$ GeV/c . Calculated using the detector simulation; the vertical scale is arbitrary. This shape is referred to as $a^{\phi}(\phi^*)$ in the text. It flattens out significantly as P_T increases.

A.2 Effect of the $\cos 2\phi^*$ term

However, a check of the $\cos 2\phi^*$ dependence in the data is required. This is because the detector acceptance is not uniform as a function of ϕ^*. As shown in Figure A.1, the acceptance is smaller near $\phi^* = 0$ and $\phi^* = \pi$, and larger near $\phi^* = \pi/2$ and $\phi^* = 3\pi/2$. After being multiplied by this acceptance, the $\cos 2\phi^*$ term in Equation A.9 may no longer integrate to zero. Since the $\cos 2\phi^*$ term also depends on $\cos^2\theta^*$, if ρ_{1-1} is large it may bias the measured value of α. This section presents a confirmation that the effect of the $\cos 2\phi^*$ term in the data is in fact small and can be neglected.

Meanwhile, the third term in Equation A.9 depends on $\cos\phi^*$. Due to the symmetric shape of the acceptance, this term will still vanish upon being multiplied by the acceptance and integrated, so it can be ignored regardless of the size of $\mathrm{Re}(\rho_{01})$.

To estimate the effect of the $\cos 2\phi^*$ term on the measured value of α in a simple fashion, two steps are presented below. First, a method of measuring ρ_{1-1} in the data is described.

Then, for a given value of ρ_{1-1}, the size of the resulting shift in α is calculated.

A.2.1 Measuring ρ_{1-1}

In this analysis, the observed quantity is the angular distribution of the data, D, which is the product of the true distribution W and the angular acceptance A. All three quantities depend on θ^* and ϕ^*:

$$D(\theta^*, \phi^*) \;\propto\; W(\theta^*, \phi^*) \cdot A(\theta^*, \phi^*) \tag{A.10}$$

The size of ρ_{1-1} can be estimated by measuring the $\cos 2\phi^*$ dependence of the data distribution. The above equation is integrated over $\cos\theta^*$, and the data distribution is divided by the acceptance:

$$\begin{aligned} \frac{\int_{-1}^{+1} D(\theta^*,\phi^*)\; d\cos\theta^*}{a^\phi(\phi^*)} \;\propto\; & \tfrac{2}{\alpha+3} \int_{-1}^{+1} (1+\alpha\cos^2\theta^*)\; a^\theta(\theta^*)\; d\cos\theta^* \\ & + \rho_{1-1} \int_{-1}^{+1} (1-\cos^2\theta^*)\; a^\theta(\theta^*)\; d\cos\theta^*\; \cos 2\phi^* \\ & + \sqrt{2}\,\mathrm{Re}(\rho_{01}) \int_{-1}^{+1} \sin 2\theta^*\; a^\theta(\theta^*)\; d\cos\theta^*\; \cos\phi^* \end{aligned} \tag{A.11}$$

This takes advantage of the fact, checked in detector simulation, that A factors into separate θ^* and ϕ^* parts:

$$A(\theta^*, \phi^*) = a^\theta(\theta^*) \cdot a^\phi(\phi^*) \tag{A.12}$$

So, if a histogram of ϕ^* in the data is divided by an acceptance histogram from a Monte Carlo sample, the resulting histogram can simply be fitted to a normalized ϕ^*-dependent function:

$$D(\phi^*)/a^\phi(\phi^*) \;=\; N \cdot (1 + F\cos 2\phi^* + G\cos\phi^*) \tag{A.13}$$

The fit yields N, F and G, each with statistical uncertainties. By defining

$$R = \frac{\int_{-1}^{+1} (1-\cos^2\theta^*)\; a^\theta(\theta^*)\; d\cos\theta^*}{\int_{-1}^{+1} (1+\alpha\cos^2\theta^*)\; a^\theta(\theta^*)\; d\cos\theta^*} \tag{A.14}$$

the fitted value of F is simply related to ρ_{1-1} by:

$$F = \rho_{1-1} \cdot R \cdot (\alpha+3)/2 \tag{A.15}$$

R can be estimated from Monte Carlo simulation. This relation will be used below, after a few more equations.

A.2.2 Shift in α

The polarization analysis fit considers only the θ^* dependence of the distributions. In effect, the analysis fit integrates over ϕ^* and then divides D by A to recover W. The resulting quantity looks like:

$$\begin{aligned}\frac{\int_0^{2\pi} D(\theta^*,\phi^*)\ d\phi^*}{a^\theta(\theta^*)} \quad &\propto \quad \int_0^{2\pi} a^\phi(\phi^*)\ d\phi^*\ \tfrac{2}{\alpha+3}\ (1+\alpha\cos^2\theta^*) \\ &+\ \int_0^{2\pi} a^\phi(\phi^*)\cos 2\phi^*\ d\phi^*\ \rho_{1-1}\ (1-\cos^2\theta^*)\end{aligned} \tag{A.16}$$

As mentioned previously, the third term in W, which depends on $\cos\phi^*$, is not present in Equation A.16 because $\int_0^{2\pi} a^\phi(\phi^*)\cos\phi^* d\phi^*$ vanishes.

Denoting the true value of the polarization parameter as α and the measured value as α_m, let the difference between the two (due to the $\cos 2\phi^*$ term) be called $\Delta\alpha$:

$$\alpha_m \ \equiv\ \alpha + \Delta\alpha \tag{A.17}$$

In effect, the measured value of α is obtained from the relative size of the $\cos^2\theta^*$-dependent and $\cos^2\theta^*$-independent terms in Equation A.16:

$$\alpha_m \ =\ \frac{\int a^\phi d\phi^*\ \frac{2}{\alpha+3}\ \alpha\ -\ \int a^\phi \cos 2\phi^* d\phi^*\ \rho_{1-1}}{\int a^\phi d\phi^*\ \frac{2}{\alpha+3}\ +\ \int a^\phi \cos 2\phi^* d\phi^*\ \rho_{1-1}} \tag{A.18}$$

For $\rho_{1-1} \ll 1$, and defining

$$q = \frac{\int_0^{2\pi} a^\phi(\phi^*)\ \cos 2\phi^*\ d\phi^*}{\int_0^{2\pi} a^\phi(\phi^*)\ d\phi^*} \tag{A.19}$$

the result is:

$$\Delta\alpha = -q\cdot\rho_{1-1}\cdot(\alpha+3)/2 \tag{A.20}$$

Combining this with Equation A.15 gives the desired result at last:

$$\Delta\alpha = -q\cdot F/R \tag{A.21}$$

A.2.3 Results

The magnitude of $\Delta\alpha$ has been estimated in each P_T bin, using Equation A.21. F is fitted from data[2], while q and R are both calculated from Monte Carlo simulation. R has a

[2]The fit yields G as well, which also turns out to be small.

Table A.1: Estimated values of q and R, fitted values of F and derived $\Delta\alpha$ for prompt production.

$P_T^{J/\psi}$ (GeV/c)	q	$R(\alpha)$	F	$\Delta\alpha_P$
4-5	-0.69	0.95	0.058 ± 0.020	0.042 ± 0.015
5-6	-0.51	0.94	0.030 ± 0.016	0.016 ± 0.009
6-8	-0.34	0.91	0.007 ± 0.012	0.003 ± 0.004
8-10	-0.24	0.86	-0.007 ± 0.019	-0.002 ± 0.005
10-12	-0.21	0.82	-0.051 ± 0.033	-0.013 ± 0.008
12-15	-0.21	0.82	0.035 ± 0.048	0.009 ± 0.012
15-20	-0.25	0.87	-0.180 ± 0.094	-0.052 ± 0.027

small dependence on α which is corrected for separately in each bin. This estimate is only applied to prompt data, because α_P is the primary quantity of interest. (And also because the value of ϕ^* measured for J/ψ mesons from B-decay, like θ^*, is not the correct value to use in calculated angular distributions.)

Table A.1 lists the results. The statistical uncertainty on F dominates the uncertainty on $\Delta\alpha$, so uncertainties on q and R are not listed. It is clear that this effect is small, comparable to other systematic uncertainties and far smaller than the statistical uncertainties. Thus it is not included in the data analysis fit. Because $\Delta\alpha$ changes sign and takes on several values consistent with zero, it is not included as a systematic uncertainty. If the analysis were to be repeated in the future with a much larger data sample and consequently much smaller statistical uncertainties, this effect should probably be taken into account.

Appendix B

SVXII/ISL Service Work

This Appendix briefly describes the silicon tracking system for the CDFII upgrade, and the service work I did testing SVXII and ISL ladders.

B.1 The CDFII Upgrade

The next run of the Tevatron, Run 2, is scheduled to begin in spring of 2001. Its purpose is to collect a much larger number of $p\bar{p}$ collisions, at least 2 fb^{-1}, than was collected during Run 1. With a larger data sample, the precision of many existing measurements can be improved, for example the CP-violation parameter $\sin(2\beta)$. There is also a better opportunity for discovering "new physics" such as supersymmetry or the Higgs boson.

The CDF and D0 detectors have been extensively upgraded in preparation for Run 2. As well as a new data acquisition system, CDFII has new forward calorimeters and tracking systems [129]. The tracking system consists of the Central Outer Tracker (a drift chamber to replace the CTC) and the SVXII and ISL silicon detectors. SVXII and ISL (Intermediate Silicon Layers) are more extensive detectors than SVX. They will perform the same precision tracking and vertex measurements as SVX did, which are vital for heavy quark physics. In addition, they will:

- make 3-dimensional measurements, allowing precise z-vertex measurements
- extend the coverage along the beamline from ± 25 cm to ± 45 cm

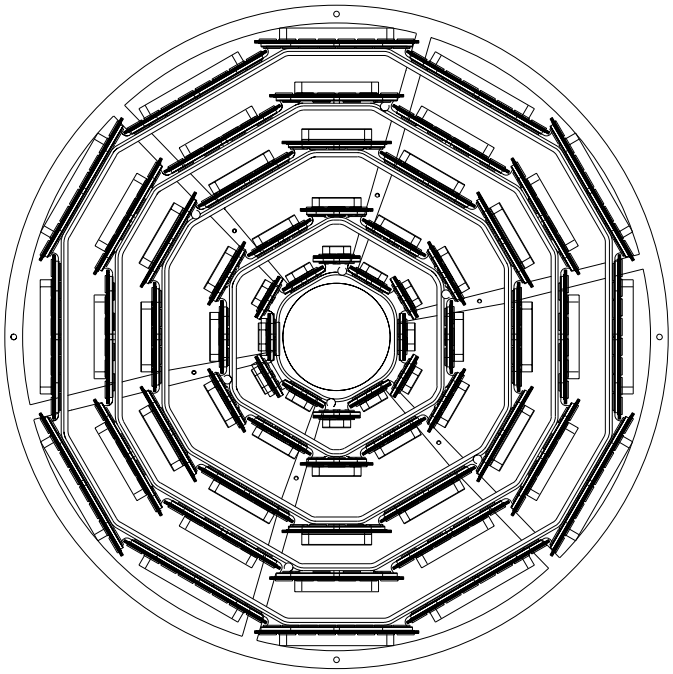


Figure B.1: An end-view of an SVXII barrel, showing the five layers of silicon ladders mounted on the bulkhead.

- provide standalone 3-dimensional tracking in the forward regions $1 < |\eta| < 2$ where the COT coverage is limited
- provide information to the Silicon Vertex Tracker (SVT), a Level 2 displaced-vertex trigger

The layout of SVXII is generally similar to that of SVX, but is extended in many respects. It consists of five concentric layers of silicon ladders, at radii from 2.5 cm to 10.6 cm from the beamline. Figure B.1 shows the positioning of the ladders. Each layer is double sided, providing $r - \phi$ measurements on the junction side and either $r - z$ or small angle stereo measurements on the ohmic side. SVXII consists of three barrels, each 30 cm long and read out at both ends. The total number of channels is approximately 406,000, almost ten times as many as in SVX. A sixth layer of single-sided high-voltage silicon will also be mounted directly on the beampipe at 1.6 cm from the beamline [134].

The ISL detector consists of silicon layers in the radial range $\sim 20 - 30$ cm, the region

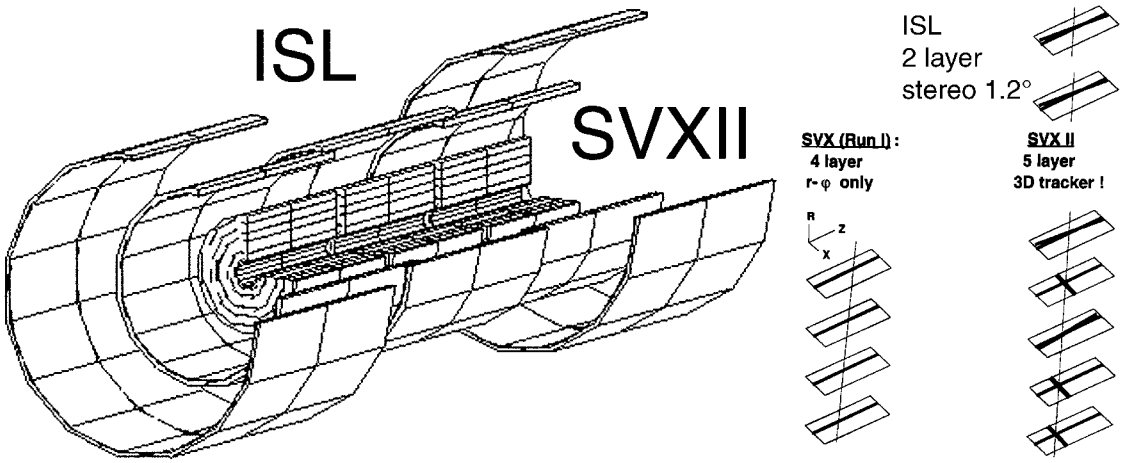


Figure B.2: A isometric view of the layout of SVXII and ISL. At the right a series of diagrams compares the tracking measurements made by SVXII+ISL to those made by SVX. From [135].

formerly occupied by the VTX. The ISL ladders are also double sided, with $r - \phi$ strips on one side and small-angle stereo strips on the other. The data acquisition system is the same for SVXII and ISL, except that the silicon vertex track trigger (SVT) only uses information from SVXII. Figure B.2 gives a schematic view of ISL surrounding SVXII.

The readout chips (called SVX3, revision D) are mounted on hybrid readout circuits. In SVXII, there are hybrids at both ends of the ladder, and there is one hybrid on each side of the ladder, mounted directly on the sensor. The two halves of the ladder are mechanically joined but electrically independent. In ISL the hybrid is not on top of the silicon, because space is not so limited. As in SVX, the hybrids connect the silicon detectors to the outside world, through a series of components which will not be described here.

B.2 SVXII/ISL Production and Testing

There are many steps in the production and testing of SVXII and ISL devices. Various steps are carried out at several CDF institutions in the United States, Europe and Japan. A large part of the process, including the final assembly of the barrels, is done at Fermilab in the Silicon Detector Facility (SiDet).

The series of events in the production of a ladder is as follows. The silicon sensors are produced by two companies, Micron Semiconductor of the U.K. and Hamamatsu Photonics of Japan. The companies perform some quality testing on the sensors, but more thorough testing is then performed at CDF institutions, and each sensor is assigned a quality grade. The SVX3 chips are manufactured by Honeywell; wafers are delivered to Lawrence Berkeley National Laboratory (LBL) for testing and dicing. Good quality chips are mounted on readout hybrids by a contractor, then LBL performs extensive testing on the completed hybrids. The SVX3 chip [136] is significantly more complex than the SVX chip of Run 1; the LBL testing includes complete characterization of each chip on the hybrid as well as a ~ 72 hour burn-in.

The tested and graded hybrids are then sent to Fermilab. Their performance is checked on arrival in case of damage during shipping. The wirebonds are the most fragile component; precautions must also be taken against electrostatic discharge damage. SVXII quarter ladders are then assembled from sensors and hybrids of acceptable quality. One ladder contains four sensors and four hybrids in total. A quarter ladder is the end of a ladder: one sensor with two hybrids attached. The quarter-ladder assembly step involves gluing the hybrids onto the sensor, wirebonding the readout strips to the chips and wirebonding the hybrids together via a jumper piece. It is one of the more stressful steps in the process for the components. Quarter ladders are then tested for readout capability and sensor damage and are burned in for ~ 72 hours. After any necessary repairs, quarter ladders are combined with additional sensors to form full ladders, and the same tests are repeated on the full ladder. A similar procedure applies for ISL assembly [137], the difference being that the production step after the ISL hybrid is the ISL half ladder.

At SiDet there are three systems used in the above testing of hybrids and ladders. The test DAQ system is a reproduction of the actual Run 2 silicon DAQ system, and uses the same VME modules. It provides the most realistic test of the final performance of the device. The Tstand system is also a VME-module based system, but is simpler and is designed specifically for testing. It is used for a variety of measurements, such as noise, leakage current, depletion voltage, and for finding dead or noisy channels and pinholes

(which will be explained shortly). It also includes an infrared laser which may be scanned across a ladder to measure the sensor's response to charge injection. Finally, the burn-in system is a PC-based system used to read out ladders during burn-in. (A version of the burn-in readout system is also used for some of the tests for ISL devices which are done on the Tstand system for SVXII devices.) This is the system with which I was involved, so it is described in some detail below.

B.3 The Burn-In System

The purpose of the burn-in system is to operate the ladders for an extended period of time under realistic conditions. This means that the ladders are cooled, the sensors are biased and the chips are read out. As well as confirming the long-term reliability of all the components in each ladder, this procedure identifies a particular type of sensor damage known as a pinhole.

A pinhole is a short through the coupling capacitor between the implant region and the aluminum readout strip. This is illustrated in Figure B.3. Pinholes may be present in a newly manufactured sensor, they may be a result of damage during wirebonding, or they may appear after the sensor has been biased for some time, when a weak capacitor fails. Since the bias voltage (tens of volts) is applied to the implants, and the SVX3 preamplifiers are operated near ground, a pinhole results in a large flow of current into the preamplifier. It can exceed the normal leakage current by several orders of magnitude. This of course has undesirable effects. The preamplifier channel with the pinhole saturates, and the current is usually high enough to spread to adjacent channels, significantly increasing their noise. Some pinholes draws enough current to reach the limit of the bias voltage supply, in which case the bias voltage to the whole half ladder sags. Pinholes on the ohmic side of the sensor in particular may make the sensor impossible to deplete [139].

Since the coupling capacitors are stressed during the burn-in, pinholes which would otherwise appear during Run 2 can be identified and removed. The channel with the pinhole is easily identified as it has very low noise and its neighbours have above-average

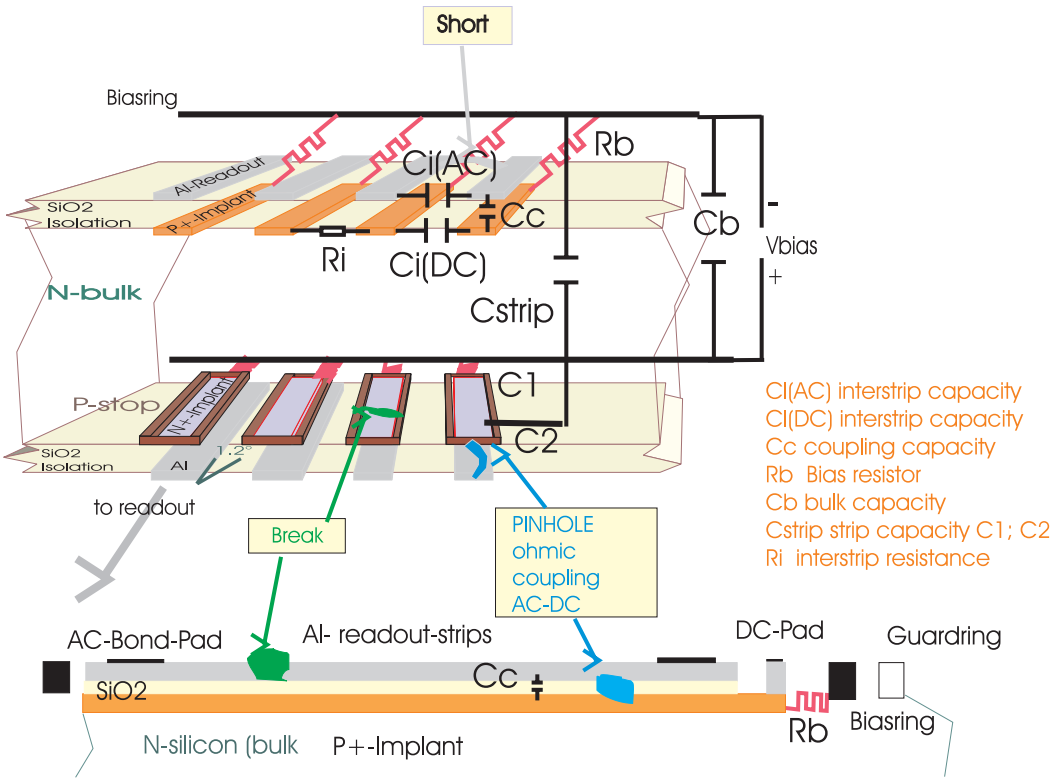


Figure B.3: Schematic of a small-angle stereo sensor (the n-side strips are angled at 1.2° with respect to the p-side strips) from [138]. Three types of damage are illustrated. A pinhole is shown on the ohmic (n) side, shorting the implant strip to the readout strip. Also shown are a break in an n-side implant and a short between two p-side readout strips.

noise. The wirebond from the readout strip to the chip is then removed, which sacrifices that channel but recovers the adjacent channels. Pinholes are most likely to appear within the first few hours of burn-in, so the burn-in runs are ~ 72 hours long.

The SVX3 chips are controlled and read out by a specially built PC-based data acquisition system [140]. It is designed so that many ladders may tested simultaneously; the construction schedule requires up to 20-30 ladders to be burned in per week during peak production. Therefore the burn-in system is highly multiplexed. The PC controls up to eight MUX/FIFO boards. Each MUX/FIFO board can control up to five devices: hybrids, SVXII quarter ladders or ISL half ladders. An SVXII full ladder is equivalent to two quarter ladders in terms of readout. The PC generates control patterns for the chips, which step them through the sequence of initializing, acquiring data, digitizing it and reading out. Asynchronous FIFO circuits on the MUX/FIFO board are used to store these patterns at the relatively slow speed of the PC I/O cards. The patterns are then sent from the pattern FIFO's to the chips at their full operating speed of 50 MHz. The data returned from the chips is read into a pair of readout FIFO's which are arranged in a "ping-pong" setup. The two FIFO's take turns, reading alternate words from the chips. The ping-pong patch was added to the MUX/FIFO board to allow ladders to be read out reliably at the full speed of 50 MHz. The readout FIFO's are read out by the PC and the data is stored on disk for analysis.

The MUX/FIFO board multiplexes the control patterns to all five attached devices. Between the board and each hybrid are a scrambler board, a 64-pin twisted-pair cable, an adapter board and the hybrid HDI cable. These parts are required to transmit good quality high-speed signals over the distance from the MUX/FIFO board to the hybrid. Some of the signal levels are differential and the rest are CMOS. The length of the cables, about 50 cm, is necessary because the hybrids and ladders under test are all located inside cooling boxes. Chip power and bias voltage are also connected through the scrambler board.

The burn-in cooling system [141] consists of four cooling boxes, each of which can hold ten SVXII quarter ladders, or 5 SVXII full ladders or ISL half ladders. Each SVX3 chip generates up to 400 mW of heat, so a cooling system is essential. The boxes are

metal with exterior foam insulation and have cooling channels in the base, through which a chilled water/glycol mixture flows at about 0°C. Nitrogen gas is flushed though the boxes to prevent condensation on the devices. A system of interlocks monitors the temperature and nitrogen flow inside each box, and shuts down the power if their values are outside acceptable bounds.

The data returned from the chips consists of pedestals for every channel. All the chips are operated continuously through the acquire/digitize/readout cycle, but data is only read out by the PC at fixed intervals, typically fifty events every five minutes. An online display of the pedestals and noise is available, as are the leakage currents as measured by the bias voltage supplies. This information allows pinholes to be spotted soon after they form. An offline pinhole-finding program may also be used to analyze data saved on disk for pinholes, leakage current and channels with large noise.

Working with several CDF colleagues from Rutgers University, I was involved in many aspects of the burn-in system. These included the development and implementation of the ping-pong patch, debugging the MUX/FIFO boards and PC software, developing the temperature monitoring system, writing the pinhole-finding program, designing and building active adapter boards and operating the system during the first stages of ladder production.

At the time of writing, ladder production is fully underway. SVXII will contain 180 full ladders, ISL will contain 150, and about 25% spares will also be built. Each one will be fully tested and graded, with the best devices being chosen for the detector. The burn-in system itself has been extensively tested and debugged over the past eighteen months and is currently in continuous use. As of the middle of June, a majority of the SVXII full ladders and roughly half of the ISL half ladders have been burned in. Including quarter ladders, over two hundred pinholes have been identified and fixed on SVXII devices. Less than ten pinholes have been found on ISL ladders, although fewer channels have been burned in. A partially filled SVXII barrel is ready for a CDF/Tevatron commisioning run in August, and the whole silicon upgrade is on schedule to be ready for Run 2 next spring.

Appendix C

The CDF Run I Collaboration

Building and running a state of the art collider detector takes a lot of people. The current CDF Run 1 author list, as of April 2000, is:

T. Affolder,[21] H. Akimoto,[43] A. Akopian,[36] M. G. Albrow,[10] P. Amaral,[7] S. R. Amendolia,[32] D. Amidei,[24] K. Anikeev,[22] J. Antos,[1] G. Apollinari,[10] T. Arisawa,[43] T. Asakawa,[41] W. Ashmanskas,[7] M. Atac,[10] F. Azfar,[29] P. Azzi-Bacchetta,[30] N. Bacchetta,[30] M. W. Bailey,[26] S. Bailey,[14] P. de Barbaro,[35] A. Barbaro-Galtieri,[21] V. E. Barnes,[34] B. A. Barnett,[17] M. Barone,[12] G. Bauer,[22] F. Bedeschi,[32] S. Belforte,[40] G. Bellettini,[32] J. Bellinger,[44] D. Benjamin,[9] J. Bensinger,[4] A. Beretvas,[10] J. P. Berge,[10] J. Berryhill,[7] B. Bevensee,[31] A. Bhatti,[36] M. Binkley,[10] D. Bisello,[30] R. E. Blair,[2] C. Blocker,[4] K. Bloom,[24] B. Blumenfeld,[17] S. R. Blusk,[35] A. Bocci,[32] A. Bodek,[35] W. Bokhari,[31] G. Bolla,[34] Y. Bonushkin,[5] D. Bortoletto,[34] J. Boudreau,[33] A. Brandl,[26] S. van den Brink,[17] C. Bromberg,[25] M. Brozovic,[9] N. Bruner,[26] E. Buckley-Geer,[10] J. Budagov,[8] H. S. Budd,[35] K. Burkett,[14] G. Busetto,[30] A. Byon-Wagner,[10] K. L. Byrum,[2] P. Calafiura,[21] M. Campbell,[24] W. Carithers,[21] J. Carlson,[24] D. Carlsmith,[44] J. Cassada,[35] A. Castro,[30] D. Cauz,[40] A. Cerri,[32] A. W. Chan,[1] P. S. Chang,[1] P. T. Chang,[1] J. Chapman,[24] C. Chen,[31] Y. C. Chen,[1] M. -T. Cheng,[1] M. Chertok,[38] G. Chiarelli,[32] I. Chirikov-Zorin,[8] G. Chlachidze,[8] F. Chlebana,[10] L. Christofek,[16] M. L. Chu,[1] C. I. Ciobanu,[27] A. G. Clark,[13] A. Connolly,[21] J. Conway,[37] J. Cooper,[10] M. Cordelli,[12] J. Cranshaw,[39] D. Cronin-

Hennessy,[9] R. Cropp,[23] R. Culbertson,[7] D. Dagenhart,[42] F. DeJongh,[10] S. Dell'Agnello,[12] M. Dell'Orso,[32] R. Demina,[10] L. Demortier,[36] M. Deninno,[3] P. F. Derwent,[10] T. Devlin,[37] J. R. Dittmann,[10] S. Donati,[32] J. Done,[38] T. Dorigo,[14] N. Eddy,[16] K. Einsweiler,[21] J. E. Elias,[10] E. Engels, Jr.,[33] W. Erdmann,[10] D. Errede,[16] S. Errede,[16] Q. Fan,[35] R. G. Feild,[45] C. Ferretti,[32] R. D. Field,[11] I. Fiori,[3] B. Flaugher,[10] G. W. Foster,[10] M. Franklin,[14] J. Freeman,[10] J. Friedman,[22] Y. Fukui,[20] I. Furic,[22] S. Galeotti,[32] M. Gallinaro,[36] T. Gao,[31] M. Garcia-Sciveres,[21] A. F. Garfinkel,[34] P. Gatti,[30] C. Gay,[45] S. Geer,[10] D. W. Gerdes,[24] P. Giannetti,[32] P. Giromini,[12] V. Glagolev,[8] M. Gold,[26] J. Goldstein,[10] A. Gordon,[14] A. T. Goshaw,[9] Y. Gotra,[33] K. Goulianos,[36] C. Green,[34] L. Groer,[37] C. Grosso-Pilcher,[7] M. Guenther,[34] G. Guillian,[24] J. Guimaraes da Costa,[14] R. S. Guo,[1] R. M. Haas,[11] C. Haber,[21] E. Hafen,[22] S. R. Hahn,[10] C. Hall,[14] T. Handa,[15] R. Handler,[44] W. Hao,[39] F. Happacher,[12] K. Hara,[41] A. D. Hardman,[34] R. M. Harris,[10] F. Hartmann,[18] K. Hatakeyama,[36] J. Hauser,[5] J. Heinrich,[31] A. Heiss,[18] M. Herndon,[17] B. Hinrichsen,[23] K. D. Hoffman,[34] C. Holck,[31] R. Hollebeek,[31] L. Holloway,[16] R. Hughes,[27] J. Huston,[25] J. Huth,[14] H. Ikeda,[41] J. Incandela,[10] G. Introzzi,[32] J. Iwai,[43] Y. Iwata,[15] E. James,[24] H. Jensen,[10] M. Jones,[31] U. Joshi,[10] H. Kambara,[13] T. Kamon,[38] T. Kaneko,[41] K. Karr,[42] H. Kasha,[45] Y. Kato,[28] T. A. Keaffaber,[34] K. Kelley,[22] M. Kelly,[24] R. D. Kennedy,[10] R. Kephart,[10] D. Khazins,[9] T. Kikuchi,[41] B. Kilminster,[35] M. Kirby,[9] M. Kirk,[4] B. J. Kim,[19] D. H. Kim,[19] H. S. Kim,[16] M. J. Kim,[19] S. H. Kim,[41] Y. K. Kim,[21] L. Kirsch,[4] S. Klimenko,[11] P. Koehn,[27] A. Köngeter,[18] K. Kondo,[43] J. Konigsberg,[11] K. Kordas,[23] A. Korn,[22] A. Korytov,[11] E. Kovacs,[2] J. Kroll,[31] M. Kruse,[35] S. E. Kuhlmann,[2] K. Kurino,[15] T. Kuwabara,[41] A. T. Laasanen,[34] N. Lai,[7] S. Lami,[36] S. Lammel,[10] J. I. Lamoureux,[4] M. Lancaster,[21] G. Latino,[32] T. LeCompte,[2] A. M. Lee IV,[9] K. Lee,[39] S. Leone,[32] J. D. Lewis,[10] M. Lindgren,[5] T. M. Liss,[16] J. B. Liu,[35] Y. C. Liu,[1] N. Lockyer,[31] J. Loken,[29] M. Loreti,[30] D. Lucchesi,[30] P. Lukens,[10] S. Lusin,[44] L. Lyons,[29] J. Lys,[21] R. Madrak,[14] K. Maeshima,[10] P. Maksimovic,[14] L. Malferrari,[3] M. Mangano,[32] M. Mariotti,[30] G. Martignon,[30] A. Martin,[45] J. A. J. Matthews,[26] J. Mayer,[23] P. Mazzanti,[3] K. S. McFarland,[35] P. McIntyre,[38] E. McKigney,[31] M. Menguzzato,[30] A. Menzione,[32] C. Mesropian,[36] T. Miao,[10] R. Miller,[25] J. S. Miller,[24] H. Minato,[41]

S. Miscetti,[12] M. Mishina,[20] G. Mitselmakher,[11] N. Moggi,[3] E. Moore,[26] R. Moore,[24] Y. Morita,[20] M. Mulhearn,[22] A. Mukherjee,[10] T. Muller,[18] A. Munar,[32] P. Murat,[10] S. Murgia,[25] M. Musy,[40] J. Nachtman,[5] S. Nahn,[45] H. Nakada,[41] T. Nakaya,[7] I. Nakano,[15] C. Nelson,[10] D. Neuberger,[18] C. Newman-Holmes,[10] C.-Y. P. Ngan,[22] P. Nicolaidi,[40] H. Niu,[4] L. Nodulman,[2] A. Nomerotski,[11] S. H. Oh,[9] T. Ohmoto,[15] T. Ohsugi,[15] R. Oishi,[41] T. Okusawa,[28] J. Olsen,[44] W. Orejudos,[21] C. Pagliarone,[32] F. Palmonari,[32] R. Paoletti,[32] V. Papadimitriou,[39] S. P. Pappas,[45] D. Partos,[4] J. Patrick,[10] G. Pauletta,[40] M. Paulini,[21] C. Paus,[22] L. Pescara,[30] T. J. Phillips,[9] G. Piacentino,[32] K. T. Pitts,[16] R. Plunkett,[10] A. Pompos,[34] L. Pondrom,[44] G. Pope,[33] M. Popovic,[23] F. Prokoshin,[8] J. Proudfoot,[2] F. Ptohos,[12] O. Pukhov,[8] G. Punzi,[32] K. Ragan,[23] A. Rakitine,[22] D. Reher,[21] A. Reichold,[29] W. Riegler,[14] A. Ribon,[30] F. Rimondi,[3] L. Ristori,[32] W. J. Robertson,[9] A. Robinson,[23] T. Rodrigo,[6] S. Rolli,[42] L. Rosenson,[22] R. Roser,[10] R. Rossin,[30] A. Safonov,[36] W. K. Sakumoto,[35] D. Saltzberg,[5] A. Sansoni,[12] L. Santi,[40] H. Sato,[41] P. Savard,[23] P. Schlabach,[10] E. E. Schmidt,[10] M. P. Schmidt,[45] M. Schmitt,[14] L. Scodellaro,[30] A. Scott,[5] A. Scribano,[32] S. Segler,[10] S. Seidel,[26] Y. Seiya,[41] A. Semenov,[8] F. Semeria,[3] T. Shah,[22] M. D. Shapiro,[21] P. F. Shepard,[33] T. Shibayama,[41] M. Shimojima,[41] M. Shochet,[7] J. Siegrist,[21] G. Signorelli,[32] A. Sill,[39] P. Sinervo,[23] P. Singh,[16] A. J. Slaughter,[45] K. Sliwa,[42] C. Smith,[17] F. D. Snider,[10] A. Solodsky,[36] J. Spalding,[10] T. Speer,[13] P. Sphicas,[22] F. Spinella,[32] M. Spiropulu,[14] L. Spiegel,[10] J. Steele,[44] A. Stefanini,[32] J. Strologas,[16] F. Strumia, [13] D. Stuart,[10] K. Sumorok,[22] T. Suzuki,[41] T. Takano,[28] R. Takashima,[15] K. Takikawa,[41] P. Tamburello,[9] M. Tanaka,[41] B. Tannenbaum,[5] W. Taylor,[23] M. Tecchio,[24] P. K. Teng,[1] K. Terashi,[41] S. Tether,[22] D. Theriot,[10] R. Thurman-Keup,[2] P. Tipton,[35] S. Tkaczyk,[10] K. Tollefson,[35] A. Tollestrup,[10] H. Toyoda,[28] W. Trischuk,[23] J. F. de Troconiz,[14] J. Tseng,[22] N. Turini,[32] F. Ukegawa,[41] T. Vaiciulis,[35] J. Valls,[37] S. Vejcik III,[10] G. Velev,[10] R. Vidal,[10] R. Vilar,[6] I. Volobouev,[21] D. Vucinic,[22] R. G. Wagner,[2] R. L. Wagner,[10] J. Wahl,[7] N. B. Wallace,[37] A. M. Walsh,[37] C. Wang,[9] C. H. Wang,[1] M. J. Wang,[1] T. Watanabe,[41] D. Waters,[29] T. Watts,[37] R. Webb,[38] H. Wenzel,[18] W. C. Wester III,[10] A. B. Wicklund,[2] E. Wicklund,[10] H. H. Williams,[31] P. Wilson,[10] B. L. Winer,[27] D. Winn,[24] S. Wolbers,[10] D. Wolinski,[24] J. Wolinski,[25]

S. Wolinski,[24] S. Worm,[26] X. Wu,[13] J. Wyss,[32] A. Yagil,[10] W. Yao,[21] G. P. Yeh,[10] P. Yeh,[1] J. Yoh,[10] C. Yosef,[25] T. Yoshida,[28] I. Yu,[19] S. Yu,[31] Z. Yu,[45] A. Zanetti,[40] F. Zetti,[21] and S. Zucchelli[3]

(CDF Collaboration)

[1] *Institute of Physics, Academia Sinica, Taipei, Taiwan 11529, Republic of China*

[2] *Argonne National Laboratory, Argonne, Illinois 60439*

[3] *Istituto Nazionale di Fisica Nucleare, University of Bologna, I-40127 Bologna, Italy*

[4] *Brandeis University, Waltham, Massachusetts 02254*

[5] *University of California at Los Angeles, Los Angeles, California 90024*

[6] *Instituto de Fisica de Cantabria, CSIC-University of Cantabria, 39005 Santander, Spain*

[7] *Enrico Fermi Institute, University of Chicago, Chicago, Illinois 60637*

[8] *Joint Institute for Nuclear Research, RU-141980 Dubna, Russia*

[9] *Duke University, Durham, North Carolina 27708*

[10] *Fermi National Accelerator Laboratory, Batavia, Illinois 60510*

[11] *University of Florida, Gainesville, Florida 32611*

[12] *Laboratori Nazionali di Frascati, Istituto Nazionale di Fisica Nucleare, I-00044 Frascati, Italy*

[13] *University of Geneva, CH-1211 Geneva 4, Switzerland*

[14] *Harvard University, Cambridge, Massachusetts 02138*

[15] *Hiroshima University, Higashi-Hiroshima 724, Japan*

[16] *University of Illinois, Urbana, Illinois 61801*

[17] *The Johns Hopkins University, Baltimore, Maryland 21218*

[18] *Institut für Experimentelle Kernphysik, Universität Karlsruhe, 76128 Karlsruhe, Germany*

[19] *Korean Hadron Collider Laboratory: Kyungpook National University, Taegu 702-701; Seoul National University, Seoul 151-742; and SungKyunKwan University, Suwon 440-746; Korea*

[20] *High Energy Accelerator Research Organization (KEK), Tsukuba, Ibaraki 305, Japan*

[21] *Ernest Orlando Lawrence Berkeley National Laboratory, Berkeley, California 94720*

[22] *Massachusetts Institute of Technology, Cambridge, Massachusetts 02139*

[23] *Institute of Particle Physics: McGill University, Montreal H3A 2T8; and University of Toronto, Toronto M5S 1A7; Canada*

[24] *University of Michigan, Ann Arbor, Michigan 48109*

[25] *Michigan State University, East Lansing, Michigan 48824*

[26] *University of New Mexico, Albuquerque, New Mexico 87131*

[27] *The Ohio State University, Columbus, Ohio 43210*

[28] *Osaka City University, Osaka 588, Japan*

[29] *University of Oxford, Oxford OX1 3RH, United Kingdom*

[30] *Universita di Padova, Istituto Nazionale di Fisica Nucleare, Sezione di Padova, I-35131 Padova, Italy*

[31] *University of Pennsylvania, Philadelphia, Pennsylvania 19104*

[32] *Istituto Nazionale di Fisica Nucleare, University and Scuola Normale Superiore of Pisa, I-56100 Pisa, Italy*

[33] *University of Pittsburgh, Pittsburgh, Pennsylvania 15260*

[34] *Purdue University, West Lafayette, Indiana 47907*

[35] *University of Rochester, Rochester, New York 14627*

[36] *Rockefeller University, New York, New York 10021*

[37] *Rutgers University, Piscataway, New Jersey 08855*

[38] *Texas A&M University, College Station, Texas 77843*

[39] *Texas Tech University, Lubbock, Texas 79409*

[40] *Istituto Nazionale di Fisica Nucleare, University of Trieste/ Udine, Italy*

[41] *University of Tsukuba, Tsukuba, Ibaraki 305, Japan*

[42] *Tufts University, Medford, Massachusetts 02155*

[43] *Waseda University, Tokyo 169, Japan*

[44] *University of Wisconsin, Madison, Wisconsin 53706*

[45] *Yale University, New Haven, Connecticut 06520*

Bibliography

[1] J. Dalton, "A New System of Chemical Philosophy (Part I)", Manchester (1808).

[2] R.P. Feynman et al., "The Feynman Lectures on Physics (Vol. 1)", Addison-Wesley Publishing Company (1963) pp. 1-2.

[3] W.C. Röntgen, *Über eine neue Art von Strahlen. Vorlaufige Mitteilung*, Sitzber. Physik. Med. Ges. **137**, 1 (1895).

[4] H. Becquerel, *Emission de Radiations Nouvelles par l'Uranium Metallique*, Compt. Ren. **122**, 1086 (1896).

[5] J.J. Thompson, *Cathode Rays*, Phil. Mag. **44**, 293 (1897); idem, Nature **55**, 453 (1897).

[6] E. Rutherford, *The Structure of the Atom*, Nature **92**, 423 (1913).

[7] E. Rutherford, *Collision of α Particles with Light Atoms IV. An Anomalous Effect in Nitrogen*, Phil. Mag. **37**, 581 (1919).

[8] J. Chadwick, *The Existence of a Neutron*, Proc. Roy. Soc. **A136**, 692 (1932).

[9] A.H. Compton, *The Spectrum of Scattered X Rays*, Phys. Rev. **22**, 409 (1923).

[10] C.J. Davisson & L.H. Germer, *Diffraction of Electrons by a Crystal of Nickel*, Phys. Rev. **30**, 705 (1927); G.P. Thompson, *Experiments on Diffraction of Cathode Rays*, Proc. Roy. Soc. **A117**, 600 (1928).

[11] C.D. Anderson, *The Apparent Existence of Easily Deflectable Positives*, Science **76**, 238 (1932).

[12] D.H. Perkins, *Nuclear Disintegration by Meson Capture*, Nature **159**, 126 (1947).

[13] H. Yukawa, *On the Interation of Elementary Particles*, Proc. Phys. Math. Soc. Jap. **17**, 48 (1935).

[14] W. Heisenberg, *Über den Bau der Atomkerne. I*, Z. Phys. **77**, 1 (1932).

[15] M. Gell-Mann, *The Eightfold Way: A Theory of Strong Interaction Symmetry*, CTSL-20 (1961); idem, *Symmetries of Baryons and Mesons*, Phys. Rev. **125**, 1067 (1962).

[16] Y. Ne'eman, *Derivation of Strong Interactions from a Gauge Invariance*, Nucl. Phys. **26**, 222 (1961).

[17] M. Gell-Mann, *A Schematic Model of Baryons and Mesons*, Phys. Lett. **8**, 214 (1964).

[18] G. Zweig, *An $SU(3)$ Model for Strong Interaction Symmetry and its Breaking I*, CERN-8182-TH-401 (1964); idem, *An $SU(3)$ Model for Strong Interaction Symmetry and its Breaking II*, CERN-8419-TH-412 (1964);

[19] E.D. Bloom et al., *High-Energy $e^- p$ Scattering at 6° and 10°*, Phys. Rev. Lett. **23**, 930 (1969); M. Breidenbach et al., *Observed Behaviour of Highly Inelastic Electron-Proton Scattering*, Phys. Rev. Lett. **23**, 935 (1969); G. Miller et al., *Inelastic e^- p Scattering at Large Momentum Transfers and the Inelastic Structure Function of the Proton*, Phys. Rev. **D 5**, 528 (1972).

[20] J.D. Bjorken, *Asymptotic Sum Rules at Infinite Momentum*, Phys. Rev. **179**, 1547 (1969).

[21] R.P. Feynman, *Very High-Energy Collisions of Hadrons*, Phys. Rev. Lett. **23**, 1415 (1969).

[22] O.W. Greenberg & D. Zwanziger, *Saturation in Triplet Models of Hadrons*, Phys. Rev. **150**, 1177 (1966).

[23] D.J. Gross & F. Wilczek, *Asymptotically Free Gauge Theories*, Phys. Rev. **D 8**, 3633 (1973).

[24] J.J. Aubert et al., *Experimental Observation of a Heavy Particle J*, Phys. Rev. Lett. **33**, 1404 (1974).

[25] J.E. Augustin et al., *Discovery of a Narrow Resonance in e^+ e^- Annihilation*, Phys. Rev. Lett. **33**, 1406 (1974).

[26] S.W. Herb et al., *Observation of a Dimuon Resonance at 9.5 GeV in 400 GeV Proton-Nucleus Collisions*, Phys. Rev. Lett. **39**, 252 (1977).

[27] D.P. Barber et al., The MARK-J Collaboration, *Discovery of Three Jet Events and a Test of Quantum Chromodynamics at PETRA Energies*, Phys. Rev. Lett. **43**, 830 (1979); R. Brandelik et al., The TASSO Collaboration, *Evidence for Planar Events in e^+ e^- Annihilation at High Energies*, Phys. Lett. **86B**, 243 (1979); C. Berger et al., The PLUTO Collaboration, *Evidence for Gluon Bremsstrahlung in e^+ e^- Annihilation at High Energies*, Phys. Lett. **86B**, 418 (1979).

[28] F. Abe et al., The CDF Collaboration, *Observation of Top Quark Production in $\bar{p}p$ Collisions*, Phys. Rev. Lett. **74**, 2626 (1995); S. Abachi et al., The D0 Collaboration, *Observation of the Top Quark*, Phys. Rev. Lett. **74**, 2632 (1995).

[29] K. Hagiwara & K. Hikasa, *Searches for Quark and Lepton Compositeness*, in "Review of Particle Physics" (C. Caso et al., Particle Data Group), Eur. Phys. J. **C 3**, 772 (1998).

[30] R. Landua, *Non-$q\bar{q}$ Candidates*, in "Review of Particle Physics" (C. Caso et al., Particle Data Group), Eur. Phys. J. **C 3**, 609 (1998).

[31] For some examples, see C. Quigg, "Gauge Theories of the Strong, Weak and Electromagnetic Interactions", Addison-Wesley (1984), pp. 11-15.

[32] C. Quigg, *Realizing the Potential of Quarkonium*, FERMILAB-CONF-97-266-T (1997).

[33] B. Nemati et al., The CLEO Collaboration, *Measurement of the Direct Photon Spectrum in* $\Upsilon(1S)$ *Decays*, Phys. Rev. **D 55**, 5273 (1997).

[34] I. Hinchliffe, *Quantum Chromodynamics*, in "Review of Particle Physics" (C. Caso et al., Particle Data Group), Eur. Phys. J. **C 3**, 81 (1998).

[35] For a detailed discussion of heavy quark production, see for example, R.K. Ellis, W.J. Stirling & B.R. Webber, "QCD and Collider Physics", Cambridge University Press (1996), pp. 347-384.

[36] J.F. Amundson et al., *Quantitative Tests of Color Evaporation: Charmonium Production*, Phys. Lett. **B390**, 323 (1997).

[37] E. Braaten, S. Fleming & T.C. Yuan, *Production of Heavy Quarkonium in High Energy Colliders*, Ann. Rev. Nucl. Part. Sci. **46**, 197 (1996).

[38] E. Braaten & T.C. Yuan, *Gluon Fragmentation into Heavy Quarkonium*, Phys. Rev. Lett. **71**, 1673 (1993).

[39] G.T. Bodwin, E. Braaten & G.P. Lepage, *Rigorous QCD Analysis of Inclusive Annihilation and Production of Heavy Quarkonium*, Phys. Rev. **D** 51, 1125 (1995), Erratum ibid. **D55**, 5853 (1997).

[40] W.E. Caswell & G.P. Lepage, *Effective Lagrangians for Bound State Problems in QED, QCD, and Other Field Theories*, Phys. Lett. **B167**, 437 (1986).

[41] A. Manohar, *Effective Field Theories*, in "Schladming 1996, Perturbative and nonperturbative aspects of quantum field theory" (1996).

[42] P. Cho & A. Leibovich, *Color-Octet Quarkonium Production*, Phys. Rev. **D 53**, 150 (1996); idem, *Color-Octet Quarkonium Production. II*, Phys. Rev. **D 53**, 6203 (1996).

[43] M. Beneke & M. Krämer, *Direct J/ψ and ψ' Polarization and Cross Sections at the Tevatron*, Phys. Rev. **D 55**, 5269 (1997).

[44] M.A. Sanchis-Lozano & B. Cano-Coloma, *Charmonia production in hadron colliders and the extraction of colour-octet matrix elements*, Nucl. Phys. **B508**, 753 (1997).

[45] B.A. Kniehl & G. Kramer, *Inclusive J/ψ and $\psi(2S)$ Production from B Decay in $p\bar{p}$ Collisions*, Phys. Rev. **D 60**, 014006 (1999).

[46] B.A. Kniehl & G. Kramer, *Tevatron-HERA Colour Octet Charmonium Anomaly Versus Higher-Order QCD Effects*, Eur. Phys. J. **C 6**, 493 (1999).

[47] M. Beneke, I.Z. Rothstein & M.B. Wise, *Kinematic Enhancements of Non-Perturbative Corrections to Quarkonium Production*, Phys. Lett. **B408**, 373 (1997).

[48] C-Y. Wong, *The Soft Gluon Emission Process in the Color-Octet Model for Heavy Quarkonium Production*, Phys. Rev. **D 60**, 114025 (1999).

[49] F. Abe et al., The CDF Collaboration, *Υ Production in $p\bar{p}$ Collisions at $\sqrt{s} = 1.8$ TeV*, Phys. Rev. Lett **75**, 4358 (1995).

[50] F. Abe et al., The CDF Collaboration, *J/ψ and $\psi(2S)$ Production in $p\bar{p}$ Collisions at $\sqrt{s} = 1.8$ TeV*, Phys. Rev. Lett **79**, 572 (1997).

[51] F. Abe et al., The CDF Collaboration, *Production of J/ψ from χ_c Decays in $p\bar{p}$ Collisions at $\sqrt{s} = 1.8$ TeV*, Phys. Rev. Lett **79**, 578 (1997).

[52] E. Braaten & S. Fleming, *Color-Octet Fragmentation and the ψ' Surplus at the Tevatron*, Phys. Rev. Lett. **74**, 3327 (1995).

[53] P. Cho & M.B. Wise, *Spin Symmetry Predictions for Heavy Quarkonia Alignment*, Phys. Lett. **B346**, 129 (1995).

[54] E. Braaten & Y-Q. Chen, *Helicity Decomposition for Inclusive J/ψ Production*, Phys. Rev. **D 54**, 3216 (1996).

[55] M. Beneke & I.Z. Rothstein, *ψ' Polarization as a Test of Color Octet Quarkonium Production*, Phys. Lett. **B372**, 157 (1996), Erratum ibid. **B389**, (1996).

[56] A. Leibovich, *ψ' Polarization due to Color-Octet Quarkonia Production*, Phys. Rev. **D 56**, 4412 (1997).

[57] E. Braaten, B. Kniehl and J. Lee, *Polarization of Prompt J/ψ at the Tevatron*, hep-ph/9911436 (1999).

[58] A. Tkabladze, *Bottomonium Polarization in Hadroproduction*, Phys. Lett. **B462**, 319 (1999).

[59] T. Affolder et al., The CDF Collaboration, *Measurement of J/ψ and $\psi(2S)$ Polarization in $p\bar{p}$ Collisions at $\sqrt{s} = 1.8$ TeV*, hep-ex/0004027, to be published in Phys. Rev. Lett. (2000).

[60] E.M. McMillan, *The Synchrotron — A Proposed High Energy Particle Accelerator*, Phys. Rev. **68**, 143 (1945); idem, *Resonance Acceleration of Charged Particles*, Phys. Rev. **70**, 800 (1946).

[61] C. Rubbia, P. McIntyre & D. Cline, *Producing Massive Neutral Intermediate Vector Bosons with Existing Accelerators*, Proc. Intern. Neutrino Conf. Aachen 1976 (ed. Vieweg, Braunschweig), 683 (1977); The staff of the CERN proton-antiproton project, *First Proton-Antiproton Collisions in the CERN SPS Collider*, Phys. Lett. **B107**, 306 (1981).

[62] Fermi National Accelerator Laboratory, *Design Report for the Tevatron I Project*, 1984.

[63] D. Cronin-Hennessy, A. Beretvas & P. Derwent, *Luminosity at CDF*, CDF internal note CDF4956, to be submitted to Nucl. Instrum. Methods (1999).

[64] J.R. Sanford, *The Fermi National Accelerator Laboratory*, Ann. Rev. Nucl. Sci. **26**, 151 (1976).

[65] J.D. Cockcroft & E.T.S. Walton, *Artificial Production of Fast Protons*, Nature **129**, 242 (1932); idem, *Disintegration of Lithium by Swift Protons*, Nature **129**, 649 (1932).

[66] E.D. Courant, M.S. Livingston, & H.S. Snyder, *The Strong-Focusing Synchrotron — A New High Energy Accelerator*, Phys. Rev. **88**, 1190 (1952).

[67] M.D. Church & J.P. Marriner, *The Antiproton Sources: Design and Operation*, Ann. Rev. Nucl. Part. Sci. **43**, 253 (1993).

[68] A. Ruggiero, *The Fermilab Tevatron I Debuncher Ring*, IEEE Trans. Nucl. Sci. **30**, 2478 (1983).

[69] D. Möhl, G. Petrucci, L. Thorndahl & S. van der Meer, *Physics and Techniques of Stochastic Cooling*, Phys. Rep. **58**, 73 (1980).

[70] A. Ando, T. Collins & D. Johnson, *Design of an 8-GeV Accumulator Ring for the Fermilab Tevatron I Project*, IEEE Trans. Nucl. Sci. **30**, 2031 (1983).

[71] *High-Energy Collider Parameters*, in "Review of Particle Physics" (R.M. Barnett et al., Particle Data Group), Phys. Rev. **D 54**, 128 (1996).

[72] H. Edwards, *The Tevatron Energy Doubler: A Superconducting Accelerator*, Ann. Rev. Nucl. Part. Sci. **35**, 605 (1985).

[73] R. Palmer & A.V. Tollestrup, *Superconducting Magnet Technology for Accelerators*, Ann. Rev. Nucl. Part. Sci. **34**, 247 (1984).

[74] H. Williams, *Design Principles of Detectors at Colliding Beams*, Ann. Rev. Nucl. Part. Sci. **36**, 361 (1986).

[75] F. Abe et al., The CDF Collaboration, *The CDF Detector: An Overview*, Nucl. Instrum. Methods Phys. Res. A **271**, 387 (1988).

[76] F. Abe et al., The CDF Collaboration, *Evidence for Top Quark Production in $p\bar{p}$ Collisions at $\sqrt{s}$ = 1.8 TeV*, Phys. Rev. **D 50**, 2996 (1994).

[77] H. Minemura et al., *Construction and Testing of a 3m Diameter × 5m Superconducting Solenoid for the Fermilab Collider Detector Facility (CDF)*, Nucl. Instrum. Methods Phys. Res. A **238**, 18 (1985).

[78] F. Bedeschi et al., *Design and Construction of the CDF Central Tracking Chamber*, Nucl. Instrum. Methods Phys. Res. A **268**, 50 (1988).

[79] F. Sauli, *Principles of Operation of Multiwire Proportional and Drift Chambers*, CERN Report 77-09 (1977).

[80] F. Abe et al., The CDF Collaboration, *Measurement of the W Boson Mass*, Phys. Rev. **D 52**, 4784 (1995).

[81] Andreas Warburton, Ph.D. Dissertation, University of Toronto, 1998.

[82] G. Lutz & A.S. Schwartz, *Silicon Detectors for Charged-Particle Track and Vertex Detectors*, Ann. Rev. Nucl. Part. Sci. **45**, 295 (1995).

[83] S. Tkaczyk et al., *The CDF Silicon Vertex Detector*, Nucl. Instrum. Methods Phys. Res. A **342**, 240 (1994).

[84] D. Amidei et al., *The Silicon Vertex Detector of the Collider Detector at Fermilab*, Nucl. Instrum. Methods Phys. Res. A **350**, 73 (1994).

[85] P. Azzi et al., *SVX′, The New CDF Silicon Vertex Detector*, Nucl. Instrum. Methods Phys. Res. A **360**, 137 (1995).

[86] S. Tkaczyk, *Operational Experience with CDF Silicon Microvertex Detectors*, Nucl. Instrum. Methods Phys. Res. A **368**, 240 (1995).

[87] P.P. Allport et al., *FOXFET biassed microstrip detectors*, Nucl. Instrum. Methods Phys. Res. A **310**, 155 (1991).

[88] S. Kleinfelder et al., *A Flexible 128 Channel Silicon Strip Detector Instrumentation Integrated Circuit with Sparse Data Readout*, IEEE Trans. Nucl. Sci. **35**, 171 (1988); C. Haber et al., *Design and Prototyping of the Front End Readout System for the CDF Silicon Vertex Detector*, IEEE Trans. Nucl. Sci. **37**, 1120 (1990).

[89] J.N. Marx & D.R. Nygren, *The Time Projection Chamber*, Physics Today **31** No. 10, 46 (1978).

[90] F. Snider et al., *The CDF Vertex Time Projection Chamber System*, Nucl. Instrum. Methods Phys. Res. A **268**, 75 (1988).

[91] C. Fabjan, *Calorimetry in High-Energy Physics*, in "Experimental Techniques in High Energy Physics" (ed. T. Ferbel), Addison-Wesley (1987).

[92] L. Balka et al., *The CDF Central Electromagnetic Calorimeter*, Nucl. Instrum. Methods Phys. Res. A **267**, 272 (1988).

[93] S. Bertolucci et al., *The CDF Central and Endwall Hadron Calorimeter*, Nucl. Instrum. Methods Phys. Res. A **267**, 301 (1988).

[94] Y. Fukui et al., *CDF End Plug Electromagnetic Calorimeter Using Conductive Plastic Proportional Tubes*, Nucl. Instrum. Methods Phys. Res. A **267**, 280 (1988).

[95] G. Brandenburg et al., *An Electromagnetic Calorimeter for the Small Angle Regions of the Collider Detector at Fermilab*, Nucl. Instrum. Methods Phys. Res. A **267**, 257 (1988).

[96] S. Cihangir et al., *The CDF Forward/Backward Hadron Calorimeter*, Nucl. Instrum. Methods Phys. Res. A **267**, 249 (1988).

[97] K. Byrum et al., *The CDF Forward Muon System*, Nucl. Instrum. Methods Phys. Res. A **268**, 46 (1988).

[98] G. Ascoli et al., *CDF Central Muon Detector*, Nucl. Instrum. Methods Phys. Res. A **268**, 33 (1988).

[99] J.D. Lewis et al., The 1992 CDF Muon System Upgrade, CDF public note CDF/PUB/MUON/PUBLIC/2858 (1994).

[100] G. Ascoli et al., *CDF Central Muon Level-1 Trigger Electronics*, Nucl. Instrum. Methods Phys. Res. A **269**, 63 (1988).

[101] F. Abe et al., The CDF Collaboration, *Measurement of* $\sigma\mathcal{B}(W \to e\nu)$ *and* $\sigma\mathcal{B}(Z \to ee)$ *in* $p\bar{p}$ *Collisions at* $\sqrt{s}$ *= 1.8 TeV*, Phys. Rev. Lett. **76**, 3070 (1996).

[102] E. Barsotti et al., *FASTBUS Data Acquisition for CDF*, Nucl. Instrum. Methods Phys. Res. A **269**, 82 (1988).

[103] G. Drake et al., *CDF Front End Electronics: The RABBIT System*, Nucl. Instrum. Methods Phys. Res. A **269**, 68 (1988).

[104] D. Amidei et al., *A Two Level FASTBUS Based Trigger System for CDF*, Nucl. Instrum. Methods Phys. Res. A **269**, 51 (1988).

[105] J. Carroll et al., *The CDF Level 3 Trigger*, Nucl. Instrum. Methods Phys. Res. A **300**, 552 (1991).

[106] S.P. Pappas, J.D. Lewis & G. Michail, *Run 1B Low* p_T *Central Dimuon Trigger Efficiencies*, CDF internal note CDF/ANAL/TRIGGER/CDFR/4076, unpublished (1997).

[107] P. Schlabach, *Introduction to the CDF Muon Trigger and its Monitoring by TRIGMON*, CDF public note CDF/MEMO/MUON/PUBLIC/2834 (1994).

[108] G.W. Foster et al., *A Fast Hardware Track-Finder for the CDF Central Tracking Chamber*, Nucl. Instrum. Methods Phys. Res. A **269**, 93 (1988).

[109] J.D. Lewis & K.T. Pitts, *A summary of CFT Operation in Run 1*, CDF internal note CDF/DOC/TRIGGER/CDFR/3999, unpublished (1997).

[110] D. Quarrie & B. Troemel, *YBOS Programmer's Reference Manual*, CDF public note CDF/DOC/CDF/PUBLIC/0156 (1987).

[111] J. Bunn & M. Goossens, *HBOOK - Statistical Analysis and Histogramming - Reference Manual*, CERN Program Library Entry Y250 (1995).

[112] R. Cropp & W. Trischuk, *Potential Improvements to the J/ψ Polarization Measurement*, CDF internal note CDF/ANAL/BOTTOM/CDFR/5166, unpublished (1999).

[113] H. Wenzel et al., *Beamlines*, CDF internal note CDF/ANAL/SEC_VTX/CDFR/3334, unpublished (1995).

[114] J. Marriner, *Secondary Vertex Fit with (optional) Mass Constraints and (optional) Pointing Constraints*, CDF public note CDF/DOC/SEC_VTX/PUBLIC/1996 (1993).

[115] F. Abe et al., The CDF Collaboration, *Measurement of B Hadron Lifetimes Using J/ψ Final States at CDF*, Phys. Rev. **D 57**, 5382 (1998).

[116] C. Caso et al., Particle Data Group, "Review of Particle Physics", Eur. Phys. J. **C 3**, 1 (1998).

[117] J.D. Jackson, *Particle and Polarization Angular Distributions*, in "High Energy Physics (Les Houches 1965)" (ed. C. DeWitt & M. Jacob), Gordon & Breach Science Publishers (1965).

[118] F. James, *MINUIT - Function Minimization and Error Analysis*, CERN Program Library Entry D506 (1998).

[119] T. Daniels et al., *J/ψ and ψ' Cross Sections*, CDF internal note 3561, unpublished (1996).

[120] M. Shapiro et al., *A User's Guide to QFL*, CDF public note CDF/ANAL/MONTECARLO/PUBLIC/1810 (1992).

[121] F. DeJongh & R. Hans, *Level 1 and Level 2 Low P_t Central Muon Trigger Efiiciencies for Run 1A*, CDF internal note 1999, unpublished (1993).

[122] S. Pappas, *DIMUTG: Dimuon Trigger Simulation for Run 1B*, CDF internal note CDF/ANAL/TRIGGER/CDFR/3537, unpublished (1996).

[123] T. Devlin, *Correlations from Systematic Corrections to Poisson-Distributed Data in Log-Likelihood Functions*, CDF public note CDF/DOC/JET/PUBLIC/3126 (1995).

[124] P. Hoyer & S. Peigne, *Quarkonium Production through Hard Comover Scattering*, Phys. Rev. **D 59**, 034011 (1999); N. Marchal, S. Peigne & P. Hoyer, *Quarkonium Production through Hard Comover Scattering. II*, hep-ph/0004234 (2000).

[125] Ph. Hägler et al., *Towards a solution of the charmonium production controversy: k_t-factorization versus color octet mechanism*, hep-ph/0004263 (2000).

[126] S. Fleming et al., *NRQCD matrix elements in polarization of J/ψ produced from b-decay*, Phys. Rev. **D 55**, 4098 (1997).

[127] T. Affolder et al., The CDF Collaboration, *Measurement of the Decay Amplitudes of the Decays $B^0 \to J/\psi\ K^*$ and $B_s^0 \to J/\psi\ \phi$ at CDF*, to be submitted to Phys. Rev. Lett. (2000).

[128] C.P. Jessop et al., The CLEO Collaboration, *Measurement of the Decay Amplitudes and Branching Fractions of $B \to J/\psi\ K^*$ and $B \to J/\psi\ K$ Decays*, Phys. Rev. Lett. **79**, 4533 (1997).

[129] F. Abe et al., The CDF II Collaboration, *The CDF II Detector Technical Design Report*, FERMILAB-Pub-96/390-E (1996).

[130] T. Affolder et al., The CDF Collaboration, *Measurement of J/ψ and $\psi(2S)$ Polarization in $p\bar{p}$ Collisions at $\sqrt{s} = 1.8$ TeV*, submitted to Phys. Rev. Lett. (2000).

[131] R. Cropp, for the CDF Collaboration, *Recent results on J/ψ, $\psi(2S)$ and Υ production at CDF*, to be published in "Proceedings of the International Europhysics Conference on High-Energy Physics, Tampere, Finland, 15-21 July 1999".

[132] M. Beneke, *Quarkonium Polarization as a Test of Non-Relativistic Effective Theory*, in "Jerusalem 1997, High energy physics", 549 (1997).

[133] K. Sridhar, A.D. Martin & W.J. Stirling, *ψ production at the Tevatron and HERA: the effect of k_T smearing*, Phys. Lett. **B438**, 211 (1998).

[134] P. Azzi-Bacchetta et al., *Proposal for a Very Low Mass, Very Small Radius Silicon Layer In the CDF II Upgrade*, CDF public note CDF/DOC/SEC_VTX/PUBLIC/4924 (1999).

[135] F. Hartmann, *The CDF Intermediate Silicon Layers Detector at VERTEX98*, CDF public note CDF/PUB/SEC_VTX/PUBLIC/4796 (1998).

[136] M. Bishai et al., *An SVX3D Chip User's Companion*, CDF internal note CDF/DOC/TRACKING/GROUP/5062, unpublished (1999).

[137] A. Affolder et al., *Production Testing of ISL Modules at FNAL*, CDF public note CDF/DOC/TRACKING/PUBLIC/5180 (1999).

[138] F. Hartmann et al., *Evaluation of the ISL prototype detectors*, CDF internal note CDF/DOC/SEC_VTX/CDFR/4627, unpublished (1998).

[139] M. Rehn et al., *Bench Tests of SVXII Quarter-Ladder Q005*, CDF public note CDF/DOC/SEC_VTX/PUBLIC/5049 (1999).

[140] J. Valls et al., *Operation of a Burn-in Setup for SVXII/ISL Ladders*, CDF public note CDF/DOC/CDF/PUBLIC/4586 (1999).

[141] J. Valls et al., *Design and Operation of the SVX-II/ISL Burn-in Sytem*, CDF public note CDF/DOC/CDF/PUBLIC/5164 (1999).